A combination of QM and MM techniques to quantify the solvent effects on applications of catalysis and ligand separation under aqueous conditions

Dissertation

Presented in Partial Fulfillment of the Requirements for the Degree Doctor of Philosophy in the Graduate School of The Ohio State University

By

Ricardo Antonio Garcia Carcamo, M.Sc.

Graduate Program in
Chemical Engineering

The Ohio State University

2024

Dissertation Committee:

Dr. Rachel B. Getman, Advisor

Dr. Aravind Asthagiri

Dr. Lisa Hall

Abstract

Solvent effects have a great relevance in various areas of chemistry. In particular, solvents are used in catalysis and separations, with many applications ranging from biomass and syn-gas conversion, hydroformylation, electrocatalysis, and waste-water treatments, among others. Water effects can impact different aspects of the chemical process: adsorption/desorption, reaction thermodynamics, kinetics, selectivity, co-catalyzing reactions, and the generation of new active centers. For these reasons, quantification of solvent effects is crucial to understand and improve chemical processes that involve solvents. This understanding of the water effects requires capturing the solvation thermodynamics; this quantity captures the effect of the solvent/medium into a solvated molecule. To measure these effects, both experimental and computational techniques are used to unveil the behavior of the solvent under these different environments. On the one hand, experimentally overall effects can be estimated, but the solvent contribution is measured indirectly, and its effects are captured by apparent or lumped kinetics. However, computational techniques can isolate both specific contributions and overall effects that are necessary for a more complete understanding of the solvent-mediated process. In this dissertation, these computational techniques are applied to understand two applications, one on catalysis in liquid media and an ion-ligand binding process under aqueous conditions.

The first application in the area of catalysis in liquid media involves investigating solvent effects to elucidate reaction mechanisms under aqueous conditions for biomass conversion.

In this work, methanol dehydrogenation at platinum supported on alumina, a typical catalytic system for this application was explored. To obtain the reaction mechanism a dual-site model is proposed, one to model larger particles where the chemistry is dominated by the platinum metal interface and the other for smaller particles where the chemistry is influenced also by the presence of the support. The elucidation of the mechanism requires first the estimation of the solvent effect for these two sites and then the incorporation of the solvation thermodynamics into the mechanism. To estimate the solvation thermodynamics for these two sites, a multiscale sampling technique was used, combining density functional theory (DFT) and free energy perturbation (FEP) method from Molecular Dynamics (MD). The thermodynamic estimations showed that the modeled site for smaller particle sizes was less effectively solvated compared to that of the larger particles. Our research unveils the different behavior of water in the interfaces, where the hydrophilic alumina exhibits a larger entropic penalty for solvation. After the estimation of the solvation thermodynamics of both types of sites, these quantities enable us to elucidate the reaction mechanism under aqueous conditions via a microkinetic modeling. The microkinetic model reveals a different reaction mechanism at the two sites, with a higher reaction yield at the larger particle site model. The microkinetic model shows that water co-catalyzes the reaction mechanism at the larger particle size model, and in the case of the smaller particle size model, water hinders the reaction via a water-splitting path. This study shows that solvent effects can impact the catalytic performance, sometimes enhancing it, others hindering it; and exhibiting a different behavior depending on the nature of the interface.

For the second application, a strategy to estimate the thermodynamics of the ion-capturing process of rare earth metals under aqueous conditions is proposed. For this strategy, a series of Free Energy Perturbation calculations from molecular dynamics is performed

for the estimation of the process thermodynamics. The thermodynamics of the process indicate that all of the early lanthanides have favorable binding processes that are entropically driven. Additionally, it was found that the ligand presents a higher affinity for ions with a smaller ionic radius. This process is attributed for the most part to the release of some of the first solvation shell water from the ions in solution to the bulk water solution and the structural reorganization of the ligand around the ion.

Acknowledgments

I would like to acknowledge the many people for their support along my 4.5-year academic journey. Specifically, I would like to thank my advisor Dr. Rachel B. Getman, for her direction, support, and patience over these years.

Dr. Aravind Asthagiri and Dr. Lisa Hall for accepting to be on my committee and for providing guidance through the processes.

Angela Bennett, Terri McAllister, Joy Rodatz, and Diana Stamey for their support with all of the administrative efforts that are related to graduate students.

I would like to thank all of the past and current members of the Getman Group. Dr. Paul Meza-Morales, Dr. Ali Estejab, Dr. Tianjun Xie, Dr. Xiaohong Zhang, Dr. Hafeera Shabbir, Dr. Stephen Vicchio, Dr. Gulam Rabbani, Dr. Sanchari Bhattacharjee, Dr. Manish Maurya, and (future PhDs) Jiexin Shi, Xiuting Chen, Rohit Punyapu, Sayani Biswas, Tian Ning Chen, Sifat Hossain and Osasumwen Ikponmwosa for their valuable discussions and suggestions.

Vita

Publications

Research Publications

1. **Ricardo A. García C.**, T. Xie, B. J. Hare, C. Sievers and R. B. Getman, *Active Sites and Mechanism of Aqueous Phase Methanol Dehydrogenation on Pt/Al₂O₃ Catalysts.* Journal of Catalysis, 435:115562. April, 2024.

2. **Ricardo A. García C.**, X. Zhang, A. Estejab, J. Zhou, B. J. Hare, C. Sievers, S. Sarupria, and R. B. Getman, *Differences in Solvation Thermodynamics of Oxygenates at Pt/Al₂O₃ Perimeter Versus Pt(111) Terrace Sites*, iScience, 26, 105980. January, 2023.

3. Bryan J. Hare, **Ricardo A. García C.**, Luke L. Daemen, Yongqiang Cheng, Rachel B. Getman, and Carsten Sievers.*Poisoning of* Pt/γ-Al_2O_3 *Aqueous Phase Reforming Catalysts by Ketone and Diketone-Derived Surface Species.* ACS Catal. 14, 3, 1480–1493. January, 2024.

4. A. Estejab, **Ricardo A. García C.**, and R. B. Getman, *Influence of an Electrified Interface on the Entropy and Energy of Solvation of Methanol Oxidation Intermediates on Platinum(111) under Explicit Solvation*, Phys. Chem. Chem. Phys., 24, 4251-4261. January, 2022.

5. B. Hare, **<u>Ricardo A. García C.</u>**, R. B. Getman, and C. Sievers, *Surface Chemistry of Ketones and Diketones on Lewis Acidic γ-Al$_2$O$_3$ Probed by Infrared Spectroscopy*, J. Phys. Chem. C, 126, 17554-17568. October, 2022.

6. B. J. Hare, **<u>Ricardo A. García C.</u>**, T. Xie, P. J. Meza-Morales, R. B. Getman, and C. Sievers, *Active Sites and Effects of Co-Adsorbed H$_2$O on Isolated Methanol Dehydrogenation over* Pt/γ-Al$_2$O$_3$, Journal of Catalysis, 402, 218-228, 725010. October, 2021.

7. G. Verma, J. Hostert, A. Summerville, A. Robang, **<u>Ricardo A. García C.</u>**, A. Paravastu, R. B. Getman, C. Duval and J. Renner. *Investigation of Rare Earth Element Binding to a Surface-Bound Affinity Peptide Derived from EF Hand Loop I of Lanmodulin.* ACS Appl. Mater. Interfaces, 16, 13, 16912–16926. March, 2024

Fields of Study

Major Field: Chemical Engineering

Table of Contents

List of Tables

List of Figures

Chapter 1: Introduction and background

1.1 Motivation

Water is a widely used solvent for catalysis and biochemistry, with many applications ranging from biomass and syn-gas conversion, electro-catalysis, protein-folding, and waste-water treatments, among others[92;201;123]. Water effects can impact different aspects of chemical process like: adsorption/desorption, diffusion, reaction thermodynamics, kinetics, selectivity, co-catalyzing reactions, and the generation of new active centers[220;222;7;123;118]. All these factors are dependent on the different types of water environments, for instance: metal interfaces, hydrophilic and hydrophobic surfaces, electrodes, porous materials, protein-water interfaces, water-air interfaces, etc[17;173]. For these reasons, understanding the role of water is crucial for the improvement of catalysis in water and biochemistry under aqueous conditions, among other possible applications.

1.2 Quantification of solvent effects

Solvation can be defined, following Ben-Naim[11;13], as the process of transferring one solute molecule from a fixed position in an ideal gas phase to a fixed position in the liquid phase at constant pressure and temperature. And the term *hydration* energy refers to the specific case of aqueous solutions[169]. Another relevant distinction made by Ben-Naim[12] was between two solvation concepts: solvation (simply) and *conditional solvation*. Simply solvation refers to

the solvent's initial distribution in the absence of the solute (the solvent in the bulk solution), while textitconditional solvation specifically considers the initial solvent configuration in the absence of the solute, given the presence of a specific "condition" (this condition could be a ligand or an interface). This "condition" is often associated with a protein in the literature. A graphical representation of these two solvation concepts in shown in Figure 1.1. The first of these concepts in this dissertation is the equivalent of the solute solvation in the bulk aqueous phase, and the second concept is equivalent to the solvation of the different adsorbates bound to the catalyst surface or the ion bound to the ligand.
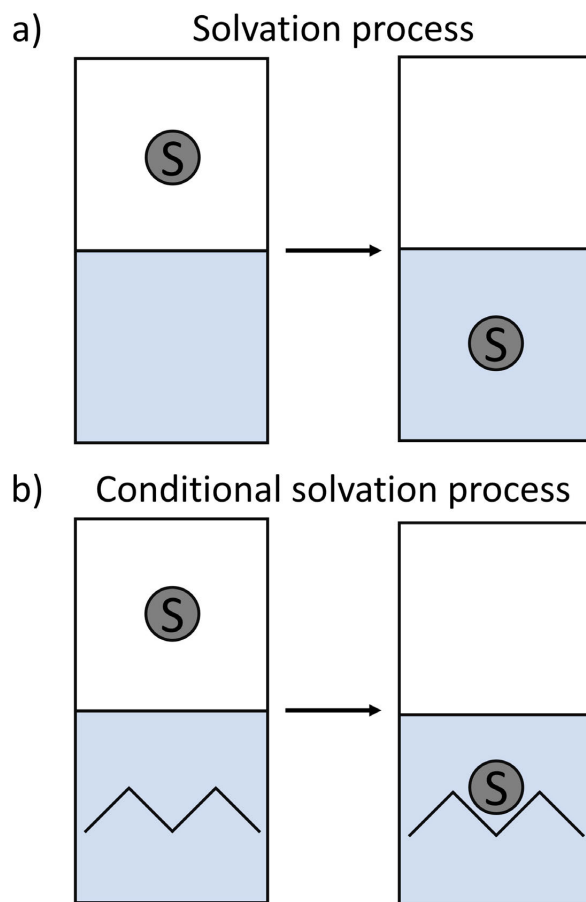
Figure 1.1: Graphical representation of the process of (a) solvation and (b) conditional solvation of a solute (s) in a liquid next to a protein. Adapted from Ref[13].

The solvation thermodynamics can subsequently influence other relevant physico-chemical properties such as adsorption or desorption rates, reaction free energies, activation barriers, dissociation constant, among others. To measure these effects, both experimental and computational techniques are used to describe the physico-chemical behavior of the water under these different environments. These different techniques have different strengths and disadvantages. Experimental methods to measure solvation thermodynamics mostly rely on calorimetric measurements and the estimation of Henry's law constants. These measurements exhibit relatively low uncertainties, typically around 1.5% and 4.2%, respectively[175;135]. However, most of the time they lack the capacity to isolate the specific thermodynamic contributions. Further, to isolate specific contributions an ideal reference is needed[163]. This isolation of the solvation thermodynamics is challenging because its effects are captured by apparent or lumped kinetics or mixed with adsorption energetics. In the case of computational techniques, all the specific contributions can be isolated with effort, but can exhibit considerable errors, depending on the simulated system. For example, continuum solvation models can display solvation free energy errors of approximately 0.2 eV[133] when compared to higher accuracy computational methods. Additionally, quantum mechanics/molecular mechanics approaches for single molecules exhibit hydration energies with relative differences ranging from 2% to 200%, depending on the solute[110]. These computational techniques have to balance computational cost, accuracy in energetics, and configurational sampling. For these reasons, a combination of both types of techniques can provide valuable insights into the role of the solvent in the solvent-mediated process.

1.2.1 Experimental quantification techniques

Solvation can be manifested in different effects depending on the process, and the measurement of this effect will vary accordingly. Two common experimental quantification procedures of solvent effects are in the areas of adsorption and reaction kinetics. In the case of the adsorption process, the solvation-free energy can be recovered by measuring the partition coefficient between the gas phase and the aqueous phase at the limit of infinite dilution as follows[169]:

$$K_H = \frac{C_i^g}{C_i^{aq}} \tag{1.1}$$

Where K_H is the Henry's law constant, C_i^g and C_i^{aq} are the gas phase and aqueous phase equilibrium concentration of the component i, respectively. From the equilibrium constant the solvation free energy can be extracted as shown in Equation:

$$\Delta G_{solv} = R\,T \cdot \ln(K_H) \tag{1.2}$$

Where ΔG_{solv} is the solvation free energy, R is the ideal gas constant, and T is the system temperature.

Another measurement of the solvent effects is through the association/binding process, usually employed in biochemistry. In this case, classical experiments are performed to determine dissociation constants (K_d) using differential scanning calorimetry and isothermal titration calorimetry[160;152]. From these measurements, the solvation contributions can be recovered from a thermodynamic cycle with gas phase references[169].

It is important to mention that all these measurements are valuable information that can also serve as validation or calibration for computational techniques, which will be described in the following section.

1.2.2 Computational quantification techniques

In the field of computational chemistry, researchers have employed various techniques to characterize solvent behavior. These methods span a spectrum from the fully quantum description, force field based simulations, microsolvation methods, a combination of quantum mechanical and molecular mechanics (QM/MM), and implicit methods[71;173]. These methods exhibit a trade-off between the accuracy of energetics estimation (which requires higher computational resources) and the length and time scales of the modeled systems. When the energy description is at a high level of theory (with higher accuracy), large systems or longer simulation times are computationally prohibited. However, at a lower level of theory, they can effectively operate within large systems and simulation timeframes. First principle quantum calculations, while providing a high level of accuracy, can only account for a limited amount of atoms and timescales[199]. Among the quantum approaches, ab initio molecular dynamics (AIMD) represents a highly accurate, but also a very computationally costly approach. In the AIMD methods, the nuclei positions evolve over time, the energy is calculated quantum mechanically, and as the system evolves, polarization and charge-transfer effects are explicitly taken into account[80]. This quantum description offers an accurate estimation of the energetics, but it is still limited to small systems (in the order of hundreds of atoms) and short running times (in the order of fs)[80;71]. These limitations are especially critical when modeling liquids, as the evaluation of equilibrium states properties requires sampling considering long-range interactions or long-time correlation behavior[173;170;196].

Force field based simulations from molecular mechanics (MM) offer longer simulation times and larger systems can be handled (in the order of a hundred thousand atoms) but are limited to the accuracy of the force field, the incorporation of polarization effects, and with the force field transferability (i.e. the capacity of the force field to be used in systems for which it was not originally fitted)[162;204]. Another key aspect of calculating thermodynamic

properties is the sampling. These simulations are typically constrained to sampling times in the order of ns. While for smaller systems sampling is usually enough, larger systems, like the case of protein simulations, obtaining a proper sampling can be challenging. This is because in large systems, a large number of local minima can be found and the system can become trapped and fail to execute ergodic sampling across configuration space[120;206;31].

In microsolvation methods, the solute electronic energy is estimated with standard QM accuracy with the inclusion of a small number of explicit solvent molecules (usually limited to the first solvation shell), with the possibility of the inclusion of implicit solvation[118;191;192]. Although these methods are efficient in terms of the energetics involved in the enthalpic component of the free energy, they are not able to properly capture the entropic component of the free energy or the enthalpic component when a larger amount of water molecules is required in the estimation of the energetics.

QM/MM combines some of the advantages of both the quantum and the molecular mechanics descriptions. In these methods, the simulated system is divided into two regions[20]: one active region treated at the QM level and an environment region treated at the MM level. By incorporating the QM treatment into the simulation, the estimation of free energies is typically improved compared to purely MM approaches[177]. However, they sometimes suffer from convergence issues in the QM region, they are still very computationally demanding, and suffer from limitations from the number of solvent molecules required to properly describe the active region[177;128;226].

In the case of implicit solvation models, a QM or MM solute is placed in a cavity surrounded by a continuum dielectric description of the solvent[215;136;183]. The solvation free energy is accounted by two components: an electrostatic component and a cavitation term. Although these methods are computationally efficient compared with other methods their

results suffer from some limitations. For instance, they are unable to properly capture hydrogen bonds[193]. Furthermore, in most implicit solvation models, the solvation free energies exhibit a "symmetry" with respect to the ion charge regardless of its sign. In other words, implicit solvation models (if not specially accounted) estimate equal solvation free energy for ions with the same charge but opposite signs (e.g. +2 or -2 ion charges). However, in reality, these energies often differ[165]. The cavity component, if accounted, is usually estimated by computing the accessible surface area and a factor derived from the experimental solvation energies of small nonpolar molecules[58;26]. The non polar contribution that falls into the cavity term, can lead to differences between the explicit methods and experimental data[218]. These assumptions make implicit solvation methods suffer transferability problems to different environments from those in which they were originally developed.

1.3   Challenges and opportunities

In Section 1.2.2 the most popular methods in computational chemistry used to estimate the solvent effects were briefly described. While all of them exhibit their own strengths and weaknesses there is no "do it all" method and significant efforts have to be placed in the selection and implementation of the appropriate technique to the system of interest. As each system has its own chemical behavior that will demand different levels of accuracy or sampling.

Considering the different advantages and disadvantages of these sets of methods, multiscale techniques have become an interesting route, combining the strengths of two (or more) of these techniques to refine the estimations of the solvent effects. Some of these efforts to improve estimation methods for solvation free energies are the following examples. Carine Michel and coworkers[193] proposed a hybrid approach that combines molecular mechanics and quantum mechanics to estimate the free energy. In their method, the free energy is

estimated primarily using MM, but the solute's polarization effects are considered at the QM level. Steven Lustig[165] uses a multiscale solvation-layer interface, taking into account the atomic radii for the first solvation shell to improve the regular estimates of a continuum solvation model. Heyden and coworkers[52;51] developed an implicit solvation model for solid surfaces that combines periodic with cluster model Density Functional Theory (DFT) calculations, adapting the implicit solvation scheme to account for the long-range metal interactions. Finally, another more recent approach is the incorporation of Machine Learning (ML) potentials trained with QM data into molecular dynamics simulations to improve the accuracy of the force fields and take advantage of the more computationally efficient MM approach, allowing longer simulation times[61;27;21]. Despite the many options available for modeling solvent behavior, these models are typically designed for (simply) solvation scenarios. However, they are not equally developed for conditional solvation. Conditional solvation introduces additional complexity as a result of the long-range interactions between solvent molecules and the interface[50], creating an environment distinct from the bulk phase. Further, the limited availability of experimental and theoretical studies and, to some extent, the inherent intricacy of the interfacial systems[217], make the modeling and estimation of conditional solvation even more challenging.

1.4 Potential applications

1.4.1 Application to heterogeneous catalysis

One type of interface of interest is the solid-liquid interface that occurs in heterogeneous catalysis. For this application tuning the reaction environment surrounding a catalyst active site is the heart of catalysis design, with the use of solvents being a common strategy[117]. Hence, a grand challenge in catalysis research is understanding the specific ways that solvents influence catalytic chemistry[38]. The aqueous environment plays multiple roles in the

catalysis, such as modifying thermodynamic and kinetic quantities,[72;210] altering the dominant reaction pathways,[117;116;176] and participating in the mechanism, e.g., via site blocking[130], modification of the active site,[190;223] and mediating hydrogen transfer[140;117]. For instance, solvents can alter active site chemistries[98;180] and coverages[192;142], modify reaction energetics[52;179;50;176], stabilize intermediate species[139;193;30] and transition state[18] structures, promote certain reaction paths[72] and mechanisms[174;184], and ultimately influence catalytic outcomes[72]. While significant research has been performed to elucidate these roles of solvent, intuition about how solvents will influence any particular catalytic system remains unknown. This is because solvent effects vary greatly depending on the catalytic interface[33;5].

Aqueous Phase Reforming as a test reaction

The dependence of interfacial properties becomes particularly important for reactions that utilize different types of active sites. An example of such a reaction is aqueous phase reforming (APR), which is a process that can produce hydrogen from derivatives of biomass under liquid water solvent[43;34]. This is an attractive process because biomass is an important energy source for the transition to a more sustainable energy market. Among biomass products, hydrogen is an emerging alternative to fossil fuels with environmental and economic benefits[164;158]. Hydrogen derived from biomass is particularly promising for biorefining[148]. The hydrogen that is produced can be used in other biorefinery reactions such as hydrodeoxygenation[194]; it can also be used in Fischer-Tropsch synthesis[81] or to produce electricity[181].

In the APR oxygenate species or sugars such as saccharides and polyols are converted into hydrogen[65]. APR employs a metal catalyst, typically over metal oxide or carbon-based supports[103;166;43;29] and an aqueous phase environment[34]. The APR mechanism comprises three sub-processes, i.e., dehydrogenation, decarbonylation, and water gas shift (WGS)[67;34;115]. Typical reaction conditions are temperature $\sim$500 K, pressure between 10-50 bar, and feedstock concentration between 1-10%[43]. Some industrially relevant feedstocks are ethanol[197],

glycerol[129], ethylene glycol[195], sorbitol[64], sucrose[63], and glucose[157]. However, the broader adoption of APR technology is inhibited by low H_2 (g) yields and catalyst deactivation[34;76].

Interestingly, in this type of supported metal systems, both sites on the metal interface (terrace sites) and at the metal/support interface (perimeter sites) have been shown to be relevant to the observed chemistry[3;205;78]. A commonly used system for APR is platinum supported on alumina (Pt/Al_2O_3) due to its relatively high yield and selectivity toward hydrogen[34;29]. However, the ways that these two types of sites (terrace and perimeter sites) promote the APR mechanism are different, even in the absence of solvent. For example, molecules tend to bind more strongly at perimeter sites than at terrace sites[74;224], due to the presence of undercoordinated metal atoms at perimeter sites. Furthermore, metals in the support at perimeter sites can provide additional anchoring sites[211], hence providing a richer active site environment[124].

Moreover, solvents interact differently with these two types of sites as well. Specifically, metal sites are relatively hydrophobic[122], whereas metal oxide supports generally comprise ions which are more attractive to solvent molecules[138;178;6]. The more attractive interface leads to differences in molecular and structural solvent phenomena. For example, H_2O molecules adsorb more strongly to more hydrophilic interfaces than to more hydrophobic interfaces, which leads to larger water densities near the interfaces of more hydrophilic surfaces[6;79;154]. These larger densities result in reduced mobilities for interfacial H_2O molecules[62;88], which influence the free energies[125] of interfacial processes such as catalysis. Indeed, the kinetics of APR have been observed to be different at perimeter sites compared with terrace sites, with these differences being attributed to the different roles of water in these two types of sites[78]. However, the specific ways in which water solvent influences APR at terrace versus perimeter sites remain unknown.

In fact, this information is unresolved even for the simplest oxygenate, methanol. This is despite decades of research into the mechanism of methanol decomposition due to its importance to electrocatalysis[95], direct fuel cells[2], and CO_2 reduction[209], in addition to APR. Prior research suggests that interactions between water and the alumina support influence the chemistry. Specifically, our groups[78] showed that large metal particles are more active for aqueous phase methanol dehydrogenation than small metal particles, suggesting that the reaction is favored on the more highly coordinated metal sites, i.e., on metal terraces, than on the undercoordinated sites at the metal/support perimeter. We further showed that the presence of water inhibits activity on small metal particles but has no effect on the activity of large metal particles. However, the mechanistic reasons for this remain unresolved. Multiple groups have shown using molecular simulations that the reaction mechanism for dehydrogenation is different on terrace sites than it is on perimeter sites in gas phase[45;59;211], and our groups have shown that in the aqueous phase, the strongly bound water layer destabilizes interfacial species due to a cavity effect[25]. However, how this influences the mechanism and rate of methanol dehydrogenation remains to be resolved.

1.4.2 Application to ion-Ligand capture

Rare earth elements (REEs) are important metals that have been widely used in many industrial applications like electronics, manufacturing, medical science, lasers, optical glass, and fiber optics among others[9]. Moreover, REEs can be found in diverse sources, such as industrial process residues. Notable examples include phosphogypsum, bauxite residue (red mud), mine tailings, metallurgical slags, coal ash, incinerator ash, and wastewater streams[8]. The abundance of these sources makes the extraction and recovery of REEs an attractive

11

area of study for economic and environmental reasons. Until recently, their extraction, separation, and purification are usually performed via chemical extraction and physical methods, but these techniques are either inefficient or environmentally damaging[90;87]. In the last decade, it has been established that bacteria can incorporate Lanthanides in the active site[42], and chemists have used this biological naturally Lanthanide-binding protein, Lanmodulin (LanM), to capture rare earth elements[73]. LanM is an EF-hand-containing protein with four predicted EF-loops[32]: EF-1, EF-2, EF3, and EF-4 with possible binding sites for the ion capture process. LanM exhibits a high affinity for the early (+3) Lanthanides over other ions with similar ionic radius such as Ca (+2)[126]. Notably, experimental evidence has revealed that the EF-1 loop exhibits the highest affinity for both calcium and lanthanide ions[214]. This selectivity is probably due to electrostatic interactions with the ligand, which are larger than the +1 and +2 ions, competing for the binding sites in the ligand[4]. However, until this date, the use of proteins for ion capture is not yet suitable for economic reasons at low concentration levels[93;213]. Therefore, an improvement of the current state of the ligands is needed, which can maximize the reusability and the capacity to selectively extract and concentrate the REEs with low-concentration feedstocks.

1.5 Dissertation Outline

This dissertation comprises two applications in which the estimation of solvent effects plays a crucial role in describing the physicochemical processes. The first application focuses on biomass conversion in heterogeneous catalysis, while the second application involves ligand-based capture of rare earth elements. Both applications occur under aqueous conditions. The first (Chapter 3) and second (Chapter 4) technical chapters are dedicated to the first application and the third (Chapter 5) technical chapter is dedicated to the second application. The first technical chapter is dedicated to the quantification of the solvation

thermodynamics in the Pt/Al_2O_3 catalyst. The second technical chapter is dedicated to elucidating the reaction mechanism for methanol dehydrogenation at the Pt/Al_2O_3 catalyst. In the third technical chapter, analogous techniques used for the estimation of solvation thermodynamics are employed to estimate the ligand-ion-capture process thermodynamics to understand the driving force of this separation.

Chapter 2: Methodology

For this dissertation, the target thermodynamic quantities are divided between the different applications.

For the first application on heterogeneous catalysis two types of interfaces are simulated $Pt(111)$ (terrace sites) and Pt/Al_2O_3 (perimeter sites). For these two systems, the following types of quantities are calculated using DFT in the gas phase: reaction energies (see Section 2.1), activation barriers (see Section 2.1.4), and atomic charges (see Section 2.1.4). Solvation thermodynamics are calculated, using explicit water, by a multiscale sampling technique combining DFT calculations and MD simulations (see Section 3.2.1). The solvation thermodynamics is divided into three quantities, the free energy, the enthalpic component, and the entropic component. The entropic component is calculated by MD simulations subtracting the enthalpic component (ΔE_{int}^{MD}, see Section 2.2.1) from the free energy from MD (ΔF_{sol}^{MD}, see Section 2.2.1). The enthalpic component of the free energy is estimated by DFT (ΔE_{int}^{DFT}, see Section 3.2.1) and the free energy is obtained by combining the entropic component from MD and the enthalpic component by DFT.

For the second application for the ion-ligand capture process, two types of system are simulated. The first system is where the ion is placed in a water solution, and the second system is where the ion is bound to the ligand in a water solution. With these two systems, a thermodynamic process is proposed to capture the thermodynamics of the ion-ligand capture process (see Section 5.2.1). For these processes, the thermodynamic quantities are estimated

by MD, the free energy according to Section 2.2.2, the enthalpic component according to Section 2.2.2, and the entropic component is calculated by the subtraction of the enthalpic component from the free energy.

2.1 Density Functional Theory simulations

2.1.1 General settings

Density Functional Theory (DFT) calculations are performed using the Vienna Ab initio Simulation Package (VASP)[107;105;106] using PAW 2002 pseudopotentials[143;108], the PBE exchange-correlation functional[150;151], and D3 dispersion corrections with Becke-Johnson damping[69;70]. Plane waves are included to an energy cutoff of 400 eV, spin polarization is turned on, and dipole corrections are applied in the direction normal to the surface. Gamma-centered Monkhorst Pack[141] k-point meshes are used in all DFT calculations. Electronic energies are calculated self-consistently and considered to be converged when the difference between subsequent iterations falls below 10^{-6} eV. Geometries are considered converged when the magnitudes of the forces on all atoms allowed to relax fall below 0.05 eV/Å.

2.1.2 Gas phase structures

DFT calculations for gas phase molecules follows the settings of Section 2.1.1 with the following changes. Calculations for gas phase molecules used a unit cell with lengths of 20 Å $\times$ 20.1 Å $\times$ 20.2 Å and only one gas phase species per unit cell. Electronic energies are calculated self-consistently and considered to be converged when the difference between subsequent iterations falls below 10^{-6} eV. All atoms in the supercell are allowed to relax. Gamma-centered Monkhorst Pack[141] k-point with mesh of $1 \times 1 \times 1$ is used for all gas phase molecules.

2.1.3 Platinum/alumina simulation supercells

Pt terrace and Pt/Al_2O_3 perimeter sites are modeled with a platinum (111) slab and a platinum particle supported on an alumina slab, respectively. Pt(111) terrace site models are taken from our prior work[18] and the details are summarized below. Pt/Al_2O_3 perimeter site models are constructed as follows. Under liquid H_2O, Al_2O_3 can develop a coverage of OH* groups due to H_2O dissocation[154;171]. However, as determining the extent of hydroxylation requires calculating the surface free energy and then performing thermodynamic and/or kinetic modeling, evaluation of a hydroxylated surface is reserved for future work. Hence, Pt/Al_2O_3 models in this work utilize a pristine Al_2O_3 slab. They are constructed as follows. Al_2O_3 slabs are built by cleaving a (0001) surface from the structure of bulk α-Al_2O_3 (space group = R$\bar{3}$c), which has a calculated lattice parameter of 5.178 Å, in agreement with a previous computational study[96]. Two periodic supercells are employed, one smaller and computationally efficient for the DFT calculations and a second larger supercell that more accurately captures interfacial phenomena for the MD simulations. Dimensions of the DFT and MD supercells are a = b = 10.3 Å and c = 32.7 Å and a = b = 15.5 Å and c = 53 Å, respectively. Supercell angles for both cells are $\alpha = \beta = 90°$ and $\gamma = 55.3°$. Pt nanoparticles are modeled with tetrahedrally shaped Pt_4 particles constructed on the tops of the α-Al_2O_3 slabs, following our prior work[211]. Energies and entropies of solvation calculated using these small Pt_4 particles are compared against analogous values calculated using Pt_8 particles and Pt_{20} and Pt_{48} nanorods in Supporting Information of Ref[25]. We find that when the adsorbate geometry and partial charge are held constant, the Pt particle size has a nearly negligible influence on the calculated energies and entropies of solvation; however, when the adsorbate partial charge and geometry are changed, it can influence the calculated entropy of solvation. We find the calculated partial charges have a maximum 0.2 meV/K influence on the calculated entropies of solvation. At 300 K, this results in a 0.07 eV uncertainty in

the free energy of solvation, which is within the standard error due to the method[49] as well as the configurational variability caused by thermal disorder in the liquid structure[18;222]. Further, we find that variation of partial charges in the adsorbates is not systematic and hence not due to small particle size effects (see the model validation sections in Supporting Information of Ref[25]). Variation of adsorbate geometry is related to the specific adsorption site structure at the Pt/Al_2O_3 interface and hence also not due to small particle size effects. We find that variation in the adsorbate geometry has a maximum 0.4 meV/K influence on the calculated entropies of solvation, which results in a 0.11 eV uncertainty in the free energy of solvation at 300 K, which is also within the uncertainty expected by the MSS method.

Adsorbates are added to the supercells near or on the Pt particles. The closest distances between adsorbates in neighboring periodic images are 8 Å and 13 Å for the DFT and MD supercells, respectively. In prior work we found that lateral interactions between adsorbates at these neighbor distances contribute less than 0.10 eV to the calculated energetics[211]. H_2O molecules are added to the supercells using the MCPliQ code[19]. Specifically, 50 to 60 H_2O molecules are added to the DFT cells, depending on the vacuum volume remaining after the adsorbate is added. The resulting water column heights are 14–15 Å, which guarantee at least three solvation shells[172]. Similarly, 182 to 188 H_2O molecules are added to the MD cells, resulting in water column heights of 30 Å. An additional 14 Å of vacuum space is included at the top of the water columns in all supercells.

2.1.4 Transition States calculations

Transition States (TS) searches are carried out using a combination of the climbing image nudged elastic band (CI-NEB)[84;83] and dimer methods[82;86]. Atoms in the TS structures as well as the top two surface layers are allowed to relax in terrace site calculations, and TS structures and the Pt cluster are allowed to relax in perimeter site calculations. TS

structures are verified via their calculated vibrational modes, which are calculated using the center difference method where atoms are displaced by 0.015 Å in the $+$ and $-$ directions in the a, b, and c dimensions. TS searches are performed using Γ-centered Monkhorst–Pack k-point meshes[141] of $3 \times 3 \times 1$.

2.1.5 Charge calculations

Partial charges are calculated from the converged structures using the DDEC6 atomic population analysis method[121].

2.2 Classical Molecular Dynamics simulations

Two sets of Classical Molecular Dynamics (MD) simulations settings are used depending on the system. For the systems in Section 3 the Section 2.2.1 settings apply and for the systems in Section 5 the Section 2.2.2 settings apply.

2.2.1 LAMMPS

Molecular Dynamics (MD) simulations are performed with the Large-scale Atomic/Molecular Massively Parallel Simulator (LAMMPS)[159]. All MD simulations are carried out at 300 K. In all MD simulations, H_2O molecules are allowed to move, while positions of surface, catalyst and adsorbate atoms are held fixed. Following addition of H_2O molecules using MCPliQ[19], an initial geometry relaxation is performed to refine the initial water configuration and then the simulation of interest is carried out.

NVT simulations used to generate water molecule configurations

NVT simulations are carried out to obtain configurations of H_2O molecules for calculating ΔE_{int}^{DFT}, ΔE_{int}^{MD}, the sizes of the cavities created by the adsorbates, and the average number of hydrogen bonds formed between H_2O molecules and the adsorbates. In all these simulations, temperature is maintained with the Nose–Hoover thermostat[147;89], a 1 fs time step is

18

employed, and the first 5 ns of the simulation are used for system equilibration. Production runs and sampling frequencies for the various quantities are as follows. Production runs for generating configurations of H_2O molecules used to calculate ΔE_{int}^{DFT} int are 3 ns long, and configurations are sampled every 0.3 ns (resulting in a total of 10 configurations). As 0.3 ns is significantly longer than hydrogen bond lifetimes of oxygenate species[18], this sampling frequency ensures that these 10 configurations are uncorrelated. The ensemble average for ΔE_{int}^{DFT} int is then calculated by evaluating Equation 2.

Production runs for generating configurations of H_2O molecules used to calculate ΔE_{int}^{MD} are 5 ns long, and configurations are sampled every 0.001 ns. The ensemble average is obtained by computing the average energy of interaction between the H_2O molecules and the adsorbate. Production runs for generating configurations of H_2O molecules for computing adsorbate cavity sizes are 9 ns long, and configurations are sampled every 0.01 ns. The cavity size is approximated as the number of equivalent H_2O molecules that are displaced by the adsorbate. Hence, the ensemble average is taken as the average number of water molecules within 12 Å of the surface when the adsorbate is not present (calculated from the density of water in that region) minus the average number of water molecules within 12 Å of the surface when the adsorbate is present. Finally, production runs for generating configurations of H_2O molecules used to calculate the average number of hydrogen bonds between H_2O molecules and adsorbates are 9 ns long, and configurations are sampled every 0.3 ns. The ensemble average is calculated by averaging the number of H_2O molecules that fit geometric criteria for hydrogen bonding[131], i.e., the O_{H_2O}-$O_{Adsorbate}$ distance ≤ 3.5 Å and either the O_{H_2O}-$O_{Adsorbate}$-$H_{Adsorbate}$ or O_{H_2O}-$O_{Adsorbate}$ H_{H_2O} angle ≤ 30. Using this criterion, both hydrogen bond donors and acceptors are counted.

Force fields and parameters for platinum/alumina systems

Following our prior publication[220], interactions between H_2O molecules and catalyst and adsorbate atoms are calculated using Lennard-Jones plus Coulomb potentials, where the long-range Coulombic interactions are captured using the Particle Particle Particle Mesh (PPPM) method[23]. Lennard-Jones parameters for adsorbate atoms are taken from the OPLS-AA[40] force field. Lennard-Jones parameters for Pt atoms are obtained using a modified version of the United Force Field (UFF)[168] (see below). Lennard-Jones parameters for the Al_2O_3-H_2O interaction are taken from a force field parameterized from DFT data by Ciacchi et al[119]. This force field was shown to produce water structures in agreement with DFT when coupled with the TIP3P water model[119]; hence, Lennard-Jones parameters for H_2O molecules are taken from the TIP3P/CHARMM[132] water model. Arithmetic mixing rules are used for H_2O-H_2O and H_2O-Pt interactions, while the remaining interactions employ geometric mixing rules. It has been shown that calculated enthalpies, entropies, and free energies of hydration are sensitive to the water model that is employed[186;85]. In the MSS method, energies of solvation are computed with DFT. Hence, the water model is more likely to influence entropies of solvation. We find that the choice of water model gives a maximum 0.2 meV/K difference in the calculated entropies of hydration. At 300 K, this results in a 0.05 eV uncertainty in the free energy of hydration. Further, we previously showed that free energies of solvation for constituents of sugar alcohols and ammonia on Pt(111) calculated using the MSS method where the MD simulations employed the TIP3P/CHARMM water model were in excellent agreement with free energies of solvation calculated with implicit solvation for adsorbates that do not form strong hydrogen bonds with H_2O (i.e., which can be appropriately modeled with implicit solvation[220]). These results suggest that the water model has a minor influence on the calculated solvation thermodynamics for the species

studied herein; however, the influence likely becomes more dramatic as the hydration energy becomes stronger.

Free energy perturbation calculations

ΔF_{sol}^{MD} are calculated using the methods of Free Energy Perturbation (FEP) and thermodynamic integration, following ref.[198;112;161;75] and our prior work[220]. In these methods, a solute is "grown" in a solvent over the course of a NVT simulation by gradually "turning on" the interaction between solvent and solute. A thermodynamic integration is performed on the energy of the system to compute ΔF_{sol}^{MD}. In this work, the general strategy is that the solute is the adsorbate, and the solvent is H_2O. During the FEP simulations, Leonard-Jones parameters and Coulomb charges are scaled (with coupling parameter λ) for the adsorbate. The Pt particle and Al_2O_3 slab are not scaled. Rationale for this modeling choice is discussed in Supporting Information of Ref[25]. Scaling is performed in 50 steps, following the suggestion of Chipot[161]. For each step, an NVT simulation is performed for 300 ps, which yields a total simulation time of 15 ns (including separate scaling of the Lennard-Jones and Coulomb contributions to the energy[161]).

2.2.2 GROMACS

Simulation settings

Molecular Dynamics (MD) simulations were carried out using the GROMACS package[189] version 2020.5. The CHARMM force field was selected to model the ligand and ions[36]. Water molecules were treated with the SPC/E force field model[188]. A simulation box with $5 \times 5 \times 5$ nm^3 dimensions was used, giving a distance between neighboring ligands around 3.2 nm. Simulations used a leap-frog stochastic dynamics integrator[66]; and were carried out at 1 bar and 300K using the Berendsen thermostat and Parrinello–Rahman barostat respectively[15;149]. Particle Mesh Ewald[41;48] was used for long-range nonbonded electrostatic

interactions. Van der Waals interactions were treated with a cut-off with a pair list radius of 2.0 nm and a cut-off distance of 1.2 nm. Systems with a net non-zero net charge are simulated with a homogeneous background counter charge[91;200].

Equilibration

Prior to the free energy calculations and enthalpy estimation, a pre-equilibration for the structures with the ligand is performed. This consists of an energy minimization step, 100 ps of an NVT run, an initial 50 ps of an NPT run, and a longer 5 ns run at an NPT ensemble, all of this with a 1 fs of time step. Equilibration and convergence are confirmed via the radius of gyration and the total energy, an example of the convergence of the gyration and the total energy is provided in Figure 2.1. The convergence of the equilibration run can be verified with a value close to zero on the slope monitored variable (the radius of gyration or the total energy) versus time, as indicative of stationarity.
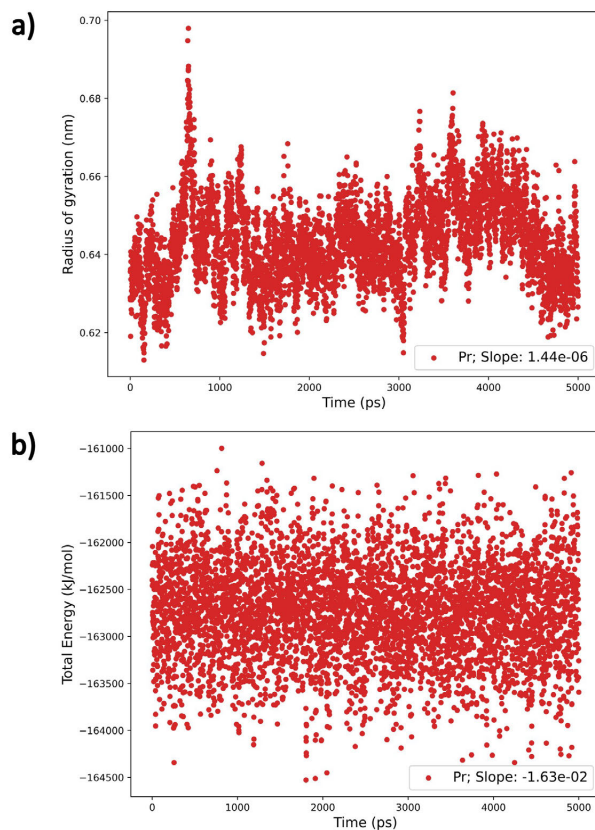
Figure 2.1: Convergence verification in the equilibration run of Pr in the bound state. a) Radius of gyration. b) Total energy. The slopes between the monitored variable versus time are shown in the plot legends. A value close to zero is taken as indicative of stationarity of the time series and equilibration convergence.

Free energy calculations

Free energy calculations are calculated using the free energy perturbation method[28;161;203]. In this approach, a coupling parameter (λ) turns off the pair interactions between the ion and the rest of the system for the Coulombic and van der Waals components. This calculation involves sampling between linearly spaced states between the initial and final states, using 20 windows with a sampling of 0.5 ns in each window and softcore potentials[16] for the Coulombic and van der Waals components. The Bennett Acceptance Ratio[14] method is used for the calculation of the free energy differences.

For each window (with its respective λ state) a pre-equilibration process for the free energy calculation is performed as follows. First, an energy minimization step using the steepest descent algorithm[189] is performed. An NVT equilibration run for 50 ps followed by an NPT equilibration for 50 ps both with a time step of 1 fs are then performed. Finally, a production sampling on an NPT run for 50 ps, both with a time step of 1 fs are performed.

Estimation of the enthalpic component

The estimation of the enthalpic component is more demanding in terms of the sampling error compared to the free energy. The reason for this lies in the fact that average total energies tend to be large, and roughly proportional to the number of particles in the system. Hence, the estimation of even a small quantity, from the difference between two independently measured large numbers is less reliable than the estimation of the free energy[198]. For this reason, the estimation of the enthalpic component for the free energy decomposition (i.e. enthalpy and entropy components) requires longer simulations[137]. For these reasons, the sampling dedicated to the enthalpic component is longer and exhibits more sampling error. The estimation of the enthapic component as described in Section 5.2.1 is performed as the energy difference between the bound and the unbound state of the ion as follows:

$$\Delta H = \langle E_{\lambda=0} \rangle - \langle E_{\lambda=1} \rangle \tag{2.1}$$

Where ΔH is the enthalpic component of step 5.2 or step 5.3 (see Section 5.2.1), $\langle E_{\lambda=0} \rangle$ is the average total energy with the ion in the bound state, and $\langle E_{\lambda=1} \rangle$ is the average total energy with the ion in the unbound state. These two later quantities are calculated after the free energy calculations, specifically from the structures in the bound and unbound state. The ensemble average of these two quantities is performed as a longer NPT run for 20 ns at a time step of 2 fs running time and following the settings of the previous section 2.2.2.

Chapter 3: Differences in solvation thermodynamics of oxygenates at platinum/alumina perimeter versus platinum terrace sites

3.1 Introduction

The solvent interacts differently at the terrace and perimeter sites due to differences in the nature of the interfaces, and how these differences influence the APR is still unknown. In this work, we begin to fill this knowledge gap by computing free energies of solvation of APR intermediates on Pt/Al_2O_3 catalysts. We specifically investigate differences in solvation thermodynamics for intermediates in the pathway for methanol decomposition on $Pt(111)$ and Pt/Al_2O_3 slabs, which serve as models for terrace and perimeter sites, respectively. Solvation thermodynamics are calculated under explicit liquid water using our previously developed method of multiscale sampling (MSS)[19], which combines density functional theory (DFT) with classical molecular dynamics (MD). The MSS method is used to compute energies (ΔE_{int}^{DFT}), entropies (ΔS_{int}^{MD}), and free energies (ΔF_{solv}^{MSS}) of solvation of CH_3OH*, CH_2OH*, $CHOH*$, $COH*$, CH_3O*, CH_2O*, $CHO*$, and $CO*$ adsorbates (*'ed species indicate that they are adsorbed to the catalyst). Solvation thermodynamics of $H*$ and H_2O* are additionally computed for completeness. We find that the strength of the water-adsorbate interaction has a strong influence on adsorbate solvation thermodynamics in terrace and perimeter sites, but solvation entropy contributes more significantly to the solvation free

25

energy in perimeter sites due to the greater work needed to create cavities in the solvent structure at these more hydrophilic interfaces.

3.2 Methods

3.2.1 Solvation free energies

Solvation free energies are calculated using a combination of DFT and MD, following our prior work[220]:

$$\Delta F_{solv}^{MSS} = \Delta E_{int}^{DFT} - T\Delta S_{int}^{MD} \tag{3.1}$$

where ΔF_{solv}^{MSS} is the Helmholtz free energy of solvation calculated with Multi Scale Sampling (MSS)[220], ΔE_{int}^{DFT} is the water-adsorbate interaction energy calculated with DFT, and ΔS_{int}^{MD} is the water-adsorbate interaction entropy calculated with MD. A flow diagram illustrating how ΔF_{solv}^{MSS}, ΔE_{int}^{DFT}, and ΔS_{int}^{MD} are calculated is provided in Figure 3.1.
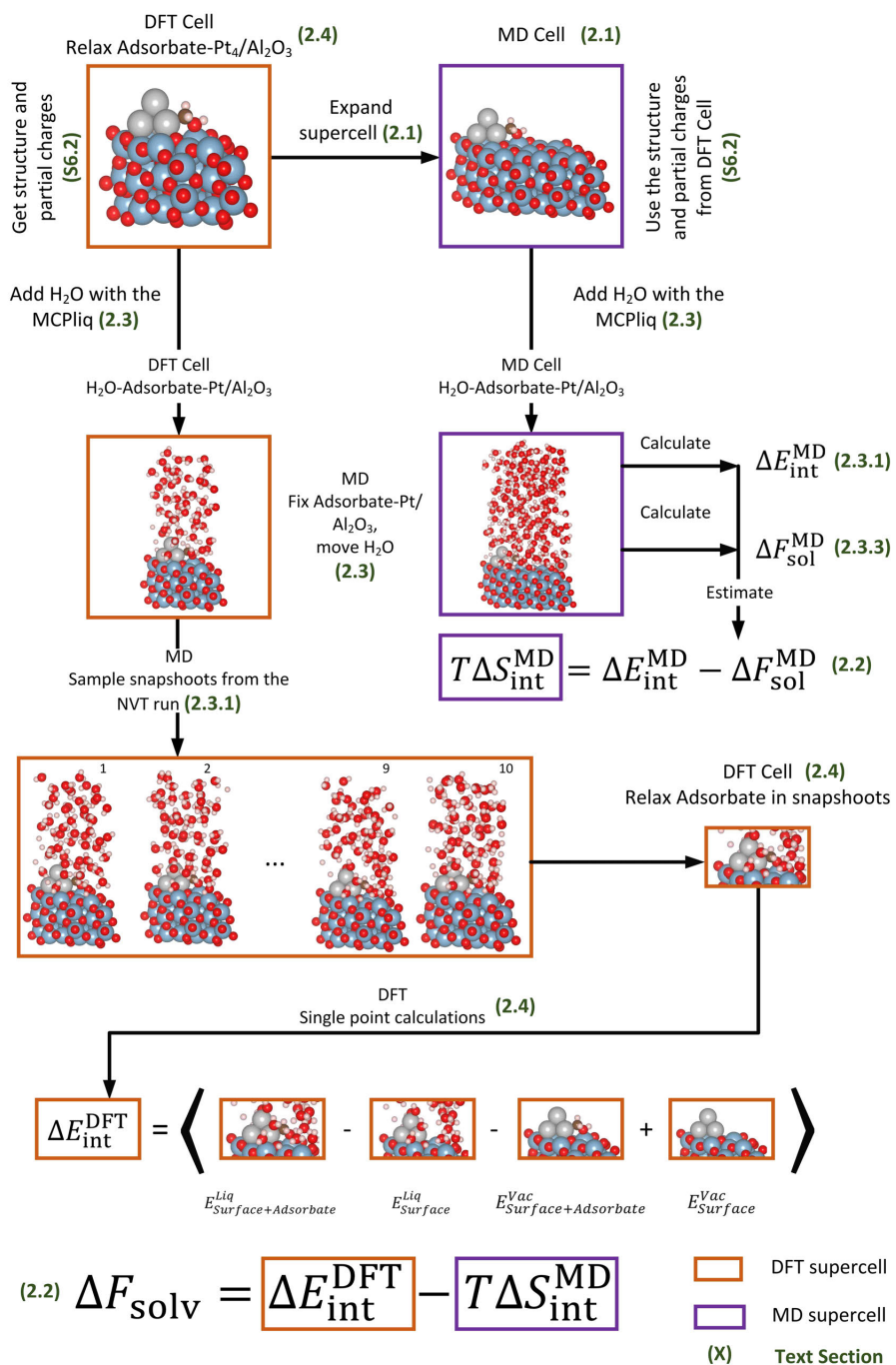
Figure 3.1: Flow diagram for the multiscale sampling method. NOTE: The related text sections shown in the green text can be found in Ref.[25]

A description of the procedure is as follows. Following construction of the Pt/Al_2O_3 models, adsorbates are added to the supercells and their geometries are optimized in DFT using initial guesses based on those published previously by our group[211]. H_2O molecules are then added to the supercell using the MCPliQ code[19]. Configurations of H_2O molecules are then obtained in the canonical (NVT) ensemble in MD. A tractable number of configurations is then sampled and used to compute ΔE_{int}^{DFT} following our prior work[19;220].

$$\Delta E_{int}^{DFT} = \langle (E_{Pt/Al_2O_3+adsorbate}^{liq} - E_{Pt/Al_2O_3+adsorbate}^{vaq}) - (E_{Pt/Al_2O_3}^{liq} - E_{Pt/Al_2O_3}^{vac}) \rangle \quad (3.2)$$

where $E_{Pt/Al_2O_3+adsorbate}^{liq}$ is the electronic energy (calculated with DFT) of the Pt/Al_2O_3 model with the adsorbate under liquid water, $E_{Pt/Al_2O_3+adsorbate}^{vaq}$ is the electronic energy of the Pt/Al_2O_3 model with the adsorbate in vacuum, $E_{Pt/Al_2O_3}^{liq}$ is the electronic energy of the Pt/Al_2O_3 model under the same liquid water structure as for $E_{Pt/Al_2O_3+adsorbate}^{liq}$ but with the adsorbate removed, and $E_{Pt/Al_2O_3}^{vac}$ is the electronic energy of the Pt/Al_2O_3 model without the adsorbate in vacuum.

$T\Delta S_{int}^{MD}$ is calculated from two separate MD simulations, following our previous publications[220;49]:

$$T\Delta S_{int}^{MD} = \Delta E_{int}^{MD} - \Delta F_{sol}^{MD} \quad (3.3)$$

where ΔE_{int}^{MD} is the average energy of interaction between the H_2O molecules and the adsorbate over an NVT trajectory, and ΔF_{sol}^{MD} is the Helmholtz free energy of solvation of the adsorbate, calculated using the method of free energy perturbation (FEP) in MD. Values used to compute $T\Delta S_{int}^{MD}$ are provided in Supporting Information[25] Table S12.

Values of ΔF_{solv}^{MSS} are compared with the analogous values calculated with implicit solvation in Supporting Information[25] Table S13.

3.3   Results

Calculated structures of adsorbates at the Pt/Al_2O_3 perimeter sites are shown in Figure 3.2. With the exceptions of CO∗, COH∗, and H∗, methanol and its derivatives bind O-down to Al ions. Adsorbates with non-fully saturated methyl groups additionally bind to the Pt cluster[211].
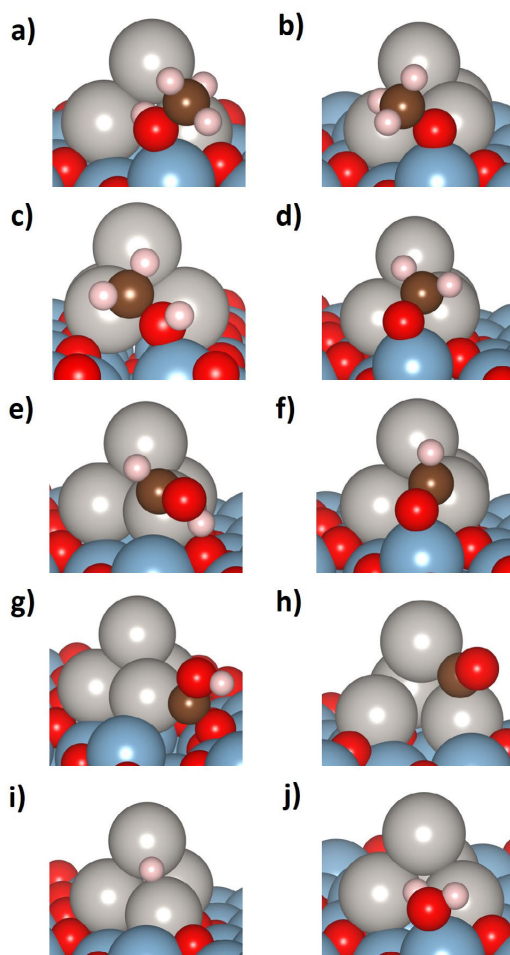
Figure 3.2:   Calculated adsorbate geometries in Pt/Al_2O_3 perimeter sites. a) CH_3OH* b) CH_3O* c) CH_2OH* d) CH_2O* e) CHOH∗ f) CHO∗ g) COH∗ h) CO∗ i) H∗ j) H_2O*. Pt = gray, O = red, C = brown, H = pink.

Calculated energies, entropies, and free energies of solvation for these adsorbates are presented in Figure 3.3; entropies are presented as $T\Delta S_{int}^{MD}$ to illustrate the extent to which they contribute to ΔF_{solv}^{MSS}. All adsorbates exhibit negative energies of solvation (except for H$*$, which exhibits a slightly positive ΔE_{int}^{DFT} that is ~ 0). All adsorbates also exhibit negative entropies of solvation, in line with our prior work[220]. Free energies of solvation are positive for all adsorbates except H$_2$O$*$, due to $T\Delta S_{int}^{MD}$ being more negative than ΔE_{int}^{DFT}. Specifically, alcohol adsorbates except for COH$*$ (i.e., CH$_3$OH$*$, CH$_2$OH$*$, and, CHOH$*$) have $\Delta F_{solv}^{MSS} \sim 0$ due to having $T\Delta S_{int}^{MD}$ that directly compensate ΔE_{int}^{DFT}, whereas aldehyde/CO$*$ adsorbates except for CH$_2$O$*$ (i.e., CH$_3$O$*$, CHO$*$, and CO$*$) have non-negligible ΔF_{solv}^{MSS} that are more positive than the corresponding alcohol adsorbates due to having large negative values of $T\Delta S_{int}^{MD}$. This trend of entropy of solvation compensating energy of solvation agrees with prior literature, which shows that energy and entropy of solvation are related[13;114;46] since the higher interaction between the solute and solvent increases the energy but at the same time restricts the motions of the solvent molecules, which leads to an entropy penalty[182;46]. Hence, entropies of solvation generally counteract energies of solvation.
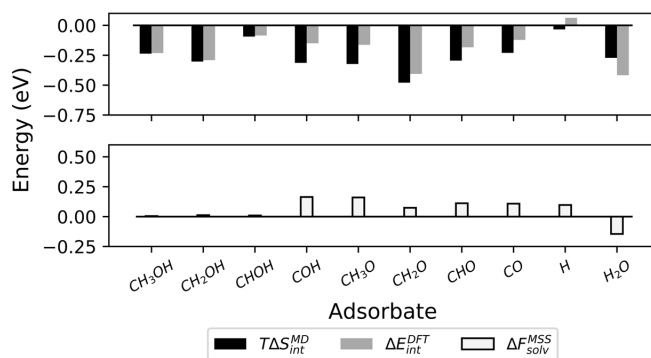
Figure 3.3: Calculated energies (gray bars and text), entropies (black bars and text), and free energies (white bars and black text) of solvation for methanol decomposition products on Pt/Al$_2$O$_3$ perimeter sites.

Calculated solvation thermodynamics are compared with the analogous values calculated on Pt(111) in Figure 3.4. In general, ΔF_{solv}^{MSS} are more negative on Pt(111) than on Pt/Al$_2$O$_3$. For alcohol adsorbates with the exception of CHOH∗ (i.e., CH$_3$OH∗, CH$_2$OH∗, and COH∗), this is because ΔE_{int}^{DFT} on Pt(111) are large and negative and outweigh TΔS_{int}^{MD}, whereas on Pt/Al$_2$O$_3$, ΔE_{int}^{DFT} are smaller and nearly equal to TΔS_{int}^{MD}. For aldehyde/CO* adsorbates (CH$_3$O∗, CH$_2$O∗, CHO∗, and CO∗), TΔS_{int}^{MD} outweigh ΔE_{int}^{DFT} on Pt(111) and Pt/Al$_2$O$_3$, with the effect being more pronounced on Pt/Al$_2$O$_3$. In fact, both ΔE_{int}^{DFT} and TΔS_{int}^{MD} are more negative for aldehyde/CO* adsorbates on Pt/Al$_2$O$_3$ than on Pt(111).
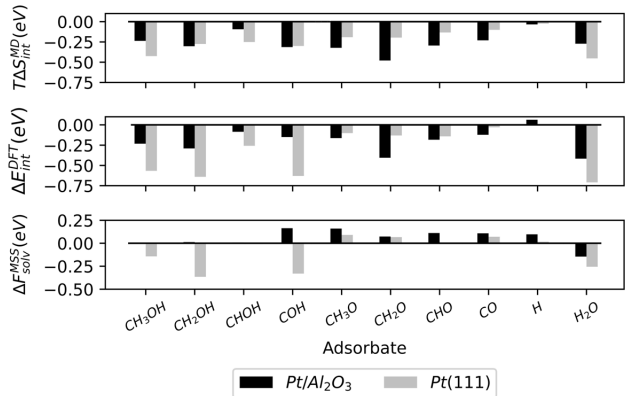
Figure 3.4: Comparison of solvation thermodynamics for terrace and perimeter sites Calculated entropies (top), energies (middle), and free energies (bottom) of solvation for methanol decomposition products on Pt/Al$_2$O$_3$ perimeter sites (black) versus Pt(111) terrace sites (gray).

Figure 3.4 shows that entropies of solvation contribute more to free energies of solvation on Pt/Al$_2$O$_3$ than on Pt(111). To explore this further, Figure 3.5 plots TΔS_{int}^{MD} vs. ΔE_{int}^{DFT} for methanol decomposition intermediates on Pt/Al$_2$O$_3$ (filled black triangles) along with the analogous values for 90 C1-C3 oxygenate species on Pt(111) (open gray circles; taken from ref.[221]). Best fit lines are also included for both datasets. On Pt(111), the slope of

$T\Delta S_{int}^{MD}$ versus ΔE_{int}^{DFT} is 0.50, which agrees with prior literature[46;179] as well as homogeneous solution theory[94]. The larger slope of 0.66 for Pt/Al_2O_3 suggests that $T\Delta S_{int}^{MD}$ contributes more significantly to ΔF_{solv}^{MSS}. Values of $T\Delta S_{int}^{MD}$ are well correlated to values of ΔE_{int}^{DFT} on $Pt(111)$ ($R^2 = 0.91$), indicating that the energy to entropy compensation[13;46] trend is preserved on this interface (this is true even when the sample size for $Pt(111)$ is smaller; see Figure S22 in the Supporting Information of Ref[25]). In contrast, $T\Delta S_{int}^{MD}$ are less well correlated to ΔE_{int}^{DFT} on Pt/Al_2O_3 ($R^2 = 0.62$), suggesting that other phenomena contribute to solvation enthalpies on Pt/Al_2O_3.
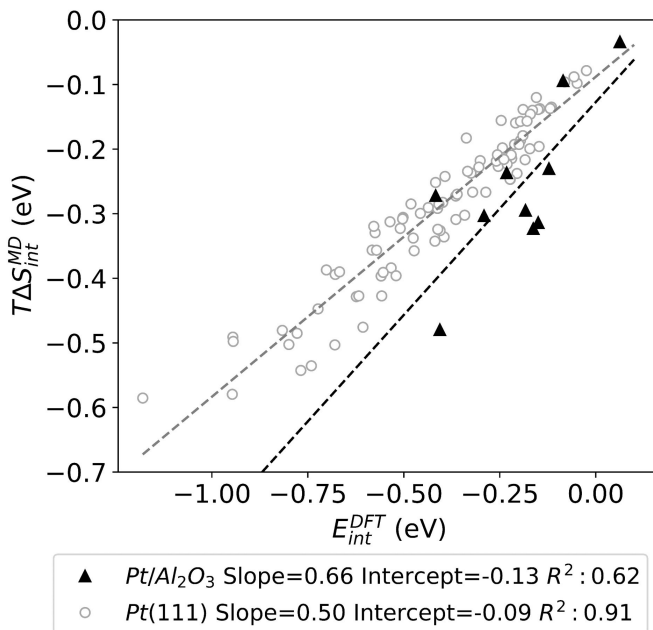
Figure 3.5: $T\Delta S_{int}^{MD}$ plotted against ΔE_{int}^{DFT} for adsorbates in Pt/Al_2O_3 perimeter sites (filled black triangles) and $Pt(111)$ terrace (open gray circles).

3.4   Discussion

The difference in relationship between $T\Delta S_{int}^{MD}$ and ΔE_{int}^{DFT} on Pt/Al_2O_3 versus $Pt(111)$ is caused by differences in properties for these two interfaces. Specifically, $Pt(111)$ is less

hydrophilic (exhibiting a H_2O molecule binding energy of 0.33 eV[156] versus 1.14 eV[167] for Al_2O_3), so solvation phenomena are largely controlled by the adsorbates themselves, resulting in the strong correlation between $T\Delta S_{int}^{MD}$ and ΔE_{int}^{DFT}. In contrast, Al_2O_3 is hydrophilic[208], and the weaker correlation between $T\Delta S_{int}^{MD}$ and ΔE_{int}^{DFT} suggests that other phenomena in addition to the strength of the adsorbate-H_2O bond, particularly the H_2O interaction with the Al_2O_3 interface, contribute to $T\Delta S_{int}^{MD}$.

To improve the understanding about solvation thermodynamics on Pt/Al_2O_3, we sought to identify the phenomena that influence $T\Delta S_{int}^{MD}$ on this interface. We showed in prior work[220] that $T\Delta S_{int}^{MD}$ on Pt(111) is related to loss of mobility/increase in "order" of H_2O molecules that form strong hydrogen bonds with adsorbates[220] (since hydrogen bonds hold the H_2O molecules in specific orientations with respect to the adsorbate and hence surface). Figure 3.6 shows that hydrogen bond formation either remains for the most part the same on Pt/Al_2O_3 (alcohol adsorbates except for CH_3OH*) or increases (aldehyde/CO$*$ adsorbates except for CHO$*$) compared to Pt(111). Applying the same rationale from our prior work[220], it is reasonable, then, that $T\Delta S_{int}^{MD}$ contributes more significantly to ΔF_{solv}^{MSS} on Pt/Al_2O_3 than on Pt(111). However, if this were the only contribution to $T\Delta S_{int}^{MD}$, we would expect better correlation between $T\Delta S_{int}^{MD}$ and ΔE_{int}^{DFT}, as on Pt(111). We hence investigated other phenomena that could contribute to $T\Delta S_{int}^{MD}$ on Pt/Al_2O_3.
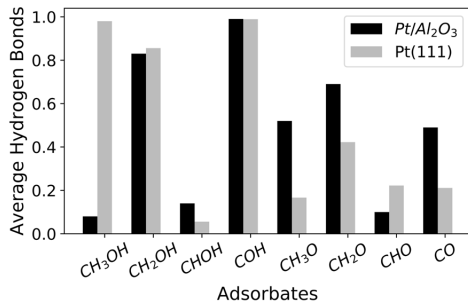
Figure 3.6: Comparison of hydrogen bond formation for adsorbates in Pt/Al_2O_3 perimeter sites (black bars) and Pt(111) terrace sites (gray bars).

We specifically investigated phenomena related to the hydrophilicity of the Al_2O_3 surface, including the H_2O molecule packing (see Figures S18 and S21 of Supporting Information from Ref[25].) and solvent compressibility. The solvent compressibility was particularly insightful. The higher hydrophilicity of Al_2O_3 leads to a lower compressibility of the interfacial H_2O molecules (see Table S15 of Supporting Information from Ref.[25]), which means that more work is required to create a cavity in the solvent[62,13], i.e., to accommodate adsorbates, on Pt/Al_2O_3 compared to Pt(111). One way to quantify cavity size is by the number of H_2O molecules that are displaced by the adsorbate. Figure 3.7 plots $T\Delta S_{int}^{MD}$ versus the number of displaced H_2O molecules for adsorbates on Pt/Al_2O_3 and Pt(111). On Pt/Al_2O_3, these two values are correlated ($R^2 = 0.63$), with adsorbates that exhibit larger cavities also exhibiting more negative values of $T\Delta S_{int}^{MD}$ (as with the strength of the adsorbate-H_2O interaction, the R^2 value of 0.63 suggests that other phenomena in addition to cavity size contribute to $T\Delta S_{int}^{MD}$). In contrast, there is no correlation between cavity size and $T\Delta S_{int}^{MD}$ for adsorbates on Pt(111) ($R^2 \sim 0$). These results suggest that there is a higher entropy penalty associated with cavity formation[124,60] on Pt/Al_2O_3 than on Pt(111). This entropy penalty decreases (makes more negative) the entropies of solvation on Pt/Al_2O_3. Furthermore, since this effect

is related more to the water-surface interaction rather than the water-adsorbate interaction (ΔE_{int}^{DFT}), it detracts from the correlation between ΔE_{int}^{DFT} and $T\Delta S_{int}^{MD}$, resulting in a lower R^2 value than on Pt(111). In other words, the strength of the water-adsorbate interaction determines the entropy of solvation on Pt(111), whereas both the strength of the water-adsorbate interaction and the cavity size determine the entropy of solvation on Pt/Al$_2$O$_3$.
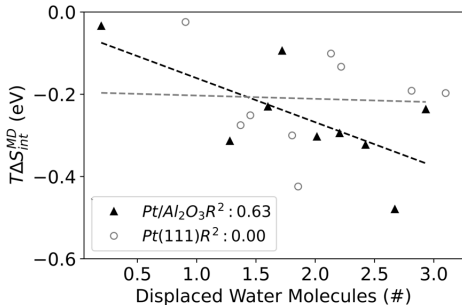
Figure 3.7: $T\Delta S_{int}^{MD}$ versus number of displaced H$_2$O molecules for adsorbates in Pt/Al$_2$O$_3$ perimeter sites (filled black triangles) and Pt(111) terrace sites (open gray circles).

3.5 Conclusion

These findings suggest that solvation thermodynamics on the terrace versus perimeter sites on Pt catalysts supported on Al$_2$O$_3$ are different. Specifically, while the solvation thermodynamics in Pt terrace sites depend almost entirely on the adsorbate and the strength of the hydrogen bonds that it forms with liquid H$_2$O molecules, interfacial properties have a strong influence on solvation thermodynamics of adsorbates in Pt/Al$_2$O$_3$ perimeter sites due to the higher interfacial hydrophilicity. This study illustrates how interfacial properties influence the solvation thermodynamics of adsorbed species and the significant role that entropy can play in the solvation thermodynamics of adsorbed species. The insight provided herein will help expand intuition about solvation thermodynamics of interfacial species, which will be helpful in catalysis and other fields.

Chapter 4: Active sites and mechanism of aqueous phase methanol dehydrogenation on platinum/alumina catalysts from multiscale modeling, microkinetic modeling, and operando spectroscopy

4.1   Introduction

There are multiple outstanding knowledge gaps about the mechanism of methanol APR. Towards the goal of closing these knowledge gaps, our objective in this work is to clarify the active sites and mechanism for methanol dehydrogenation on Pt/Al_2O_3 catalysts. To do this, we use a combination of multiscale simulations[18;220;211;25], microkinetic modeling, and Fourier transform infrared spectroscopy (FTIR)[78]. We show that the active sites for CH_3OH dehydrogenation are on the terraces of large Pt particles and that sites at the Pt/Al_2O_3 perimeter are inactive. This is because strongly bound H_2O* molecules inhibit CH_3OH* molecules from binding at the Pt/Al_2O_3 perimeter. Further, these H_2O* molecules protonate CH_xO* species at the Pt/Al_2O_3 perimeter, hence pushing the reaction in reverse. These effects do not occur on Pt terrace sites, and hence, the rate is only minorly affected by the aqueous phase. Interestingly, the mechanism on terrace sites is significantly impacted by the water solvent. Specifically, liquid H_2O molecules promote significant stabilization of CH_2OH* and $COH*$ species, which forces the mechanism through a $COH-H_2O*$ intermediate that alters the equilibrium between $COH*$ and $CO*$.

4.2   Methodology

4.2.1   Models

Making comparisons between experiments and theory requires constructing models that can be used along with experimental observations to explain the observed behavior. To complement this work, our collaborators[78] performed FTIR experiments on both "large" and "small" Pt particles, which have average particle sizes of 4.6 nm and 1.0 nm, respectively. Both particle sizes comprise sites on Pt terraces as well as at the Pt/Al_2O_3 perimeter (Figure 4.1). However, the larger Pt particles will have a greater fraction of terrace sites whereas the smaller Pt particles will have a greater fraction of perimeter sites. Hence, differences in activity between the two particle sizes, along with insights from modeling, can be used as a probe of the relative activity on terrace versus perimeter sites. Following prior work[211,25], we use a Pt(111) slab to model terrace sites and a Pt cluster anchored to an Al_2O_3 slab to model Pt/Al_2O_3 perimeter sites. While this choice of models is a simplification of real nanometer-sized Pt particles on Al_2O_3, it allows for studying the extent to which interactions with the support affect the reaction path of methanol on Pt.
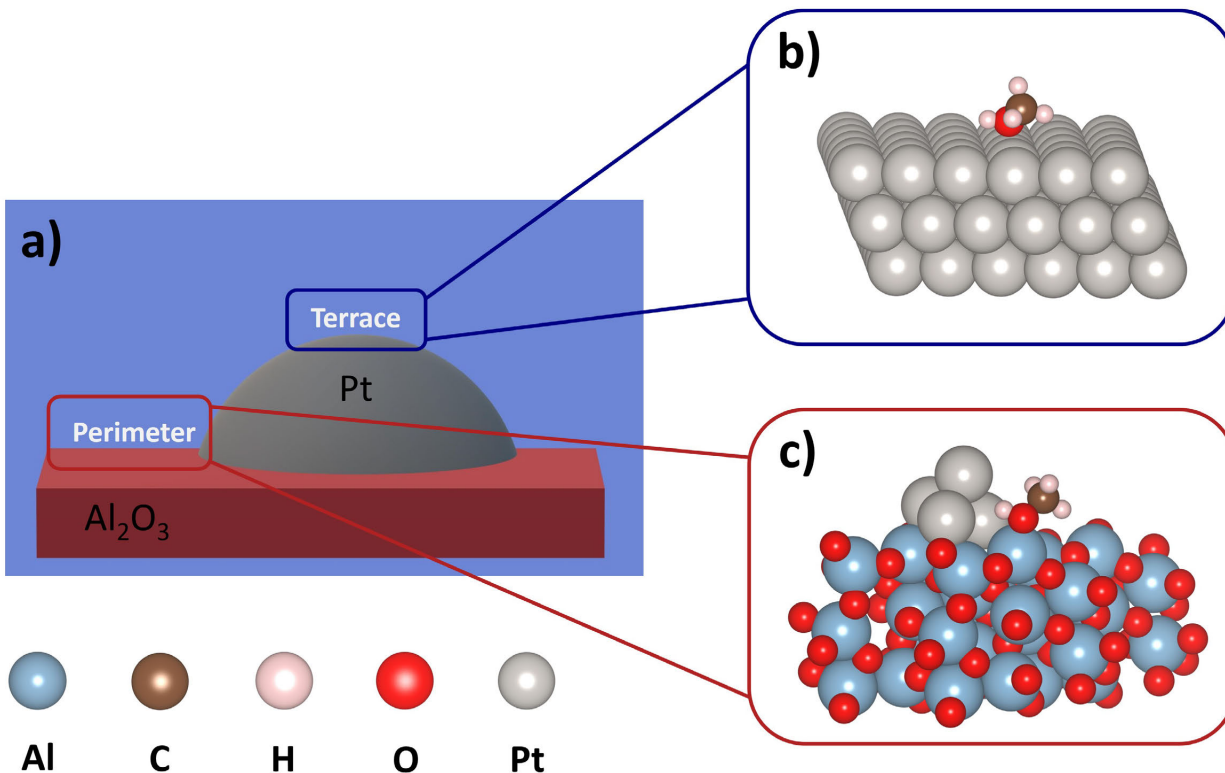
Figure 4.1: Pt/Al$_2$O$_3$ site models. a) Cartoon representation of a supported Pt catalyst. b) Terrace site model. c) Perimeter site model.

4.2.2 Microkinetic Modeling

Microkinetic modeling is carried out using the MKMCXX software[55;54;53]. The operation temperature is set to 500 K. The bulk phase concentration of CH$_3$OH is set to 10%. In gas phase models, an inert N$_2$ (g) gas comprises the remaining 90%, while water comprises the remaining 90% in aqueous phase models. The pressure is set to 1 bar in all models and remains constant over the simulation. In practice, APR is carried out near the vapor pressure of water at the reaction temperature, to maintain condensed phase conditions. In our modeling, condensed phase conditions are maintained using multiscale modeling with explicit liquid water[25]. Hence, the sole function of the pressure is to compute gas phase

collision frequencies for adsorption/desorption reactions. How these are modeled is discussed below. Microkinetic models are run until the changes in the fractional coverages of all of the reaction intermediates between successive iterations are less than 10^{-12} ML (10^8 s for terrace sites and 10^{10} s for perimeter sites). The degree of rate control (DRC) is calculated using the MKMCXX software[55;53], which follows the method of Campbell and coworkers[24].

4.2.3   Possible Reaction Steps

The following elementary steps are considered in the microkinetic models:

$$CH_3OH + * \rightleftharpoons CH_3OH* \tag{4.1}$$

$$H_2O + * \rightleftharpoons H_2O* \tag{4.2}$$

$$CH_3OH* + * \rightleftharpoons CH_2OH* + H* \tag{4.3}$$

$$CH_2OH* + * \rightleftharpoons CHOH* + H* \tag{4.4}$$

$$CHOH* + * \rightleftharpoons COH* + H* \tag{4.5}$$

$$COH* + * \rightleftharpoons CO* + H* \tag{4.6}$$

$$COH* + H_2O \rightleftharpoons COH{-}H_2O* \tag{4.7}$$

$$COH{-}H_2O* + * \rightarrow CO* + H* + H_2O \tag{4.8}$$

$$CH_3OH* + * \rightleftharpoons CH_3O* + H* \tag{4.9}$$

$$CH_3O* + * \rightleftharpoons CH_2O* + H* \tag{4.10}$$

$$CH_2O* + * \rightleftharpoons CHO* + H* \tag{4.11}$$

$$CHO* + * \rightleftharpoons CO* + H* \tag{4.12}$$

$$CH_2OH* + * \rightleftharpoons CH_2O* + H* \tag{4.13}$$

$$CHOH* + * \rightleftharpoons CHO* + H* \tag{4.14}$$

$$CO* \rightleftharpoons CO + * \tag{4.15}$$

$$H* \rightleftharpoons \frac{1}{2} H_2 + * \tag{4.16}$$
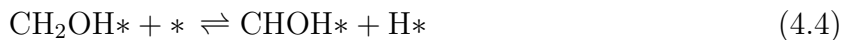
where "$*$" is an adsorption site and "$*$'ed" species are adsorbed to the catalyst. Structures of adsorbed species can be found in Supporting Information[37] Section 3. Steps 4.1-4.16 are chosen based on prior work by López[59], Mavrikakis[101], Neurock[45], Asthagiri[145], Janik[97], Zhou and Li[225], and our group[18,211]. Of the steps listed, those involving H_2O (e.g., rxn 4.2) are not included in gas phase microkinetic models. Further, H_2O adsorption is not included in the aqueous phase terrace site model because the binding energy of H_2O is significantly weaker than for CH_3OH on Pt(111)[167,155]. Finally, H_2O-catalyzed COH$*$ dehydrogenation (rxns 4.7 and 4.8) is not included in the aqueous phase perimeter site model, since by inspection (see Supporting Information[37] Figure 10g) the O−H bond on COH$*$ in perimeter sites is inaccessible to H_2O. (We additionally show below that COH$*$ does not form on perimeter sites, so the reaction is irrelevant anyways.)

In addition to steps 4.1-4.16, we investigate reactions where H_2O* donates a proton to a partially dehydrogenated species and converts to OH$*$ (e.g., $CH_2O* + H_2O* \rightleftharpoons CH_2OH* +$ OH$*$; see Supporting Information[37] Section 1.3). We find that this type of reaction is unfavorable at terrace sites; however, some such reactions are feasible at perimeter sites. Effects of these steps on the mechanism and rate are discussed below and in Supporting Information[37] Section 1.3.

C−O cleavage and hydrogenolysis reactions are not included in our models since they are thermodynamically[113] and kinetically unfavorable,[68,45] respectively. The Boudard reaction[56] ($2CO* \longrightarrow CO_2* + C*$) is not included since activity is suppressed below 673 K[109] (while APR is carried out ∼500 K). Finally, any step 4.1-4.16 with calculated free energy (see Table 4.1) more positive than 0.30 eV is not included in microkinetic modeling.

4.2.4 Rate Constants

Rate constants for surface reactions are calculated using the equations:

$$k_{\text{fw}} = A_{\text{fw}} \exp\left(\frac{-\Delta F_{\text{act,fw}}}{k_B \cdot T}\right) \tag{4.17}$$

$$k_{\text{bw}} = k_{\text{fw}}/K_{\text{eq}} \tag{4.18}$$

$$K_{\text{eq}} = \exp\left(\frac{-\Delta F_{\text{rxn}}}{k_B \cdot T}\right) \tag{4.19}$$

where "fw" denotes the forward reaction, "bw" denotes the backward reaction, A is the pre-exponential term, F is the calculated free energy, k_B is Boltzmann's constant, and T is the reaction temperature. A_{fw} and A_{bw} are set equal to 10^{13} s^{-1} · site^{-1} for all reactions[187] except the forward reaction of step 4.7 and the backward reaction of step 4.8, which both involve a liquid H_2O molecule. Values of A for these reactions are set as follows. $A_{\text{fw,7}}$ is set equal to 1.43×10^{10} s^{-1} · site^{-1}, which is the value calculated in our prior work[18]. $F_{\text{act,fw,7}}$ and $F_{\text{act,fw,8}}$ are set to zero, also following our prior work[18], since step 4.7 simply involves forming a hydrogen bond between COH∗ and a liquid H_2O molecule, and step 4.8 involves proton transfer through a hydrogen bond[145;227;97]. Then, $A_{\text{bw,8}}$ is solved for to maintain thermodynamic consistency between steps 4.6, 4.7 and 4.8. Doing this, $A_{\text{bw,8}}$ equals 2.25×10^{9} s^{-1} · site^{-1}.

Rate constants for adsorption and desorption are simulated using the Hertz-Knudsen (HK) model[53], which computes A_{fw} as the number of collisions per unit time that an ideal gas molecule has with a featureless surface and assumes that $\Delta F_{\text{act,fw}} = 0$ and $\Delta F_{\text{act,bw}} = -\Delta F_{\text{ads}}$ for exergonic adsorption. We have previously shown that such models give adsorption rates for methanol that are several orders of magnitude smaller (depending on the concentration) than the adsorption rate in liquid systems and proposed an alternate method for quantifying the adsorption rate in liquid systems[222]. We found that using this alternate method does not significantly influence the results of this work (see Supporting Information[37] Section 1.8). We

hence use the HK model for all adsorption/desorption reactions for simplicity. Additionally, we neglect solvation contributions to $\Delta F_{\text{act,bw}}$ for steps 4.15 and 4.16. This is done so as not to convolute differences in the simulated CH_3OH dehydrogenation rates between gas and aqueous phases with the free energies of solvation of $CO*$ and $H*$. Specifically, we find that water solvent destabilizes $CO*$ by 0.14 eV on terrace sites and 0.26 eV on perimeter sites and $H*$ by 0.03 eV on terrace sites and 0.11 eV on perimeter sites (see Table 4.1). While the destabilization of $H*$ has minimal influence on the simulated rate of methanol dehydrogenation (see Supporting Information[37] Section 1.9), destabilization of $CO*$ increases the rate by up to 3 orders of magnitude (see Supporting Information[37] Section 1.5). FTIR experiments did not consider $CO*$ desorption or conversion by another means, such as WGS[78], so accounting for destabilization in microkinetic modeling would cloud our ability to identify the roles of water solvent observed experimentally.

4.2.5 Site Balance

Sites are counted as follows. On Pt(111), a site can be considered to be a single Pt atom (or the surface area occupied by a single Pt atom). Analysis of adsorbate geometries in perimeter sites indicates that defining a perimeter site is more complicated. This is because some species (e.g., CH_2OH*) bind to both Pt and Al, others (e.g., CH_3OH*, H_2O*) bind to Al and "block" the proximal Pt atom from most – but not all – species, and others (e.g., $H*$) only bind to Pt and do not block the proximal Al atom at all. This is important, since in the second and third cases, two species could potentially occupy the same "site," depending on how a site is defined. Based on the reaction steps presented above and the adsorbate geometries presented in Supporting Information[37] Figure 10, this could occur when 1) CH_3OH or H_2O adsorbs to an Al atom simultaneously with $H*$, and 2) H_2O adsorbs to an Al atom simultaneously with $CO*$. Accounting for this would require writing a multisite

microkinetic model where Pt and Al atoms are counted separately. To our knowledge, this capability does not exist in the MKMCXX code. Hence, we tested the two scenarios as follows. To model scenario 1), we wrote a model where H* does not exist and instead directly desorbs as $\frac{1}{2}H_2$. For example, instead of $CH_3OH* + * \rightleftharpoons CH_2OH* + H*$, rxn 4.3 was written as $CH_3OH* \rightleftharpoons CH_2OH* + \frac{1}{2}H_2$. We found this choice has no noticeable impact on the mechanism and impacts the rate by less than an order of magnitude. Further details are provided in Supporting Information[37] Section 1.2. To model scenario 2), we eliminated rxn 4.2 from the microkinetic model and instead bundled the free energy of H_2O adsorption into step 4.12. We found that this choice has no noticeable impact on the mechanism or rate. Further details are provided in Supporting Information[37] Sections 1.1. Given the lack of influence of scenarios 1) and 2) on the results, we define one perimeter site as the grouping of Pt atoms plus the proximal Al atom at the Pt/Al_2O_3 perimeter.

4.2.6 Free Energies

Species free energies (F_i) are set as follows. Free energies of gas phase species (F_i^{gas}) are set equal to the electronic energies calculated using density functional theory (DFT; i.e., the zero point energy and thermal contributions are neglected). Free energies of reaction (ΔF_{rxn}^{gas}) and activation in gas phase ($\Delta F_{act,fw}^{gas}$) are then calculated as:

$$\Delta F_{rxn \text{ or } act,fw}^{gas} = \left(\sum^{\text{products or TS}} F_i^{gas} \right) - \left(\sum^{\text{reactants}} F_i^{gas} \right) \tag{4.20}$$

This equation is written using sums since ΔF_{rxn}^{gas} can involve multiple reactant and product species (e.g., rxn 4.8 has 2 reactant species and 3 product species); however, we note that $\Delta F_{act,fw}^{gas}$ always involves only 1 TS and 1 reactant species. In general, ΔF_{rxn}^{gas} and $\Delta F_{act,fw}^{gas}$ used in this work are in good agreement with values calculated previously[59;211]; microkinetic modeling results using previously reported values on terrace sites in gas phase are provided in

Supporting Information[37] Section 1.1 for comparison. Free energies of reaction and activation in the aqueous (aq) phase are computed by adding the change in the free energy of solvation, $\Delta\Delta F^{\text{solv}}_{\text{rxn or act,fw}}$

$$\Delta F^{\text{aq}}_{\text{rxn or act,fw}} = \Delta F^{\text{gas}}_{\text{rxn or act,fw}} + \Delta\Delta F^{\text{solv}}_{\text{rxn or act,fw}} \qquad (4.21)$$

where

$$\Delta\Delta F^{\text{solv}}_{\text{rxn or act,fw}} = \left(\sum^{\text{products or TS}} \Delta F^{\text{solv}}_{\text{i}} \right) - \left(\sum^{\text{reactants}} \Delta F^{\text{solv}}_{\text{i}} \right) \qquad (4.22)$$

and $\Delta F^{\text{solv}}_{\text{i}}$ are the calculated free energies of solvation for the different reaction intermediates and TSs. Exceptions are steps 4.7 and 4.8; $\Delta F^{\text{solv}}_{\text{rxn}}$ for these reactions are estimated as discussed above.

4.2.7 Solvation Thermodynamics

$\Delta F^{\text{solv}}_{\text{i}}$ for reaction intermediates are taken from Chapter 3. The estimated values of $\Delta H^{\text{solv}}_{\text{i}}$ and $T\Delta S^{\text{solv}}_{\text{i}}$ are at 300 K. The values of $T\Delta S^{\text{solv}}_{\text{i}}$ are scaled to 500 K, a typical reaction temperature for the APR, by multiplying this quantity of a factor of 5/3. Solvation thermodynamics for transition states (TSs) are estimated according to a method proposed in the Supporting Information of Ref[25]. Briefly, we found that values of $\Delta F^{\text{solv}}_{i}$ are linearly correlated to the DFT-calculated partial charges on the oxygen atoms in the alkoxy groups of aldehyde species and the oxygen and hydrogen atoms in the hydroxyl groups of alcohol species. We hence compute the partial charges of TS species using DFT and use them along with the correlation derived in prior work to determine $\Delta F^{\text{solv}}_{i}$ for TSs. Further details are provided in Supporting Information[37] Section 2. Finally, ΔF^{solv} for a free site $*$ is set to 0 for all reactions.

Structural Models

Structures needed to compute ΔF_i^{solv} for all TSs used in this work as well as ΔF_i^{gas} for the TSs for steps 4.3 and 4.13 on perimeter sites need to be calculated. These structures are calculated using periodic boundary condition DFT calculations using a 4-layer 4 Pt×4 Pt Pt(111) slab as a model for terrace sites and a Pt cluster anchored to an α-Al$_2$O$_3$(0001) slab as a model for perimeter sites, following our prior work[18;2;25]. Pt(111) slabs are modeled in supercells with lengths of a = b = 11.2 Å and c = 26.8 Å and angles of $\alpha = \beta = 90°$ and γ = 120°. Pt/Al$_2$O$_3$ perimeter sites are in supercells with lengths of a = b = 10.3 Å and c = 32.7 Å and angles of $\alpha = \beta = 90°$ and $\gamma = 55.3°$. These models are depicted in Supporting Information[37] Figures S14 and S15.

Pt particles used in our perimeter site models comprise 4 Pt atoms. We have previously shown that ΔF_i^{solv} is insensitive to the size of the Pt cluster used to model the Pt/Al$_2$O$_3$ perimeter site.[25] Specifically, we found the difference in ΔF_i^{solv} between the Pt$_4$ cluster and a Pt$_{48}$ cluster is below 0.10 eV, which is within the standard uncertainty of the modeling method used to compute ΔF_i^{solv}[25]. However, the Pt cluster size could influence calculated values of F_i^{gas}. Previous literature[146;216] showed that binding energies and reaction energetics involved in the oxygen reduction reaction calculated using Pt$_4$ clusters supported on graphene and Al$_2$O$_3$ are only minorly different when compared with 6–10 Pt atom clusters. Further, the binding energy of CO∗ on our Pt$_4$/Al$_2$O$_3$ model is only 0.08 eV more negative than the value calculated by Koleva et al.[104] using a Pt$_{10}$/γ-Al$_2$O$_3$ model. We find that the binding energy of CO∗ is 0.24 eV more negative on Pt$_4$/Al$_2$O$_3$ than on Pt(111). Since CO∗ desorption has the highest DRC (see Table 4.2), the result of this is that the simulated rate in gas phase is ∼2.5 orders of magnitude slower on our perimeter site models than on our terrace site models. However, this difference does not influence the main conclusion about perimeter sites made in this paper, i.e., that the active sites for aqueous phase CH$_3$OH

dehydrogenation are on the Pt terraces and that sites at the Pt/Al_2O_3 perimeter are inactive due to H_2O* molecules that bind strongly to Al atoms at the Pt/Al_2O_3 perimeter, hence blocking sites for CH_3OH*. These findings are discussed in detail below.

4.2.8   Kinetics from experimental data

The FTIR data is performed by our experimental collaborators and taken from a previous publication[78]. Experiments were performed on a Pt/γ-Al_2O_3 catalyst in the presence and absence of H_2O. Experiments done in the absence of H_2O were performed under vacuum at $150°C$ and 0.5 mbar methanol. Experiments performed in the presence of H_2O exposed the catalyst to 0.5 mbar H_2O prior to exposure to methanol. Both experiments were carried out for up to 30 min and the CO stretching frequency was tracked. The integral of this frequency is proportional to the quantity of methanol consumed. Experimental reaction rates are hence calculated as the rate of change of the CO integral with respect to the reaction time. Rates reported herein are the maximum values for each dataset.

4.3   Results

4.3.1   Reaction Energetics

Calculated values of ΔF_{rxn} and $\Delta F_{act,fw}$ are presented in Table 4.1. In agreement with prior work,[211] CH_3OH adsorbs more favorably at perimeter sites than terrace sites due to the presence of Lewis acidic sites at the Al_2O_3 interface[22;77;207]. Further, early $O-H$ cleavage is preferred on perimeter sites, whereas early $C-H$ cleavage is preferred on Pt terraces[45;59]. $CO*$ binds strongly to both types of sites; however, its binding energy is more than 0.3 eV stronger in perimeter sites than in terrace sites. This is in agreement with previous experimental results as well[10;102]. Notably, CH_3OH* and $CO*$ are weakened under solvation in both types of sites, with CH_3OH* destabilized by 0.14 eV in terrace sites and

46

0.13 eV in perimeter sites, and CO∗ destabilized by 0.14 eV in terrace sites and 0.26 eV in perimeter sites.

Table 4.1: Calculated free energies of reaction and activation for possible steps in the methanol dehydrogenation reaction on terrace and perimeter sites in units of eV.

Type of site		Terrace Sites				Perimeter Sites			
No.	Reaction	$\Delta F_{\rm rxn}^{\rm gas}$ (eV)*	$\Delta F_{\rm act}^{\rm gas}$ (eV)	$\Delta F_{\rm rxn}^{\rm aq}$ (eV)	$\Delta F_{\rm act}^{\rm aq}$ (eV)	$\Delta F_{\rm rxn}^{\rm gas}$ (eV)*	$\Delta F_{\rm act}^{\rm gas}$ (eV)	$\Delta F_{\rm rxn}^{\rm aq}$ (eV)*	$F_{\rm act}^{\rm aq}$ (eV)**
1	$CH_3OH + * \rightleftharpoons CH_3OH*$	-0.76	NC	-0.62*	NC	-1.15	NC	-1.02	NC
2	$H_2O + * \rightleftharpoons H_2O*$	-0.47	NC	0.77*	NC	-0.95	NC	-0.92 / -1.16°	NC
3	$CH_3OH* + * \rightleftharpoons CH_2OH* + H*$	-0.48	0.81§	-0.77*	0.79**	-0.61	0.47	-0.43	0.56
4	$CH_2OH* + * \rightleftharpoons CHOH* + H*$	-0.51	0.49	-0.14*	0.73**	0.49	NC	0.47	NC
5	$CHOH* + * \rightleftharpoons COH* + H*$	-0.84	0.51	-1.10*	0.41**	-0.59	NA	-0.17	NA
6	$COH* + * \rightleftharpoons CO* + H*$	-0.38	1.23§	-0.08*	1.39**	-1.21	NA	-1.20	NA
7	$COH* + H_2O \rightleftharpoons COH-H_2O*$	NC	NC	0.28‡	0‡	NA	NA	NA	NA
8	$COH-H_2O* + * \rightarrow CO* + H* + H_2O$	NC	NC	-0.36‡	0‡	NA	NA	NA	NA
9	$CH_3OH* + * \rightleftharpoons CH_3O* + H*$	0.33	NC	0.44*	NC	-0.51	0.30†	-0.18	0.40
10	$CH_3O* + * \rightleftharpoons CH_2O* + H*$	-0.04	NA	-0.03*	NA	-0.40	1.00†	-0.26	0.92
11	$CH_2O* + * \rightleftharpoons CHO* + H*$	-1.33	NA	-1.42*	NA	-0.45	0.84†	-0.42	0.72
12	$CHO* + * \rightleftharpoons CO* + H*$	-1.17	0.43§	-1.07*	0.43**	-0.56	1.32†	-0.48	1.24
13	$CH_2OH* + * \rightleftharpoons CH_2O* + H*$	0.77	NC	1.18*	NC	-0.31	1.05	-0.01	1.12
14	$CHOH* + * \rightleftharpoons CHO* + H*$	-0.05	0.54	-0.10*	0.45**	-1.25	NA	-1.05	NA
15	$CO* \rightleftharpoons CO + *$	2.19	NC	2.05$^{\star,\diamond}$	NC	2.43	NC	2.17$^\diamond$	NC
16	$H* \rightleftharpoons \frac{1}{2}H_2 + *$	0.68	NC	0.65$^{\star,\diamond}$	NC	0.64	NC	0.53$^\diamond$	NC

*Taken from Ref.[25]

**Computed based on a correlation from Ref.[25]

†Taken from Ref.[211]

‡Estimated based on values reported in Ref.[18]

§Taken from Ref.[59].

NC = Not calculated because $\Delta F_{\rm rxn} \geq 0.30$ eV or it is an adsorption/desorption step and $\Delta F_{\rm act}$ is assumed to be 0 or because the reaction is not relevant in this phase.

NA = Not accessible due to a reactant species being unfavorable.

$^\diamond$ Not used in microkinetic modeling; the gas phase equivalent was used instead.

$^\circ$Equivalent value at the clean alumina surface.

The influence of solvation on the calculated reaction energetics is illustrated in Figure 4.2. This box-and-whisker plot shows the distribution of $\Delta\Delta F^{\text{solv}}$ for the reaction and activation free energies in terrace and perimeter sites. The line inside of each box is the median value of $\Delta\Delta F^{\text{solv}}$. Most of these are $\sim$0 with the exception of $\Delta F_{\text{rxn}}^{\text{aq}}$ in perimeter sites, which has a median $\Delta\Delta F^{\text{solv}}$ of 0.16 eV, indicating that $\Delta F_{\text{rxn}}^{\text{aq}}$ in perimeter sites tends to be penalized by solvation. We showed in prior work that this is the result of the large entropic penalties that result in forming CH_3O* and CH_2O*, due to the large cavities these adsorbates create in the strongly bound H_2O layer on the Al_2O_3 surface.[25] The range of values in between the tick marks (i.e., the "whiskers") indicates the range of values of $\Delta\Delta F^{\text{solv}}$ for each dataset, while the ranges of values spanned by the boxes indicate the interquartile ranges. All datasets have ranges $\sim$0.3 eV and interquartile ranges of $\sim$0.2 eV except for $\Delta F_{\text{rxn}}^{\text{aq}}$ in terrace sites, which has a range of nearly 0.7 eV. Specifically, rxns 4.3-4.6 have large $\Delta\Delta F^{\text{solv}}$ of -0.29 eV, $+0.37$ eV, -0.26 eV, and $+0.30$ eV, respectively. These reactions involve CH_2OH* and $COH*$ which have large ΔF^{solv} due to strong interactions with liquid water[18].
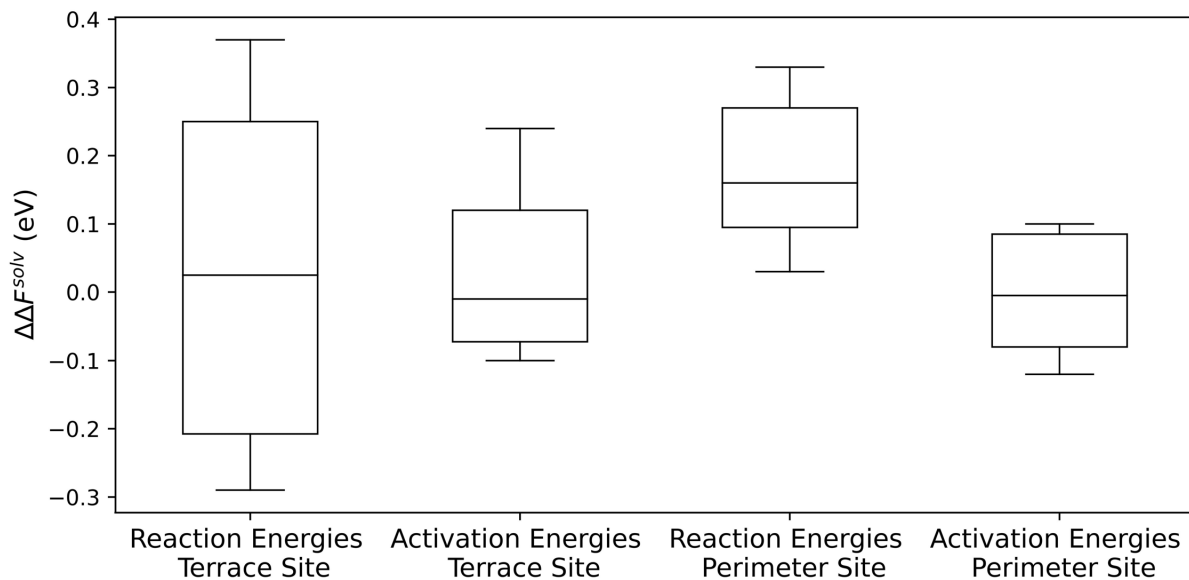
Figure 4.2: Boxplot of the solvation contribution ($\Delta\Delta F^{solv}$) due to reaction and activation for terrace and perimeter sites. The boxes show the interquartile ranges and the whiskers show the maximum and minimum observed values. The line inside the box is the median.

4.3.2 Rates and Mechanisms

Methanol consumption rates are plotted in Figure 4.3. Specifically, rates simulated in microkinetic modeling are plotted in Figure 4.3a and rates derived from FTIR data are shown in Figure 4.3b. Simulations indicate that in gas phase, the rate on terrace sites is more than 2 orders of magnitude faster than in perimeter sites. In somewhat of a contrast, the experimentally-derived rate on large Pt particles is within the same order of magnitude as that on small Pt particles. This difference could be because simulations are modeling terrace sites *or* perimeter sites, whereas the Pt particles utilized experimentally comprise both terrace sites *and* perimeter sites. Alternatively it could be due to the calculated binding energy of CO∗, or a combination, or something else altogether. For this reason, we refrain

50

from making a conclusion about the relative activity of terrace vs perimeter sites in gas phase at this time and instead focus on the influence of solvent.

Both experiments and simulations indicate that water solvent has a small influence on the rate in terrace sites (which are "modeled" by large Pt particles in experiments). However, simulations and experiments notably disagree on the influence of water on perimeter sites (which are "modeled" by small Pt particles in experiments). Specifically, simulations indicate that solvation slightly increases the rate at perimeter sites (due to slight stabilization of the TS for rxn 4.12; see below), while experiments indicate that the presence of water decreases the rate on small Pt particles by ~1.5 orders of magnitude. This difference suggests a mismatch between experiments and simulations. To understand this more deeply, we investigate the dominant reaction pathways (Figure 4.4) and rate determining steps (Table 4.2) for all four models.
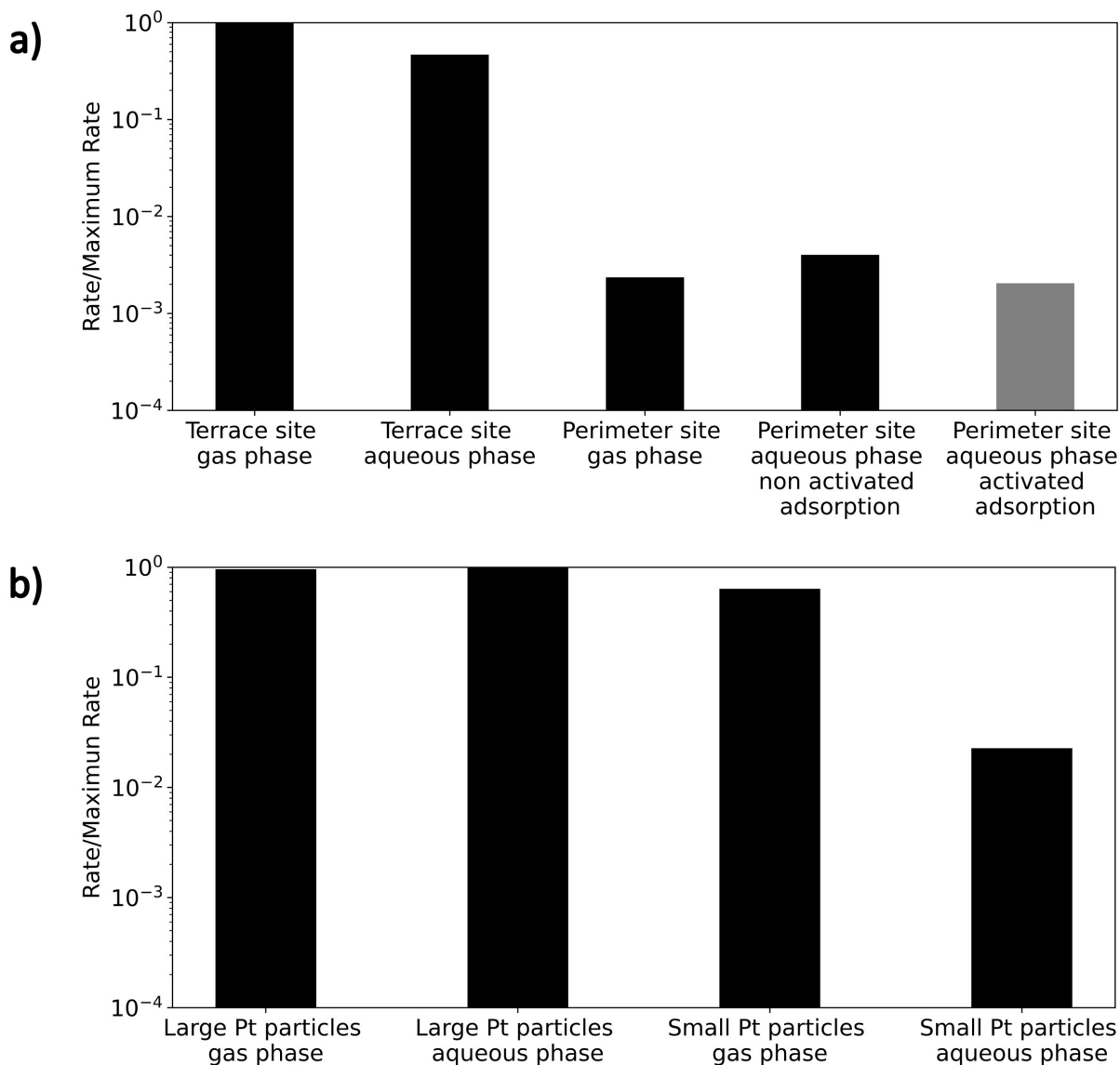
Figure 4.3: Relative methanol consumption rates. a) Rates simulated in microkinetic modeling relative to the simulated rate on terrace sites in the gas phase. Black bars represent the original model and the gray bar represents a model where methanol adsorption has an activation barrier equal to the desorption free energy of water. b) Rates derived from FTIR data[78] calculated relative to the rate on large Pt particles in the aqueous phase.
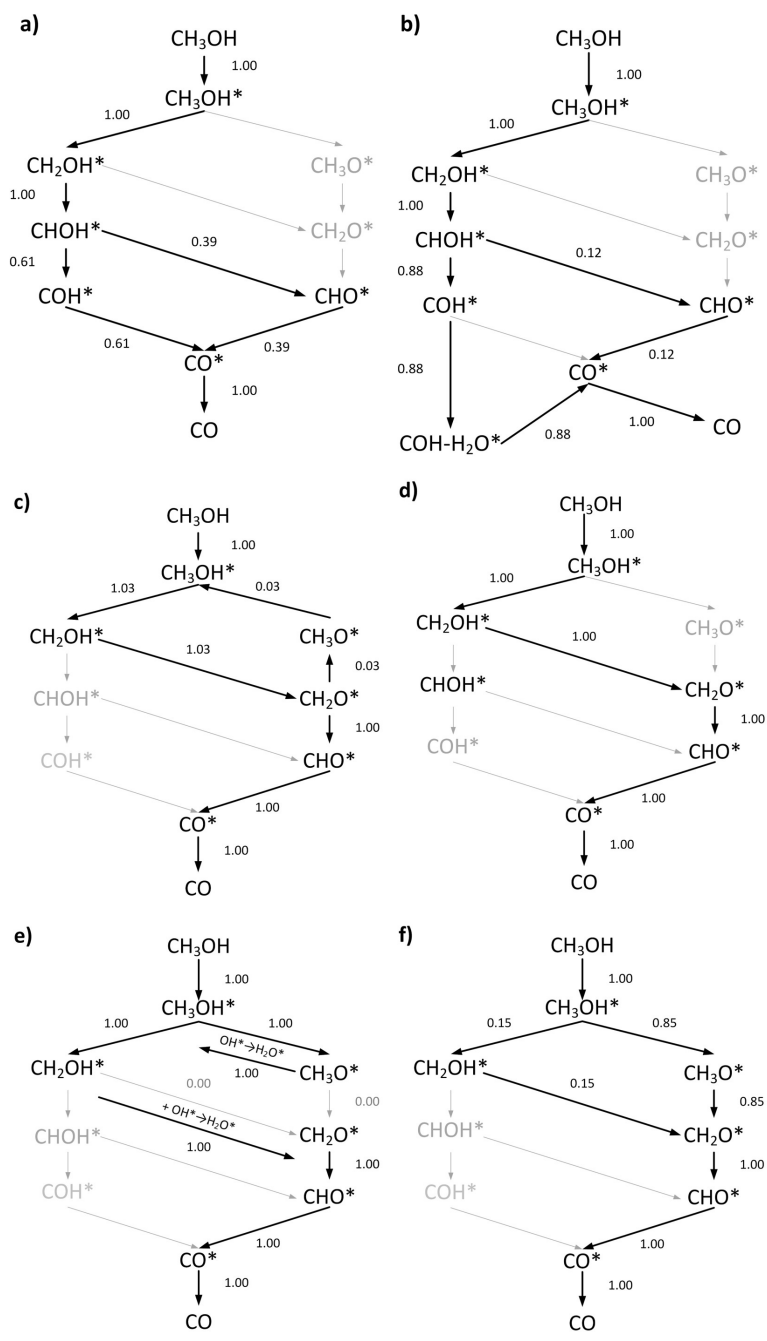
Figure 4.4: Calculated methanol dehydrogenation reaction mechanisms (black arrows) on a) terrace sites in gas phase, b) terrace sites in aqueous phase, c) perimeter sites in gas phase, d) perimeter sites in aqueous phase (original model), e) perimeter sites in aqueous phase with H_2O* reaction with CH_2O* and CH_3O* steps enabled, f) perimeter sites in aqueous phase where methanol adsorption has an activation barrier equal to the desorption free energy of water. Gray arrows represent thermodynamically and/or kinetically unfavorable reactions. Numbers over each arrow are the reaction rates relative to the rate of methanol adsorption for that model.

Table 4.2: Steps with degree of rate control value > 0.1 for the different microkinetic models investigated in this work. Values of $\Delta F_{\text{act}}^{\text{ads}}$ are for CH_3OH adsorption.

Site/phase	Step	calculated DRC value
Terrace/gas	$CO* \rightleftharpoons CO + *$	0.99
Terrace/aqueous	$CO* \rightleftharpoons CO + *$	1.00
Terrace/aqueous	$H* \rightleftharpoons \frac{1}{2}H_2 + *$	0.27
Terrace/aqueous	$CH_3OH* + * \rightleftharpoons CH_2OH* + H*$	−0.27
Perimeter/gas	$CO* \rightleftharpoons CO + *$	0.74
Perimeter/gas	$CHO* + * \rightleftharpoons CO* + H*$	0.43
Perimeter/gas	$H* \rightleftharpoons \frac{1}{2}H_2 + *$	−0.15
Perimeter/aqueous: $\Delta F_{\text{act}}^{\text{ads}} = 0$	$CO* \rightleftharpoons CO + *$	1.00
Perimeter/aqueous: $\Delta F_{\text{act}}^{\text{ads}} = 1.16$ eV	$CO* \rightleftharpoons CO + *$	0.68
Perimeter/aqueous: $\Delta F_{\text{act}}^{\text{ads}} = 1.16$ eV	$CH_3O* + * \rightleftharpoons CH_2O* + H*$	0.17

Terrace Sites

The dominant reaction pathway on terrace sites in gas phase is presented in Figure 4.4a. It begins by proceeding through an "alcohol route" where the $O-H$ bond remains intact, in agreement with previous literature[45;59;211]. Upon formation of CHOH∗, the mechanism branches to CHO∗; this is because CHOH∗ dehydrogenation to COH∗ has a large activation barrier. However, COH∗ is thermodynamically preferred over CHO∗, so 61% of CHOH∗ is converted to COH∗, while 39% of CHOH∗ is converted to CHO∗. Steps with DRC values greater than 0.1 are presented in Table 4.2. In terrace sites in gas phase, the only step that fits that criteria is CO∗ desorption with a DRC value of 0.99.

The mechanism in aqueous phase (Figure 4.4b) starts out the same as in gas phase but then becomes notably different at the CHOH∗ branch point. Specifically, the preference to form COH∗ over CHO∗ becomes stronger, with 88% of CHOH∗ going to form COH∗ and 12% of CHOH∗ going to form CHO∗, due to stabilization of COH∗ by water. Further, the steady state coverage of COH∗ is ∼ 55% COH∗ in the aqueous phase (compared to ∼ 2% in the gas phase; see Supporting Information[37] Section 1.4). Another difference

between gas and aqueous phases is that in aqueous phase, COH∗ dehydrogenation occurs via an H_2O-assisted route involving rxns 4.7 and 4.8 due to significantly more facile kinetics. Further, desorption of both CO∗ and hydrogen have DRCs greater than 0.1 in aqueous phase (Table 4.2), with values of 1.00 and 0.27, respectively. Further, $CH_3OH∗$ dehydrogenation to $CH_2OH∗$ has a DRC value of −0.27 in aqueous phase. This is due to stabilization of both $CH_2OH∗$ and COH∗ by water. Specifically, stabilization of $CH_2OH∗$ via rxn 4.3 and subsequent stabilization of COH∗ via rxn 4.5 results in the larger preference for COH∗ over CHO∗ at the branch point. However, weakening of CO∗ via rxn 4.6 results in slower CO∗ formation kinetics (and hence slower CH_3OH consumption kinetics). If rxn 4.3 were slower, the proportion of CHO∗ to COH∗ would be larger and hence formation of CO∗ would be less impacted by water. Similarly, if hydrogen desorption were faster, formation of CO∗ via rxn 4.6 would be faster. A more detailed explanation is provided in Supporting Information[37] Section 1.6.

Perimeter Sites

The dominant reaction pathway on perimeter sites in the gas phase is presented in Figure 4.4c. We find that early C–H cleavage is preferred, similar to the mechanism on terrace sites. However, $CH_2OH∗$ is then entirely converted to $CH_2O∗$. Once $CH_2O∗$ is formed, a small amount is converted to $CH_3O∗$; however, the majority is converted to CHO∗. Perimeter sites hence follow an "aldehyde" pathway following the formation of $CH_2OH∗$. A similar mechanism was found for CH_3OH dehydrogenation on Pt/CeO_2[127]. Surface coverage in this model is ∼60% CO∗ and ∼40% CHO∗. The reactions with DRC values greater than 0.1 are CO∗ desorption and CHO∗ dehydrogenation to CO∗, with DRC values of 0.74 and 0.43, due to the strong binding energy of CO∗ and large activation energy of CHO∗ dehydrogenation, respectively (see Table 4.1). Further, hydrogen desorption has a DRC value of −0.15; if this reaction were slower, it would promote the conversion of COH∗ to CO∗ + H∗.

The mechanism for perimeter sites in the aqueous phase (Figure 4.4d) is largely the same as in gas phase, with the only minor differences being that CH_2O* dehydrogenation does not run in reverse and that $CO*$ desorption is the only step with a DRC value greater than 0.1 (equal to 1.00 in this case), due to a 0.08 eV reduction in the barrier for $CHO*$ dehydrogenation. As a result, the rate in the aqueous phase is slightly larger than in gas phase. This observation is in contrast to experiments performed on small Pt particles, which showed a reduction in the rate in the presence of water (see Figure 4.3b).

Possible Explanations for Differences Between Experiments and Theory

The difference in the presence of water on small Pt particles observed experimentally vs. Pt_4/Al_2O_3 perimeter site models used in simulations suggests a "mismatch" between experiments and theory. One possibility for this could be that H_2O* molecules adsorbed at Pt/Al_2O_3 perimeter sites are protonating aldehyde intermediates[144] (e.g., $CH_2O*+H_2O* \rightleftharpoons CH_2OH* + OH*$), hence pushing the reaction backward (towards hydrogenation) and hindering the rate of methanol dehydrogenation. To investigate this possibility, we compute the free energies of such steps; they are presented in Supporting Information[37] Section 1.3. We find that reaction of H_2O* with CH_3O* to form CH_3OH* and CH_2O* to form CH_2OH* have free energies more negative than 0.3 eV (which is our tolerance for inclusion in microkinetic modeling). We hence enable these steps in microkinetic modeling, assuming the activation barriers for these steps are equal to 0, using reasoning developed in our prior work that proton transfer through a hydrogen bond has an activation barrier ~0[97;227;145;18]. Details of these simulations are presented in Supporting Information[37] Section 1.3, and the resulting mechanism is presented in Figure 4.4e. We find that H_2O* indeed participates in the mechanism by reacting with CH_3O* to form CH_3OH*; the $OH*$ that is formed then reacts with CH_2OH* to form CH_2O*. Beyond that, the mechanism is the same as in our original model. Further, the rate is unaffected (see Supporting Information[37] Section 1.3), suggesting that

H_2O* reaction with CH_xO* species at the Pt/Al_2O_3 perimeter is not responsible for the decrease in rate on small Pt particles observed experimentally.

A second possibility, which was proposed in our prior publication[78], is that diffusion of CH_3OH* across the Al_2O_3 interface is hindered by the strongly bound H_2O* adlayer[6;154] and that this affects the rate on small particles. To test this scenario, we compute the barrier of CH_3OH* diffusion across an Al_2O_3 slab in vacuum versus in the presence of a H_2O* adlayer. Details of these calculations are provided in Supporting Information[37] Section 1.7. Briefly, to simulate the aqueous phase scenario, a H_2O* adlayer is built around the TS identified in the gas phase and then the TS structure is re-relaxed. Doing this, we find that the barrier for CH_3OH* diffusion *decreases*, i.e., the H_2O* adlayer stabilizes the TS for CH_3OH* diffusion on Al_2O_3.

A failing with that model is that it does not account for the requirement that CH_3OH* must *displace* adsorbed H_2O* molecules while diffusing across the Al_2O_3 surface. To test this scenario, we increase $\Delta F_{\text{act,fw}}^{\text{aq}}$ for CH_3OH adsorption (step 4.1) from 0 to 1.16 eV, which is the free energy of desorption of a H_2O* molecule from α-Al_2O_3 in aqueous phase (note that the free energy of H_2O* desorption from pristine α-Al_2O_3 and Pt_4/Al_2O_3 are modestly different; this is due to steric hindrance on the supported Pt models). This is akin to modeling the barrier to CH_3OH* adsorbing to a perimeter site as the free energy required to displace a H_2O* molecule on the Al_2O_3 surface. Doing this, we find a $\sim$50% reduction in the rate of methanol consumption. This rate is compared with the other simulated rates in Figure 4.3a (gray bar). The mechanism is shown in Figure 4.4f. It is largely similar to the original scenario (i.e., where the activation barrier for CH_3OH adsorption was set to 0) except that a branch point occurs at CH_3OH*, with 15% of CH_3OH* being converted to CH_2OH* and 85% being converted to CH_3O*. While this scenario gives behavior that is more in line with observations from FTIR, the slight decrease in rate observed in microkinetic

modeling is noticeably less dramatic than the multiple order of magnitude decrease observed experimentally. We discuss the reasons for this in the next section.

4.4   Discussion

While the rate of methanol dehydrogenation on Pt/Al_2O_3 perimeter sites has only minor dependence on the activation barrier for methanol adsorption, the steady state *coverages* (Supporting Information[37] Figure 4) are strongly dependent on this quantity. Specifically, using the activated adsorption model, the coverage of H_2O* at the Pt/Al_2O_3 perimeter is $\sim$50% (with the remaining $\sim$50% being occupied by $CO*$), while using the unactivated model, the H_2O* coverage is $\sim$0, while the $CO*$ coverage is $\sim$100%.

The larger coverage of H_2O* suggests that reactions involving H_2O* should have more appreciable rates. We hence enabled the steps involving reaction of H_2O* with CH_3O* to form CH_3OH* and CH_2O* to form CH_2OH* along with activated methanol adsorption in our microkinetic modeling simultaneously. Doing this, the methanol consumption rate on Pt/Al_2O_3 perimeter sites decreased to $\sim$0. This decrease is more dramatic than observed in FTIR; however, we propose it is the combination of these two things that causes the decrease in rate observed experimentally. Specifically, we propose that strongly bound H_2O* molecules both inhibit CH_3OH binding at the Pt/Al_2O_3 perimeter and promote hydrogenation of CH_3OH fragments that are bound there. In fact, our microkinetic models suggest the combination of these two effects completely shuts the reaction down at the Pt/Al_2O_3 perimeter, hence suggesting that activity observed experimentally on small Pt particles is due to the Pt terraces that exist in the system. This is a difference between the simulated and experimental systems: the models of perimeter sites used in simulations *only* comprise perimeter sites, whereas the small Pt particles used in experiments *mainly but not entirely* comprise perimeter sites. Hence, the experimentally observed decrease in activity going from

4.6 nm to 1.0 nm particles is $\sim$1.5 orders of magnitude, whereas going from terrace site to perimeter site *models* results in a complete loss of activity.

Taken together, these results suggest that small Pt particles are less active than large Pt particles due to strongly bound H_2O* molecules at the Pt/Al_2O_3 perimeter that block sites for methanol dehydrogenation. The active sites for aqueous phase CH_3OH dehydrogenation on Pt/Al_2O_3 catalysts are hence Pt terrace sites, regardless of particle size; the mechanism is that presented in Figure 4.4b, and the steps with significant DRC values are $CO*$ desorption (positive DRC $\sim$1), hydrogen desorption (positive DRC $<$1), and CH_3OH* dehydrogenation to CH_2OH* (negative DRC > -1).

4.5   Conclusion

In this work, we combined multiscale modeling with microkinetic modeling and Fourier transform infrared spectroscopy to determine the mechanism for methanol dehydrogenation on supported Pt/Al_2O_3 catalysts under aqueous phase. A goal of this work was to determine if the active sites are Pt terrace or Pt/Al_2O_3 perimeter sites. Our findings indicate that sites at the Pt/Al_2O_3 perimeter are inactive due to the presence of strongly bound H_2O* molecules, which inhibit adsorption of CH_3OH and also push the reaction in the reverse by donating protons to CH_xO* species. The active sites are hence the Pt terrace sites. Water has little influence on the rate of CH_3OH dehydrogenation in terrace sites, but it has a significant impact on the mechanism. Specifically, water stabilizes CH_2OH* and $COH*$, which pushes the mechanism through a $COH-H_2O*$ intermediate. This intermediate alters the equilibrium between $COH*$ and $CO*$. Steps with significant degrees of rate control are $CO*$ desorption, hydrogen desorption, and CH_3OH* dehydrogenation to CH_2OH*. Some ways to improve the rate of methanol dehydrogenation on Pt/Al_2O_3 catalysts are to destabilize $CO*$ and (to

a lesser extent) H* as well as to decrease (make more positive) the free energies of solvation of CH$_2$OH* and COH*.

Chapter 5: Estimation of the thermodynamics of the ion-ligand capture process with EF-1 from Lanmodulin for rare earth elements under aqueous conditions

5.1 Introduction

Selective separation of REEs poses a significant challenge due to their identical charges and relatively similar sizes[126]. A key aspect in the development of this separation process is the selectivity towards a specific REE ion, which is expected to be related to the structure of the ligand structure. In this line, experimental results using isothermal Titration Calorimetry by Yuan Xu et al.[212] showed that the ligand-ion capturing process for Ce (+3) is endothermic and exergonic, hence entropically driven. This suggests that tuning the ligand conformational structure structure can affect the process entropy, which in turn will affect the separation thermodynamics. For this reason, one step toward addressing these difficulties is to understand the thermodynamic driving forces for this separation that could enable the production of more efficient ligands for this purpose.

To address this, gaining insights into the extraction process becomes crucial. In this ligand-ion capturing process, the ion that is initially fully hydrated; partially loses its solvation structure to be bound to the Lanmodulin ligand, and at the same time, the ligand undergoes a structural reorganization after binding to the ion and a reduced solvent interaction. This process can be described as the reaction shown in Equation 5.1.

$$\text{Ligand}_{aq} + \text{Ion}_{aq} \rightleftharpoons \text{Ligand} \cdot \text{Ion}_{aq} \qquad (5.1)$$

Lanthanide ions in aqueous solution usually exhibit a +3 charge with 8-9 water molecules in the first solvation shell[219]. The water structure in the first solvation shell follows a regular tricapped trigonal prism structure (see Figure 5.1 a)) for lighter lanthanides with 9 water molecules and for heavy lanthanides a square antiprism structure with 8 water molecules[153;219] (see Figure 5.1 b)). These solvation shells in water are very strongly bound with reduced mobility, especially for the first solvation shell and to a lesser extent in the second solvation shell[57]. On the other hand, once the ion is bound to the ligand, the ligand suffers a structural reorganization, specifically LanM undergoes a significant conformational change from disordered to ordered upon binding[126]. All of these structural changes are expected to have some thermodynamic implications in this process, i.e. the release of some of the first solvation shell water molecules to the bulk solution and the structural reorganization of the ligand around the ion. A step forward to understand and improve this process is to estimate the impact of all of these phenomena could have on the process thermodynamics. To begin addressing this question, it is necessary to estimate the solvation and binding process thermodynamics. To model this process, the EF-1 loop of LanM is selected as the test ligand due to its affinity for both calcium and lanthanide ions[214]. A representation of the EF-1 loop of LanM bound to Y is provided in Figure 5.2.
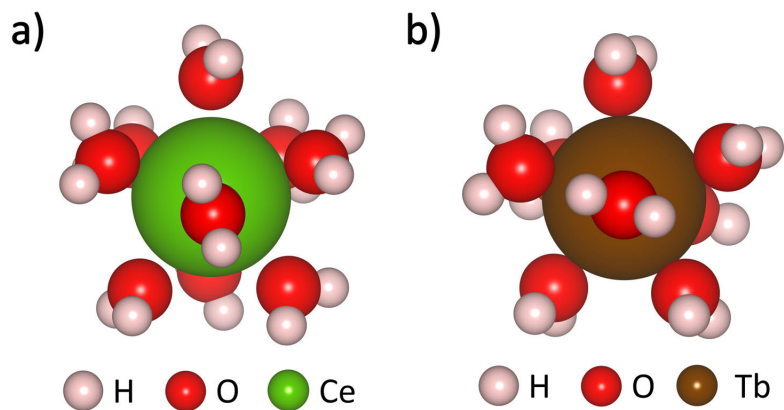
Figure 5.1: First solvation shells of ion in the unbound state optimized with DFT. a) Ce (+3) with 9 water molecules b) Tb (+3) with 8 water molecules.
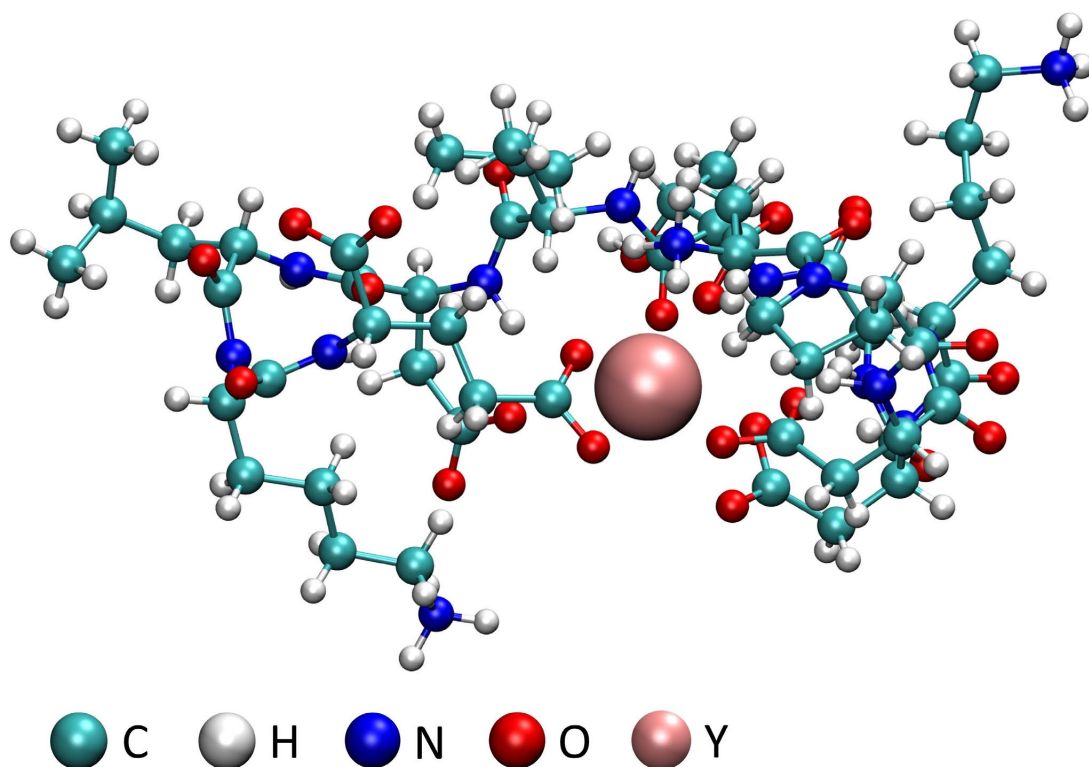
Figure 5.2: Graphical representation of EF-1 loop from LanM bound to Y. The structure is taken from Ref[32].

5.2   Methods

5.2.1   Process thermodynamics

The ion capture process $(\text{Ligand}_{\text{aq}} + \text{Ion}_{\text{aq}} \rightleftharpoons \text{Ligand} \cdot \text{Ion}_{\text{aq}})$ involves the partial loss of the solvation shells of the ion in the aqueous phase and the structural reorganization of the ligand to accommodate the ion. To estimate the ion-capture thermodynamics, the following thermodynamic process is proposed:

$$\text{Ion}_{\text{aq}} \longrightarrow \text{Ion}_{\text{vac}} \tag{5.2}$$
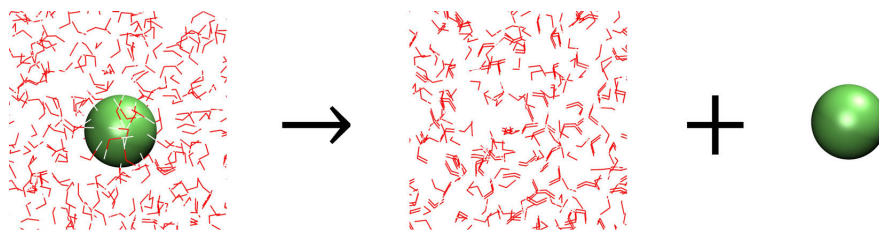
Figure 5.3:   Graphical representation of step 1 of the thermodynamic process for the ion capture process.

$$\text{Ligand} \cdot \text{Ion}_{\text{aq}} \longrightarrow \text{Ligand}_{\text{aq}} + \text{Ion}_{\text{vac}} \tag{5.3}$$
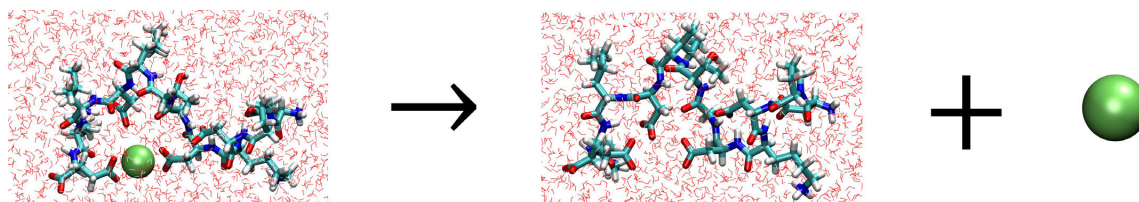
Figure 5.4:   Graphical representation of step 2 of the thermodynamic process for the ion capture process.

In the first thermodynamic step (see equation 5.2 and figure 5.3) the ion that initially is in the aqueous phase is transferred to the vacuum phase. In the second step, starting from the bound state of the ion with the ligand, the ion is transferred to the vacuum phase. Finally, to obtain the desired thermodynamic process (Ligand$_{\mathrm{aq}}$ + Ion$_{\mathrm{aq}}$ $\rightleftharpoons$ Ligand $\cdot$ Ion$_{\mathrm{aq}}$), step 2 (equation 5.3) is subtracted from step 1 (equation 5.2).

Another relevant thermodynamic quantity of interest is the ion substitution process; where the starting point is the ligand previously bound to an ion, instead of the unbound ligand. This is because in wastewater +2 ions are present and could compete with the REEs, for this reason it is necessary that the ligand exhibit a high selectivity towards the REEs and not with the +2 ions[35]. In the case of Ca (+2), a common reference in the literature[35;44], the target thermodynamic quantity is described as equation 5.4. The Ca (+2) is treated equivalent to the +3 ions previously described. The estimation of these thermodynamic quantities is performed by molecular dynamics (MD) as described in the following section.

$$\text{Ligand} \cdot \text{Ca}_{\mathrm{aq}} + \text{Ion}_{\mathrm{aq}} \rightleftharpoons \text{Ligand} \cdot \text{Ion}_{\mathrm{aq}} + \text{Ca}_{\mathrm{aq}} \qquad (5.4)$$
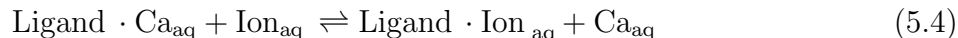
5.2.2 Simulation approach

To estimate the target thermodynamic quantities, two types of structures are necessary: the ion in the aqueous phase, and the ligand in the bound state under aqueous conditions. The first type of structure is obtained by direct insertion of the ion into the solvent and an equilibration run at the working temperature. However, the structures of the ligand are more difficult to obtain. This difficulty arises from the large protein configuration space, which, in turn, requires significant computational resources to obtain a properly equilibrated structure[39;111]. Taking this into account, this research starts from a previously obtained

structure (PDB: 6MI5) by nuclear magnetic resonance of the LanM bound to Y (+3) by A. Cotruvo et al[32]. A graphical representation of this structure is provided in Figure 5.2. From this LanM structure, the EF-1 loop peptide structure was obtained by selecting residues 35-46. This EF-1 loop is the ligand used in the simulations. To estimate the equilibrium structure of the other ions, the structure with the Y (+3) bound by A. Cotruvo is used as an initial guess, replacing the Y (+3) ion with the desired ion. After this, an equilibration at the working temperature is performed. To generate the LanM structure in the unbound state, a long equilibration run from the LanM in the bound state without the ion is proposed (simulation details are provided in the following section). To verify a proper equilibration in the unbound state, the radius of gyration is estimated and used as the convergence criterion.

5.2.3   Computation of thermodynamic properties

The estimation of the thermodynamic properties is based on the scheme of Section 5.2.1. This consists of two types processes, one for the system with the ion under aqueous conditions (see Equation 5.2) and the other for the ion with the ligand under aqueous conditions (see Equation 5.3). The MD simulation details are presented in Section 2.2.2. The process for estimating the thermodynamic properties of the ion under aqueous conditions system is shown in Figure 5.5, and the process for the thermodynamic estimates for the system of the ion under aqueous conditions system is shown in Figure 5.6.
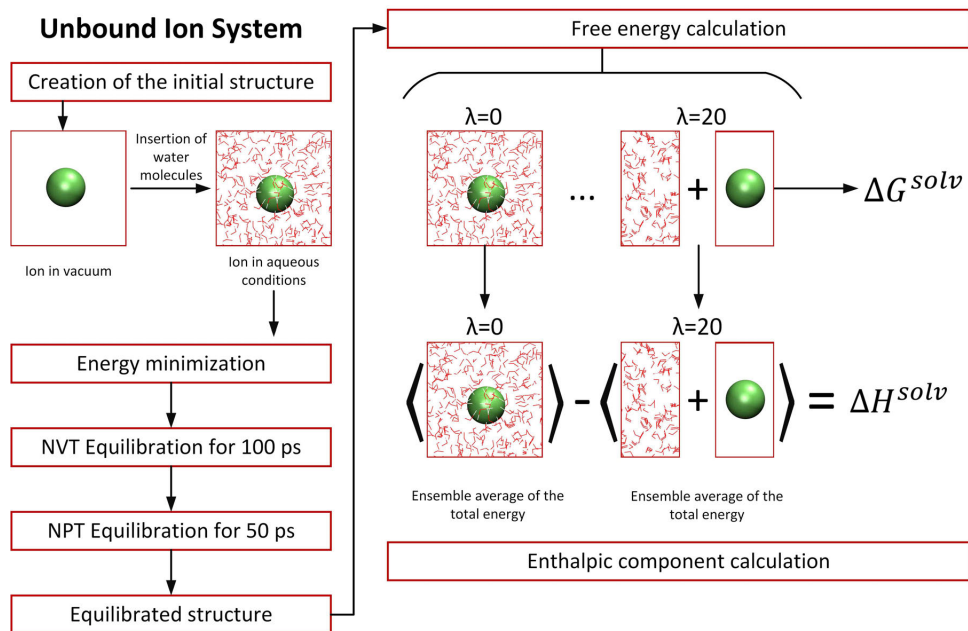
Figure 5.5: Flow diagram for the estimation of the thermodynamic properties of the ion under aqueous conditions system.
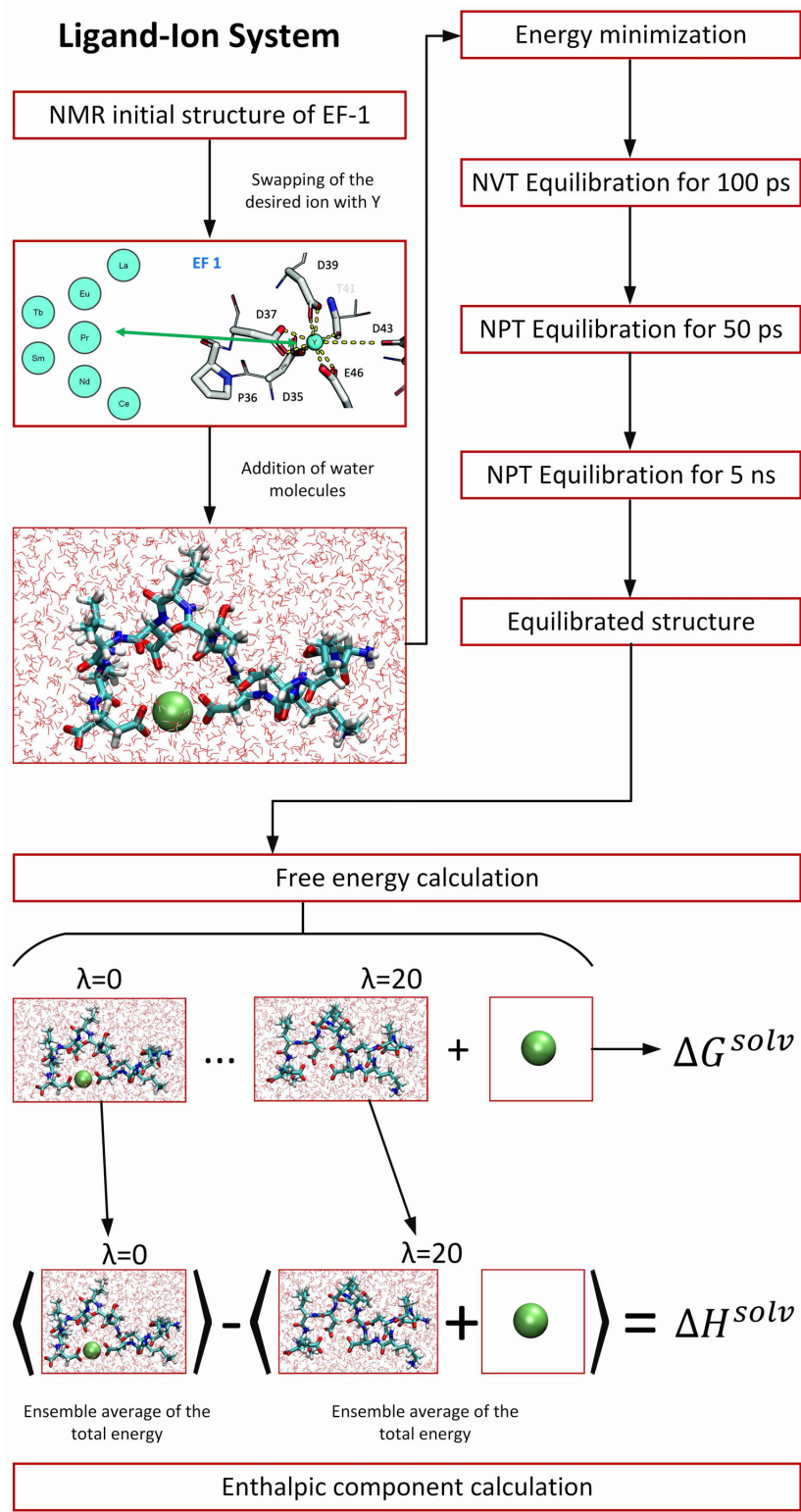
Figure 5.6: Flow diagram for the estimation of the thermodynamic properties of the ion with the ligand under aqueous conditions system.

5.2.4   Computation of structural descriptors

Besides the thermodynamic estimation, some structural features were estimated to provide some structural insights into the different systems. These include the radius of gyration, the self diffusion coefficient, and the radial distribution functions. The radius of gyration of the ligand was estimated using the default function provided by GROMACS to a centered trajectory (to avoid the ligand crossing a box boundary) over an NPT run for 20 ns, extracting a configuration every 100 ps. The self diffusion coefficient was estimated with the default GROMACS function, based on a linear regression on the mean square displacement (MSD) of atoms from a set of initial positions. This estimation was performed over an NPT run for 20 ns, extracting a configuration every 100 ps. The radial distribution function (g(r)) was estimated from a centered trajectory (to avoid the ligand crossing a box boundary) over an NPT run for 20 ns, extracting a configuration every 100 ps and a spacing between bins of 0.05Å. The number distribution (n(r)) is estimated based on the average count of atoms within a given radius and follows the same sampling of the g(r).

5.3   Results

Figure 5.7 and Table 5.1 show the solvation thermodynamics of the Ligand-ion capture process as described in Section 5.2.1, Equation 5.1 versus the effective effective ionic radius[185]. The thermodynamics steps for the calculation of 5.1 are provided in Table 5.2 and Table 5.3; following steps 5.2 and 5.3, respectively. The ion-capture process serves as an indicator of the affinity between the ligand and a specific ion. In other words, more favorable free energies correspond to a higher affinity between the ligand and the ion. A correlation between the ion-capture free energy (ΔG) and the entropic component ($T\Delta S$) with the ionic radius is observed; with more negative free energies at the smaller ionic radius. For all the

selected ions the ion-capture process is exergonic. It was also observed that the enthalpic-type contribution (ΔH) to the process thermodynamics had a minor effect on the free energy compared with the entropic effect. Consistent with experiments on a similar system[212], it is the entropic effect that drives the ligand-ion capture process for the EF-1 loop of calmodulin.

Ion	Effective effective ionic radius (Å) [†]	ΔG (kJ/mol)	ΔH (kJ/mol)	TΔS (kJ/mol)
Y	1.215	-234.46 +/- 3.40	23.00 +/- 15.58	257.46 +/- 15.95
Tb	1.235	-211.33 +/- 4.78	-3.00 +/- 11.93	208.33 +/- 12.85
Eu	1.260	-232.67 +/- 6.86	28.00 +/- 17.38	260.67 +/- 18.68
Sm	1.272	-187.35 +/- 7.44	32.00 +/- 19.87	219.35 +/- 21.22
Nd	1.303	-222.21 +/- 5.51	12.00 +/- 9.22	234.21 +/- 10.74
Pr	1.319	-186.83 +/- 4.42	29.00 +/- 16.57	215.83 +/- 17.15
Ce	1.336	-176.87 +/- 1.88	-11.00 +/- 24.35	165.87 +/- 24.43
La	1.356	-171.35 +/- 7.56	32.00 +/- 18.40	203.35 +/- 19.90

Table 5.1: Ligand-ion capture thermodynamics as defined in Equation 5.1. [†] Values of the effective effective ionic radius taken from Ref[185]. The errors shown are the standard errors directly printed from GROMACS. Note: these quantities are calculated from the quantities in Table5.3 and Table5.2

Ion	Effective effective ionic radius (Å) [†]	ΔG (kJ/mol)	ΔH (kJ/mol)	TΔS (kJ/mol)
Y	1.215	3268.94 +/- 0.63	3409 +/- 6.24	140.06 +/- 6.27
Tb	1.235	3210.25 +/- 0.62	3361 +/- 7.64	150.75 +/- 7.66
Eu	1.260	3163.63 +/- 0.59	3331 +/- 11.24	167.37 +/- 11.26
Sm	1.272	3123.65 +/- 0.47	3263 +/- 7.6	139.35 +/- 7.62
Nd	1.303	3073.80 +/- 0.22	3222 +/- 4.59	148.20 +/- 4.59
Pr	1.319	3034.89 +/- 0.76	3186 +/- 9.1	151.11 +/- 9.14
Ce	1.336	2983.85 +/- 0.48	3127 +/- 13.78	143.15 +/- 13.79
La	1.356	2921.10 +/- 0.89	3081 +/- 6.98	159.90 +/- 7.03

Table 5.2: Ion solvation thermodynamics as defined in Equation 5.2. [†] Values of the effective effective ionic radius taken from Ref[185]. The errors shown are the standard errors directly printed from GROMACS. Note: these quantities are directly obtained from simulations.

Ion	Effective effective ionic radius (Å) [†]	ΔG (kJ/mol)	ΔH (kJ/mol)	TΔS (kJ/mol)
Y	1.215	3503.40 +/- 3.34	3386 +/- 14.28	117.40 +/- 14.66
Tb	1.235	3421.58 +/- 4.74	3364 +/- 9.17	57.58 +/- 10.32
Eu	1.260	3396.30 +/- 6.83	3303 +/- 13.25	93.30 +/- 14.91
Sm	1.272	3311.00 +/- 7.43	3231 +/- 18.36	80.00 +/- 19.80
Nd	1.303	3296.01 +/- 5.51	3210 +/- 7.99	86.01 +/- 9.71
Pr	1.319	3221.72 +/- 4.35	3157 +/- 13.84	64.72 +/- 14.51
Ce	1.336	3160.72 +/- 1.82	3138 +/- 20.08	22.72 +/- 20.16
La	1.356	3092.45 +/- 7.51	3049 +/- 17.03	43.45 +/- 18.61

Table 5.3: Ligand-ion binding thermodynamics as defined in Equation 5.3. [†] Values of the effective effective ionic radius taken from Ref[185]. The errors shown are the standard errors directly printed from GROMACS. Note: these quantities are directly obtained from simulations.
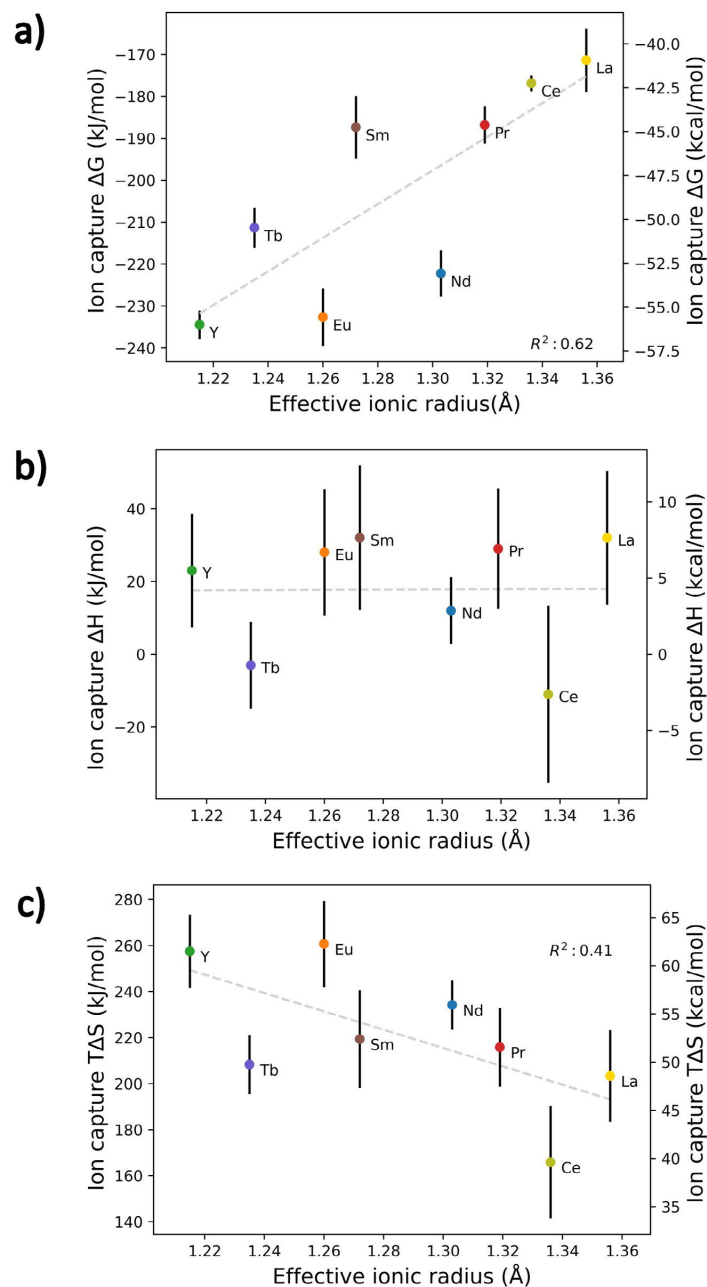
Figure 5.7: Ligand-ion capture thermodynamics for selected ions versus the effective ionic radius with error bars. a) Free energy ΔG b) Enthalpic contribution ΔH c) Entropic contribution $T\Delta S$.

Similarly, the ion substitution thermodynamics with Ca (+2) as a reference ion is presented in Figure 5.8. This process is also exergonic, but in contrast with the ligand-ion capture process, in the ion substitution process, the enthalpic component plays a larger role in combination with entropy. While the enthalpic component contributes to a baseline level around ~ 160 kJ/mol (see Figure 5.8 b)) in the free energy, the variability of the free energy with respect to the different ions is still determined by the entropic component.
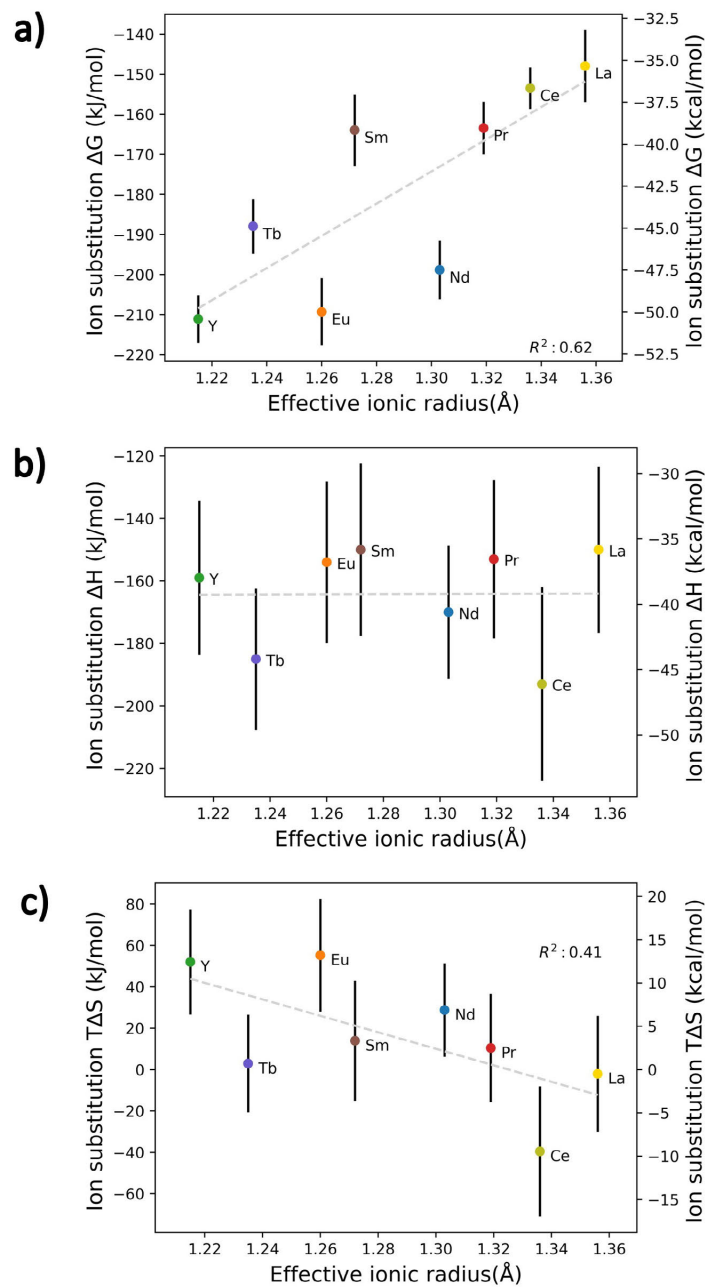
Figure 5.8: Ion-substitution thermodynamics from calcium for selected ions versus the effective ionic radius with error bars. a) Free energy ΔG b) Enthalpic contribution ΔH c) Entropic contribution TΔS.

Ion	Effective effective ionic radius (Å) [†]	ΔG (kJ/mol)	ΔH (kJ/mol)	TΔS (kJ/mol)
Y	1.215	-211.07 +/- 5.93	-159 +/- 24.72	52.07 +/- 25.42
Tb	1.235	-187.94 +/- 6.82	-185 +/- 22.6	2.94 +/- 23.61
Eu	1.260	-209.28 +/- 8.41	-154 +/- 25.9	55.28 +/- 27.23
Sm	1.272	-163.96 +/- 8.89	-150 +/- 27.63	13.96 +/- 29.02
Nd	1.303	-198.82 +/- 7.35	-170 +/- 21.29	28.82 +/- 22.53
Pr	1.319	-163.44 +/- 6.57	-153 +/- 25.36	10.44 +/- 26.19
Ce	1.336	-153.48 +/- 5.22	-193 +/- 31.01	-39.52 +/- 31.45
La	1.356	-147.96 +/- 8.99	-150 +/- 26.59	-2.04 +/- 28.07

Table 5.4: Ligand-ion substitution thermodynamics as described in Equation 5.4. [†] Values of the effective effective ionic radius taken from Ref[185]. The errors shown are the standard errors directly printed from GROMACS.

To provide some structural insights into the different systems, the following parameters were tested: the radius of gyration, the mean square displacement (MSD), and the radial distribution functions are analyzed. The radius of gyration for the ligand with the different types of ions is shown in Figure 5.9. In the set of tested ions, there were no significant variations in terms of the radius of gyration of the ligand when compared across different ion types. This indicates that the radius of gyration cannot capture the structural changes that explain the trend in the thermodynamics between the different ions.

Another important aspect to consider is the mobility of the ligand once it is bound to the ions. To investigate this, we calculated the self diffusion coefficient for the ligands with respect to the different types of bound ions. The results are depicted in Figure 5.10. No clear trend was found between this feature and the type of ions. This indicates that the ligand mobility cannot explain the thermodynamic trend between the ions.

The radial distribution functions of the different ions bound to the ligand with the oxygen of water are shown in Figure 5.11. These radial distribution functions show that the first solvation shell is below 3.5 Å, and the second solvation shell is below 5.5 Å. One relevant factor is that the three ions with the lowest effective ionic radius and more favorable binding

free energy: Y, Tb, and Eu; do not present water molecules in the first solvation shell (in the bound state with the ligand). On the other hand, Sm, which has the fourth lowest effective ionic radius, occupies an intermediate position (0-1 water molecules in the first solvation shell) between the previously mentioned ions and the ions with higher effective ionic radius: Nd, Pr, Ce, and La. These latter ions exhibit more water molecules in their first solvation shell in the range of 1-2 water molecules.
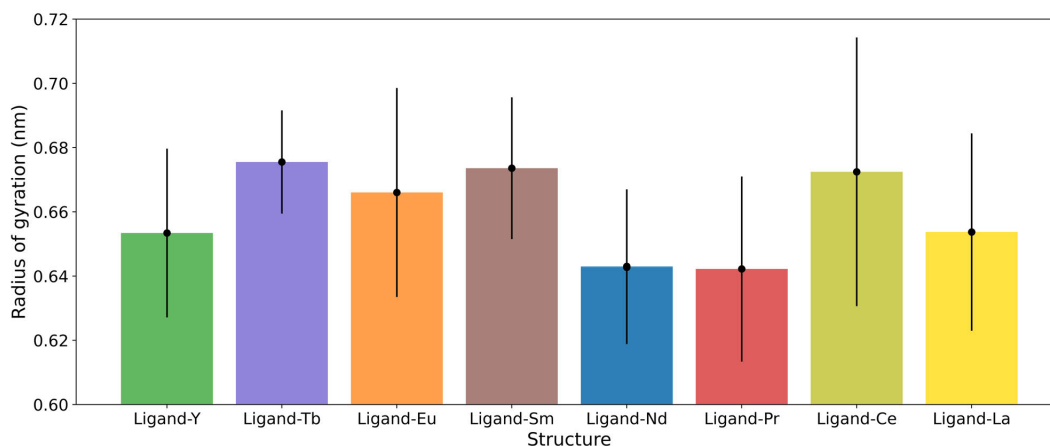
Figure 5.9: Ligand radius of gyration of the selected ions with error bars. Ions are listed in a increasing order following the effective ionic radius.
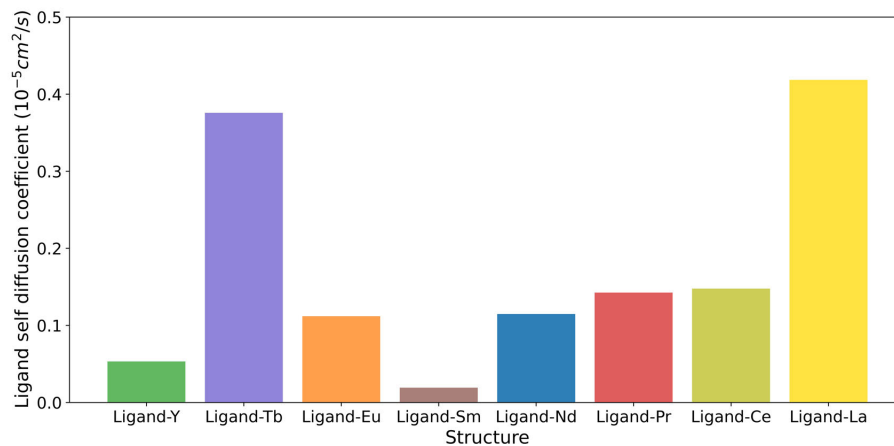
Figure 5.10: Ligand self diffusion coefficient with respect to the type of ion in the bound state. Ions are listed in a increasing order following the effective ionic radius.
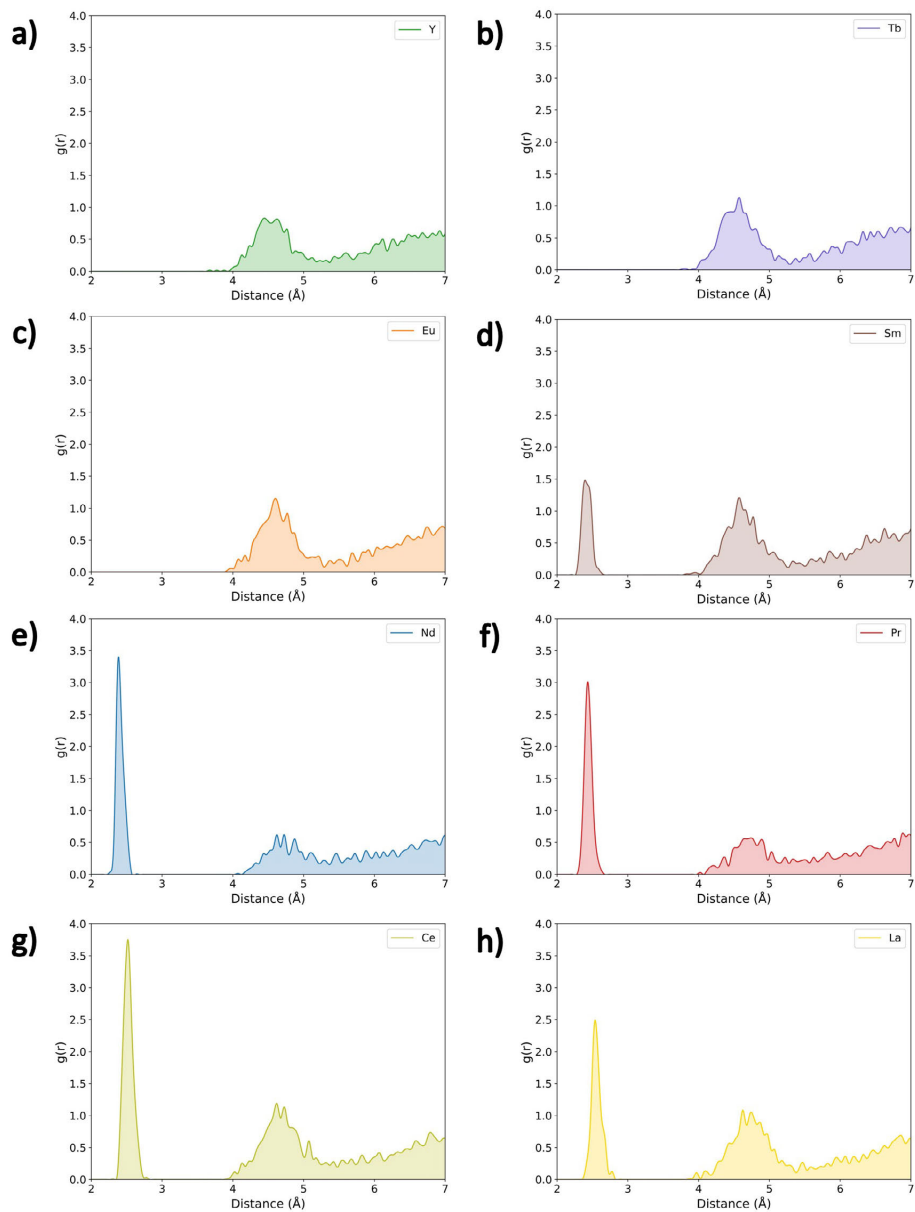
Figure 5.11: Radial distribution function between the ion in the bound state with the oxygen of water. a) Y b) Tb c) Eu d) Sm e) Nd f) Pr g) Ce h) La. Ions are listed in a increasing order following the effective ionic radius.

5.4 Discussion

5.4.1 Estimates validation

One key aspect of this study is the validation of the estimates of the process thermodynamics against experimental results. One point of comparison with experiments is the ion hydration energies which are analogous to Equation 5.2. Persson[153] reported a general correlation between the metal ion hydration energies and a factor based on the squared of the ion charge and the mean Ion–Oxygen of water bond distance as shown in Figure 5.12 a). A comparison of this correlation and our data is shown in Figure 5.12 b). Our results show fair agreement with the experimental trend, with an average difference of 360 kJ/mol less than the experimental equivalents, which accounts for a 10.03% relative difference. In terms of the average distance between the metal ion and the first coordination shell, a good agreement was obtained between the simulations and the data reported by Persson[153] (see Table 5.5). On average a difference of 0.02 Å was obtained between the experimental and simulation data.

Another point of comparison with experiments is the ligand-ion binding thermodynamics. Data generated by Verma[202] using Isothermal Titration Calorimetry (ITC) to estimate the thermodynamics of ligand-ion binding for LanM1 and with the Ce ion is provided in Table 5.6 for comparison. The experiments demonstrate an exergonic process driven by entropy, which is consistent with our simulations. However, some differences are found. The experimental thermodynamic estimates are more moderate, partially due to factors not accounted in the simulations, such as the presence of other salts and a solution buffer, among others. On the other hand, the trend between the ions is properly captured by simulations where the affinity of the ions with the ligand follows the simulation trend: Ce < Nd < Eu. Another point of comparison is the ion substitution free energy. Angelova et al.[4] using a DFT/PCM (polarizable continuum method) method estimated the ion substitution free energy between

Ca (+2) with La (+3) in -161.50 kJ/mol. This result is 9% higher than our estimate of -147.96 kJ/mol (see Table 5.8). All these results might suggest limitations from the force field or charges treatment that translate into a bias in the energetics estimation but still keep the capacity to capture the thermodynamic trends between the ions.
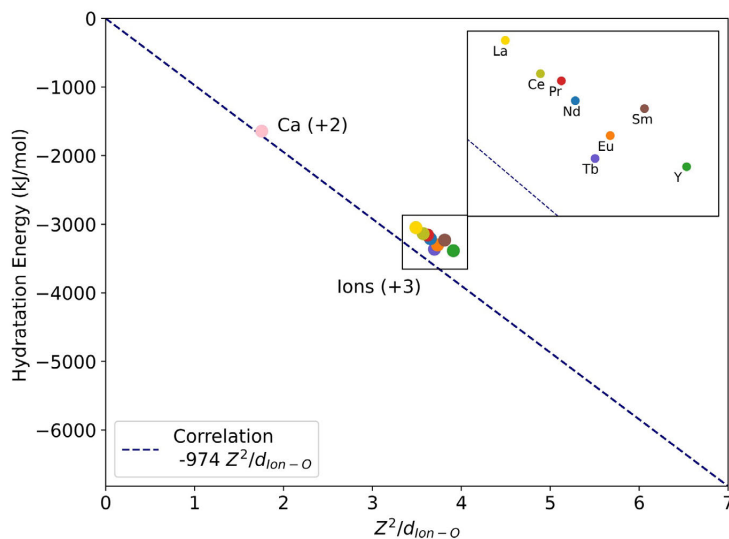
Figure 5.12: Relation between hydration energies with the ion charge and mean Ion–Oxygen of water bond distance. This plot compares the simulation results with the experimental correlation (shown with a blue dashed lines) taken from Ref[153].

Mean Ion–Oxygen of water bond distance (Å)		
Ion	Experimental data*	Simulations data
Y	2.36	2.30
Tb	2.39	2.43
Eu	2.425	2.41
Sm	2.46	2.36
Nd	2.49	2.46
Pr	2.50	2.49
Ce	2.54	2.52
La	2.52-2.64	2.58

Table 5.5: Comparison between experimental and simulations of mean Ion–Oxygen of water bond distance. *Experimental data is taken from Ref[202].

Thermodynamic quantity	ITC data*	Simulation equivalent
ΔG (kJ/mol)	-31.38 +/- 1.30	-176.87 +/- 1.88
ΔH (kJ/mol)	27.87 +/- 5.52	-11.00 +/- 24.35
TΔS (kJ/mol)	58.81 +/- 4.44	165.87 +/- 24.43

Table 5.6: Ligand ion binding thermodynamics as described in Equation 5.1. *Experimental data is taken from Ref[153].

5.4.2 Results analysis

Optimization of the ligand for selective ion capture requires the maximization of the differences between the ion binding free energies between the different types of ions. To the best of our knowledge, this process might involve three main possible driving factors for the separation: the breaking of the low mobile first solvation of the ion in solution to the bound state, the structural reorganization of the ligand, and the effect of the ligand-water interface on the structural conformation of water. The first of these possible driving forces involved in the ion capturing process is the change in the coordination environment from the ion in the aqueous solution to the bound state. For example, in the case of the Ce ion, this process

involves a reduction of the first solvation shell of the ion in solution from the unbound state to the bound state of 7.4 water molecules, as shown in Figure 5.13. A summary of the number of waters in the first and second solvation shells of the ions in the bound state is shown in Figure 5.14 a). Additionally, the number of released water molecules is shown in Figure 5.14 b). This quantity is defined as the difference between the number of water molecules in the unbound state and the number of water molecules in the bound state, within either the first or second solvation shell. Our findings (as shown in Figure 1a) align with literature[134;47], indicating that ions with smaller ionic radii tend to have fewer water molecules in their first solvation shell. For instance, when comparing the first solvation shell of smaller ions (such as Y, Tb, and Eu) to larger ions (such as Pr, Ce, and La), this trend becomes evident. However, no clear trend is observed for the second solvation shell. Regarding the total number of released water molecules, no significant differences were found between the ions, suggesting that other driving forces are responsible for explaining the binding trends. This result implies that while the release of water molecules might account for a baseline or ground level. The variability of the thermodynamics of the ligand-ion binding process is not explained by the released of water molecules as it is currently hypothesised in the literature[1]. Regarding the structural reorganization of the ligand, overall ligand characteristics such as the ligand self diffusion coefficient (see Figure 5.10) or the gyration radius (see Figure 5.9) are not able to provide insights into the different ion capture free energy trend. Another relevant feature of interest is the average distance between the oxygenate functional groups of the ligand with the ion in the bound state. The relation between these features and the ion capture thermodynamics is shown in Figure 5.15 and Figure 5.16, for the ion in the unbound and the bound state respectively. These results indicate that ions with shorter oxygen of the ligand to ion distances exhibit more favorable binding free energies and entropy. One possible interpretation of this trend is that smaller ions facilitate a greater degree of encapsulation

between the ligand and the ion; and a more encapsulated ion exhibits more affinity with the ligand. However, existing descriptors fail to fully capture the observed trend in free energies and entropic components, suggesting that additional features may play a role.
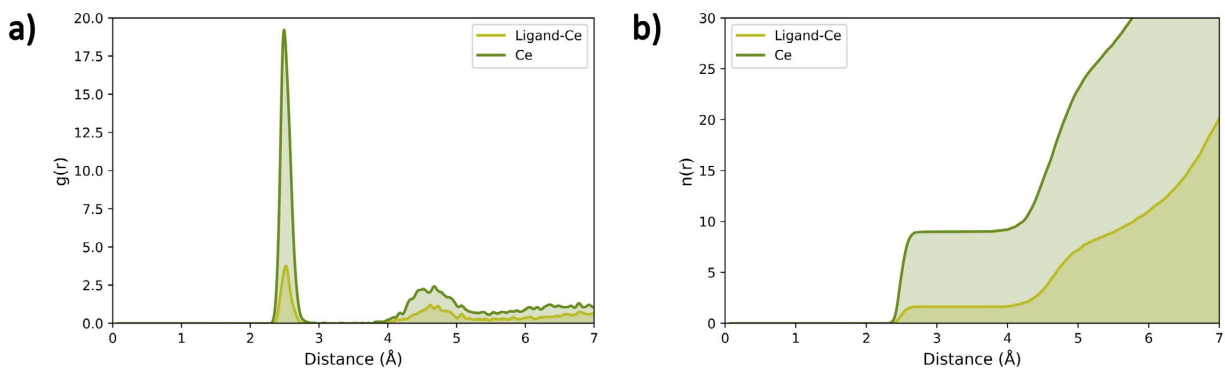
Figure 5.13:   Radial distribution function g(r) and accumulated number distribution n(r) of Ce (+3) with the Oxygen of water in the bound state (Ligand-Ce) and in the unbound state (Ce). a) g(r) b) n(r).
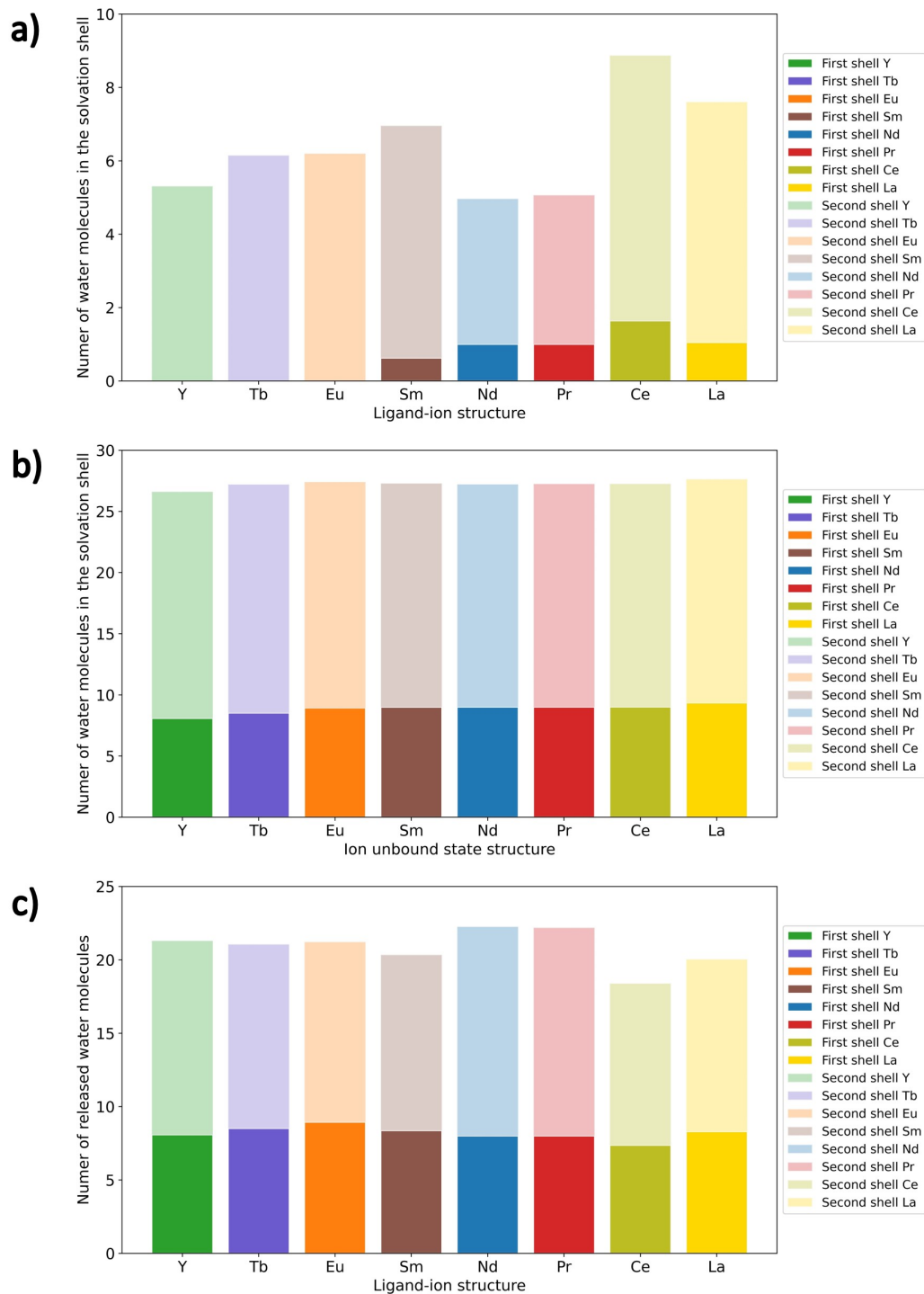
Figure 5.14: a) Number of water molecules in the first and second solvation shell per type of ion in the bound state. b) Number of water molecules in the first and second solvation shell per type of ion in the unbound state. c) Number of released water molecules in the first and second solvation shells. Ions are listed in a increasing order following the effective ionic radius. Note: The quantities calculated in c) are the subtraction of a) from b).
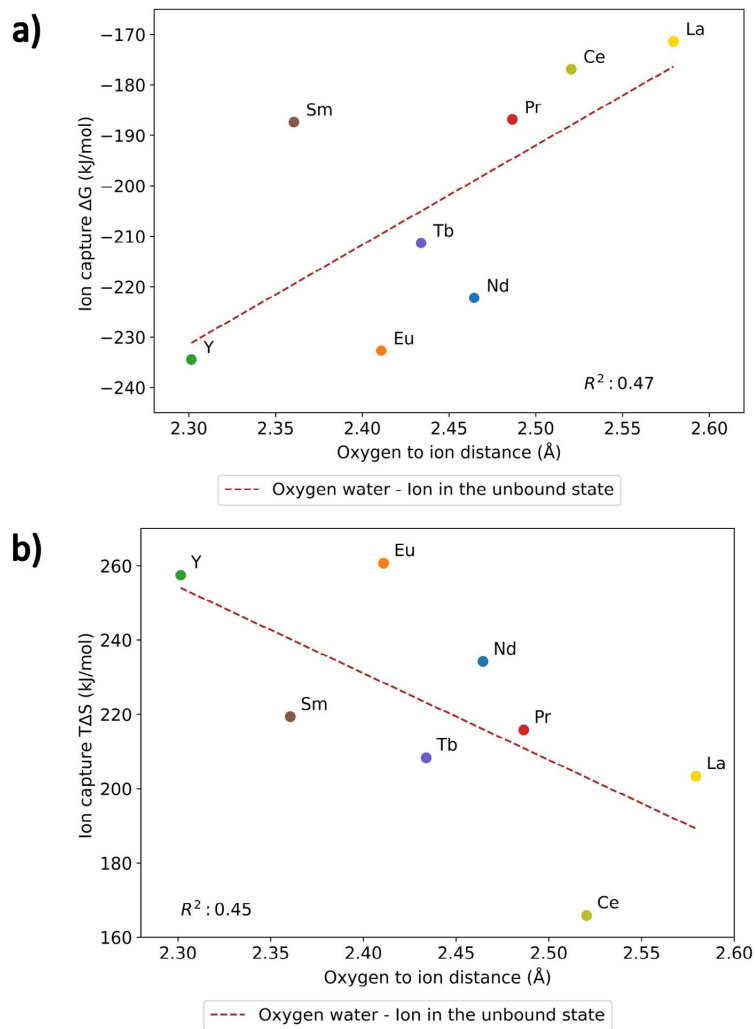
Figure 5.15: Relationship between the ion capture free energy and entropy with the average oxygen of water to the ion distance, in the unbound state. a) Free energy b) Entropy.
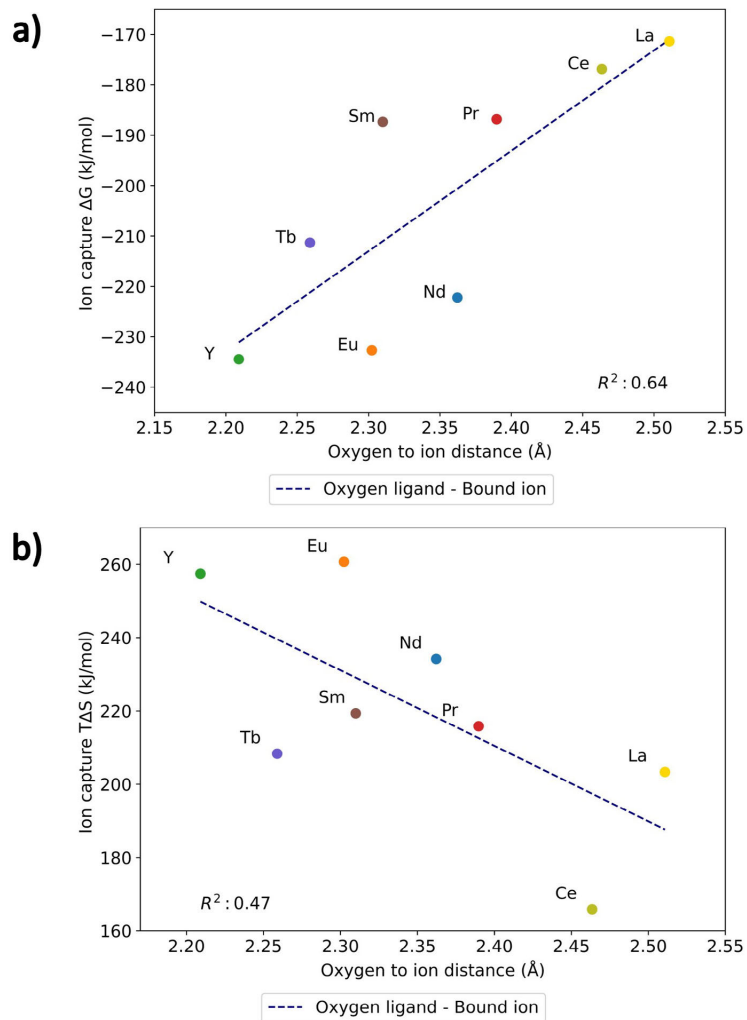
Figure 5.16: Relationship between the ion capture free energy and entropy with the average oxygen of water to the ion distance, in the bound state. a) Free energy b) Entropy.

5.5 Conclusion

The proposed strategy to estimate the thermodynamics of the ligand ion binding process of early rare earth metals is capable of replicating the affinity trend between ions with experiments[44;202], but still exhibits some difference compared to calorimetric measurements. The ligand ion binding process was found to be exergonic and entropically driven, with a low influence from the enthalpic part and consistent with experiments[212;202]. The ion

substitution process between +3 ions with Ca (+2) was also found to be exergonic, but in this case, it was mainly driven by the enthalpic component with a secondary contribution from the entropic component that explains the trend between the ions. It was observed that ions with the lowest ionic radius and closer proximity to the ligand displayed minimal or no water molecules in the initial solvation shell, and this specific group of ions also showed the highest affinity for the ligand.

Chapter 6: Conclusions and Recommendations

6.1 Summary

Understanding and estimating the thermodynamic solvent effects is a key aspect for the description and improvement of the solvent-mediated process. For this task computational techniques offer a valuable tool for the description at the molecular level of the solvent phenomena, and at the same time offer the possibility of isolating the different types of thermodynamic contributors. However, the methods have to balance accuracy, computational tractability, and enough sampling. All of these modeling decisions will depend on the environment and the target quantities, hence the methodology needs to be adapted to properly describe each system. In this dissertation, we implemented a combination of QM and MM techniques to quantify the solvent effects on applications of catalysis and ligand separation under aqueous conditions, revealing active roles of the solvent in the chemistry of these processes.

In chapter 3, we develop a modeling scheme to capture the solvation thermodynamics of the adsorbates involved in the methanol dehydrogenation on supported Pt/Al_2O_3 catalyst models. In this modeling scheme, a combination of molecular dynamics (MD) and quantum mechanics (QM) is employed to capture the entropic and enthalpic type components of the free energy, respectively. This modeling enables us to estimate the solvation thermodynamics and to make a comparison between the terrace and perimeter sites. This comparison shows

that water exhibits a different behavior at perimeter sites, compared with terrace sites due to the higher hydrophilicity of the alumina surface over the platinum surface. The higher hydrophilicity, caused the perimeter site adsorbates to be less effectively solvated compared with terrace sites. These findings highlight that the solvation thermodynamic behavior is dependable on the nature of the interface.

In chapter 4, we developed a microkinetic model to elucidate the reaction mechanism of methanol dehydrogenation in a dual-site model differentiating terrace and perimeter sites. This modeling approach tries to capture two extreme cases, one where the catalytic environment is not influenced by the support (terrace sites) and the other where the influence of the support is maximized (perimeter sites). Additionally, the solvation thermodynamics were included to capture the effect of the solvent on both types of sites. This modeling revealed that both the support and the solvent can influence the reaction mechanism. It was observed that the carbon monoxide removal is the step with the highest influence on the overall reaction rate, where the perimeter sites had a slower carbon monoxide removal, explaining the lower observed kinetics at perimeter sites. In the case of the terrace sites, the solvent affected the mechanism, but not the overall kinetics. In the case of perimeter sites the support modified the mechanism compared with terrace sites due to the presence of the alumina sites. Finally, a proposed mechanism of deactivation due to the presence of water at perimeter sites that helps explain the observed reduction of the experimental reaction rates.

In chapter 5, we devise a strategy to estimate the thermodynamics of the ion-ligand binding process for the early lanthanides with the EF-1 ligand of Lanmodulin. Our estimates showed that the binding process is exergonic and entropically driven with a higher affinity for the smaller ions. In contrast with an initial hypothesis in the literature; the release of water molecules from the ion in the unbound state to the bound state cannot explain the affinity trend between the type of ion and the ligand. This indicates that some structural

changes in the ligand are responsible for the entropic contribution that explains the different affinity between the ions.

6.2   Recommendations

This dissertation used computational techniques to estimate the solvent thermodynamic effects for applications in catalysis and separations under aqueous conditions. Although these techniques allowed the estimation of the solvent effects and at the same time provided molecular level insights into the solvent behavior, some areas of improvement were identified.

6.2.1   Multiscale sampling for free energy estimation

One of the assumptions of the perimeter site model is that the charge of the alumina slab remains roughly constant for all of the adsorbates. In our study, the size and charge of the adsorbates were small. This behavior enables us to avoid scaling the alumina surface in the thermodynamic integration. However, this condition might no longer hold for surfaces with larger charge transfer with the adsorbate or with larger adsorbates that exhibit larger net charges. The estimation of the entropic component of the solvation thermodynamics relies on the charge settings obtained from the DFT charge estimation (DDEC6 method) and the OPLS force field. These modeling decisions affect the accuracy of the estimates, but no reference values are available to validate these estimates or to compare their performance with alternative charge estimation models and alternative force fields.

6.2.2   Reaction mechanism of methanol dehydrogenation on platinum/alumina catalysts

In the microkinetic modeling aimed at elucidating the methanol dehydrogenation reaction mechanism, the carbon monoxide removal was modeled as a gas phase desorption to allow comparison with the experimental observations. This modeling decision was in line with the

scope of this research, isolating the dehydrogenation component of the mechanism. However, in the APR conditions, the WGS reaction will occur, and this in turn will affect the site coverages. For a more complete modeling of the APR process, the WGS set of reactions should be coupled into the microkinetic modeling. Hence, provinding a closer approximation to the APR process.

6.2.3 Estimation of the thermodynamics of the ion-ligand capture process

In terms of thermodynamic estimations, two main opportunities for improvement are suggested. First, we can explore enhancements related to the selected force field. Second, we can consider refining the sampling scheme. Currently, the estimated energetics exhibit a bias when compared with the experimental data. One potential limitation that could mitigate this bias is the treatment of charges, particularly the omission of polarization effects. This might become relevant in our case of study, since a polarizable force field usually are needed[100] when there is a change in the coordination environment, in this case from the ion in solution to the protein cavity. The second possible limitation could be the incorporation of an enhanced sampling technique for the free energy perturbation calculation. As the starting point, the ligand in the bound state; and obtaining the final structure of the unbound state might require some enhanced sampling technique, like Free Energy Perturbation with Replica Exchange Molecular Dynamics (FEP/REMD)[99] to overcome some possible transition barrier. Finally, further studies on features of the ligand structure that define the ligand-ion binding affinity are necessary to refine the choice of ligand employed in the separation processes.

Appendix A: Permissions

Figure A.1: Reproduction permission for Differences in solvation thermodynamics of oxygenates at Pt/Al$_2$O$_3$ perimeter versus Pt(111) terrace sites[25].

Figure A.2: Reproduction permission for Active sites and mechanism of aqueous phase methanol dehydrogenation on Pt/Al$_2$O$_3$ catalysts from multiscale modeling, microkinetic modeling, and operando spectroscopy[37].

Bibliography

[1] Eman A. Alasadi, Wonseok Choi, Xiaobing Chen, Jr Joseph A. Cotruvo, and Carlos R. Baiz. Lanmodulin's ef 2–3 domain: Insights from infrared spectroscopy and simulations. *ACS Chemical Biology*, 4 2024.

[2] M. S. Alias, S. K. Kamarudin, A. M. Zainoodin, and M. S. Masdar. Active direct methanol fuel cell: An overview. *International Journal of Hydrogen Energy*, 45:19620–19641, 7 2020.

[3] Salai Cheettu Ammal and Andreas Heyden. Nature of ptn/tio2(110) interface under water-gas shift reaction conditions: A constrained ab initio thermodynamics study. *Journal of Physical Chemistry C*, 115:19246–19259, 10 2011.

[4] Silvia Angelova, Nikoleta Kircheva, Valya Nikolova, Stefan Dobrev, and Todor Dudev. Electrostatic interactions – key determinants of the metal selectivity in la3+ and ca2+ binding proteins. *Physical Chemistry Chemical Physics*, 25:18149–18157, 7 2023.

[5] Andrew C. Antony, Tao Liang, Sneha A. Akhade, Michael J. Janik, Simon R. Phillpot, and Susan B. Sinnott. Effect of surface chemistry on water interaction with cu(111). *Langmuir*, 32:8061–8070, 8 2016.

[6] Dimitrios Argyris, Tuan Ho, David R. Cole, and Alberto Striolo. Molecular dynamics studies of interfacial water at the alumina surface. *Journal of Physical Chemistry C*, 115:2038–2046, 2 2011.

[7] Burg Ariela, Wolfer Yaniv, Shamir Dror, Kornweitz Haya, Albo Yael, Maimon Eric, and Meyerstein Dan. The role of carbonate in electro-catalytic water oxidation by using ni(1,4,8,11-tetraazacyclotetradecane)2+. *Dalton Transactions*, 46:10774–10779, 8 2017.

[8] Chrystelle N.H. Atinkpahoun, Marie Noëlle Pons, Pauline Louis, Jean Pierre Leclerc, and Henri H. Soclo. Rare earth elements (ree) in the urban wastewater of cotonou (benin, west africa). *Chemosphere*, 251:126398, 7 2020.

[9] V. Balaram. Rare earth elements: A review of applications, occurrence, exploration, analysis, recycling, and environmental impact. *Geoscience Frontiers*, 10:1285–1303, 7 2019.

[10] Roger Barth and Anita Ramachandran. Temperature effects on the infrared spectrum of carbon monoxide adsorbed by supported platinum. *Journal of Catalysis*, 125:467–471, 10 1990.

[11] Arieh Ben-Naim. *Solvation thermodynamics*. Plenum Press, 1987.

[12] Arieh Ben-Naim. Solvation: from small to macro molecules. *Current Opinion in Structural Biology*, 4:264–268, 1 1994.

[13] Arieh Ben-Naim. *Molecular Theory of Water and Aqueous Solutions*. World Scientific Publishing Company, 7 2009. doi:10.1142/7136.

[14] Charles H. Bennett. Efficient estimation of free energy differences from monte carlo data. *Journal of Computational Physics*, 22:245–268, 10 1976.

[15] H. J.C. Berendsen, J. P.M. Postma, W. F. Van Gunsteren, A. Dinola, and J. R. Haak. Molecular dynamics with coupling to an external bath. *The Journal of Chemical Physics*, 81:3684–3690, 10 1984.

[16] Thomas C. Beutler, Alan E. Mark, René C. van Schaik, Paul R. Gerber, and Wilfred F. van Gunsteren. Avoiding singularities and numerical instabilities in free energy calculations based on molecular simulations. *Chemical Physics Letters*, 222:529–539, 6 1994.

[17] Olle Björneholm, Martin H. Hansen, Andrew Hodgson, Li Min Liu, David T. Limmer, Angelos Michaelides, Philipp Pedevilla, Jan Rossmeisl, Huaze Shen, Gabriele Tocci, Eric Tyrode, Marie Madeleine Walz, Josephina Werner, and Hendrik Bluhm. Water at interfaces. *Chemical Reviews*, 116:7698–7726, 7 2016.

[18] Cameron J. Bodenschatz, Tianjun Xie, Xiaohong Zhang, and Rachel B. Getman. Insights into how the aqueous environment influences the kinetics and mechanisms of heterogeneously-catalyzed coh* and ch3oh* dehydrogenation reactions on pt(111). *Physical Chemistry Chemical Physics*, 21:9895–9904, 5 2019.

[19] Cameron J. Bodenschatz, Xiaohong Zhang, Tianjun Xie, Jeremy Arvay, Sapna Sarupria, and Rachel B. Getman. Multiscale sampling of a heterogeneous water/metal catalyst interface using density functional theory and force-field molecular dynamics. *JoVE (Journal of Visualized Experiments)*, 2019:e59284, 4 2019.

[20] Jelle M. Boereboom, Paul Fleurat-Lessard, and Rosa E. Bulo. Explicit solvation matters: Performance of qm/mm solvation models in nucleophilic addition. *Journal of Chemical Theory and Computation*, 14:1841–1852, 4 2018.

[21] Nicéphore Bonnet and Nicola Marzari. Solvation free energies from machine learning molecular dynamics. *Journal of Chemical Theory and Computation*, 5 2024. doi: 10.1021/acs.jctc.4c00116.

[22] Jurriaan Boon, Jasper van Kampen, Roelof Hoogendoorn, Stefania Tanase, Frans P F van Berkel, and Martin van Sint Annaland. Reversible deactivation of γ-alumina by steam in the gas-phase dehydration of methanol to dimethyl ether. *Catalysis Communications*, 119:22–27, 2019.

[23] Oscar Buneman. Computer simulation using particles (r. w. hockney and j. w. eastwood). *SIAM Review*, 25:425–426, 7 1983. doi: 10.1137/1025102.

[24] Charles T. Campbell. The degree of rate control: A powerful tool for catalysis research. *ACS Catalysis*, 7:2770–2779, 4 2017.

[25] Ricardo A Garcia Carcamo, Xiaohong Zhang, Ali Estejab, Jiarun Zhou, Bryan J Hare, Carsten Sievers, Sapna Sarupria, and Rachel B Getman. Differences in solvation thermodynamics of oxygenates at pt/al2o3 perimeter versus pt(111) terrace sites. *iScience*, 26:105980, 7 2023.

[26] David A. Case, Thomas E. Cheatham, Tom Darden, Holger Gohlke, Ray Luo, Kenneth M. Merz, Alexey Onufriev, Carlos Simmerling, Bing Wang, and Robert J. Woods. The amber biomolecular simulation programs. *Journal of Computational Chemistry*, 26:1668–1688, 12 2005.

[27] Yaoyi Chen, Andreas Krämer, Nicholas E. Charron, Brooke E. Husic, Cecilia Clementi, and Frank Noé. Machine learning implicit solvation for molecular dynamics. *Journal of Chemical Physics*, 155:84101, 8 2021.

[28] Clara D. Christ, Alan E. Mark, and Wilfred F. Van Gunsteren. Basic ingredients of free energy calculations: A review. *Journal of Computational Chemistry*, 31:1569–1582, 6 2010.

[29] Aysegul Ciftci, Baoxiang Peng, Andreas Jentys, Johannes A Lercher, and Emiel J M Hensen. Support effects in the aqueous phase reforming of glycerol over supported platinum catalysts. *Applied Catalysis A: General*, 431-432:113–119, 7 2012.

[30] Paul Clabaut, Benjamin Schweitzer, Andreas W. Götz, Carine Michel, and Stephan N. Steinmann. Solvation free energies and adsorption energies at the metal/water interface from hybrid quantum-mechanical/molecular mechanics simulations. *Journal of Chemical Theory and Computation*, 16:6539–6549, 10 2020.

[31] Daniel J. Cole, Julian Tirado-Rives, and William L. Jorgensen. Enhanced monte carlo sampling through replica exchange with solute tempering. *Journal of Chemical Theory and Computation*, 10:565–571, 2 2014.

[32] Erik C. Cook, Emily R. Featherston, Scott A. Showalter, and Joseph A. Cotruvo. Structural basis for rare earth element recognition by methylobacterium extorquens lanmodulin. *Biochemistry*, 58:120–125, 1 2019.

[33] Michael J. Cordon, James W. Harris, Juan Carlos Vega-Vila, Jason S. Bates, Sukhdeep Kaur, Mohit Gupta, Megan E. Witzke, Evan C. Wegener, Jeffrey T. Miller, David W. Flaherty, David D. Hibbitts, and Rajamani Gounder. Dominant role of entropy in stabilizing sugar isomerization transition states within hydrophobic zeolite pores. *Journal of the American Chemical Society*, 140:14244–14266, 10 2018.

[34] I. Coronado, M. Stekrova, M. Reinikainen, P. Simell, L. Lefferts, and J. Lehtonen. A review of catalytic aqueous-phase reforming of oxygenated hydrocarbons derived from biorefinery water fractions. *International Journal of Hydrogen Energy*, 41:11003–11032, 7 2016.

[35] Joseph A. Cotruvo, Emily R. Featherston, Joseph A. Mattocks, Jackson V. Ho, and Tatiana N. Laremore. Lanmodulin: A highly selective lanthanide-binding protein from a lanthanide-utilizing bacterium. *Journal of the American Chemical Society*, 140:15056–15061, 11 2018.

[36] Anastasia Croitoru, Sang Jun Park, Anmol Kumar, Jumin Lee, Wonpil Im, Alexander D. Mackerell, and Alexey Aleksandrov. Additive charmm36 force field for nonstandard amino acids. *Journal of chemical theory and computation*, 17:3554, 6 2021.

[37] Ricardo A. García Cárcamo, Tianjun Xie, Bryan J. Hare, Carsten Sievers, and Rachel B. Getman. Active sites and mechanism of aqueous phase methanol dehydrogenation on pt/al_2o_3 catalysts from multiscale modeling, microkinetic modeling, and operando spectroscopy. *Journal of Catalysis*, 435:115562, 7 2024.

[38] Yihu Dai, Gengnan Li, Daniel E. Resasco, and Yanhui Yang. How do structure and topology of the catalyst affect water promotion or inhibition effects? *Chem Catalysis*, 1:962–965, 10 2021.

[39] Isabella Daidone, Andrea Amadei, and Alfredo Di Nola. Thermodynamic and kinetic characterization of a β-hairpin peptide in solution: An extended phase space sampling by molecular dynamics simulations in explicit water. *Proteins: Structure, Function, and Bioinformatics*, 59:510–518, 5 2005.

[40] Wolfgang Damm, Antonio Frontera, Julian Tirado–Rives, and William L Jorgensen. Opls all-atom force field for carbohydrates. *Journal of Computational Chemistry*, 18:1955–1970, 12 1997.

[41] Tom Darden, Darrin York, and Lee Pedersen. Particle mesh ewald: An n log(n) method for ewald sums in large systems. *The Journal of Chemical Physics*, 98:10089–10092, 6 1993.

[42] Lena J. Daumann. Essential and ubiquitous: The emergence of lanthanide metallobio-chemistry. *Angewandte Chemie International Edition*, 58:12795–12802, 9 2019.

[43] R. R. Davda, J. W. Shabaker, G. W. Huber, R. D. Cortright, and J. A. Dumesic. A review of catalytic issues and process conditions for renewable hydrogen and alkanes by aqueous-phase reforming of oxygenated hydrocarbons over supported metal catalysts. *Applied Catalysis B: Environmental*, 56:171–186, 3 2005.

[44] Gauthier J.P. Deblonde, Joseph A. Mattocks, Dan M. Park, David W. Reed, Joseph A. Cotruvo, and Yongqin Jiao. Selective and efficient biomacromolecular extraction of rare-earth elements using lanmodulin. *Inorganic Chemistry*, 59:11855–11867, 9 2020.

[45] Sanket K Desai, Matthew Neurock, and K Kourtakis. A periodic density functional theory study of the dehydrogenation of methanol over pt(111). *The Journal of Physical Chemistry B*, 106:2559–2568, 7 2002.

[46] Anatoliy I. Dragan, Christopher M. Read, and Colyn Crane-Robinson. Enthalpy–entropy compensation: the role of solvation. *European Biophysics Journal*, 46:301–308, 5 2017.

[47] Magali Duvail, Riccardo Spezia, and Pierre Vitorge. A dynamic model to explain hydration behaviour along the lanthanide series. *ChemPhysChem*, 9:693–696, 4 2008.

[48] Ulrich Essmann, Lalith Perera, Max L. Berkowitz, Tom Darden, Hsing Lee, and Lee G. Pedersen. A smooth particle mesh ewald method. *The Journal of Chemical Physics*, 103:8577–8593, 11 1995.

[49] Ali Estejab, Ricardo A García Cárcamo, and Rachel B Getman. Influence of an electrified interface on the entropy and energy of solvation of methanol oxidation intermediates on platinum(111) under explicit solvation. *Physical Chemistry Chemical Physics*, 24:4251–4261, 7 2022.

[50] Muhammad Faheem and Andreas Heyden. Hybrid quantum mechanics/molecular mechanics solvation scheme for computing free energies of reactions at metal-water interfaces. *Journal of Chemical Theory and Computation*, 10:3354–3368, 8 2014.

[51] Muhammad Faheem, Mohammad Saleheen, Jianmin Lu, and Andreas Heyden. Ethylene glycol reforming on pt(111): first-principles microkinetic modeling in vapor and aqueous phases. *Catalysis Science & Technology*, 6:8242–8256, 11 2016.

[52] Muhammad Faheem, Suwit Suthirakun, and Andreas Heyden. New implicit solvation scheme for solid surfaces. *Journal of Physical Chemistry C*, 116:22458–22462, 10 2012.

[53] I.A.W. Filot. *Introduction to microkinetic modeling.* Technische Universiteit Eindhoven, i edition, 7 2018.

[54] Ivo A W Filot, Robin J P Broos, Jeaphianne P M Van Rijn, Gerardus J H A Van Heugten, Rutger A Van Santen, and Emiel J M Hensen. First-principles-based microkinetics simulations of synthesis gas conversion on a stepped rhodium surface. *ACS Catalysis*, 5:5453–5467, 7 2015.

[55] Ivo A W Filot, Rutger A van Santen, and Emiel J M Hensen. The optimally performing fischer-tropsch catalyst. *Angewandte Chemie International Edition*, 53:12746–12750, 7 2014. https://doi.org/10.1002/anie.201406521.

[56] David W. Flaherty, Wen Yueh Yu, Zachary D. Pozun, Graeme Henkelman, and C. Buddie Mullins. Mechanism for the water–gas shift reaction on monofunctional platinum and cause of catalyst deactivation. *Journal of Catalysis*, 282:278–288, 9 2011.

[57] F. M. Floris and A. Tani. A study of aqueous solutions of lanthanide ions by molecular dynamics simulation with ab initio effective pair potentials. *The Journal of Chemical Physics*, 115:4750–4765, 9 2001.

[58] Emilio Gallicchio and Ronald M. Levy. Agbnp: An analytic implicit solvent model suitable for molecular dynamics simulations and high-resolution modeling. *Journal of Computational Chemistry*, 25:479–499, 3 2004.

[59] Rodrigo García-Muelas, Qiang Li, and Núria López. Density functional theory comparison of methanol decomposition and reverse reactions on metal surfaces. *ACS Catalysis*, 5:1027–1036, 7 2015.

[60] Alejandro J. Garza. Solvation entropy made simple. *Journal of Chemical Theory and Computation*, 15:3204–3214, 5 2019.

[61] Julia Gebhardt, Matthias Kiesel, Sereina Riniker, and Niels Hansen. Combining molecular dynamics and machine learning to predict self-solvation free energies and limiting activity coefficients. *Journal of Chemical Information and Modeling*, 60:5319–5330, 11 2020.

[62] Rahul Godawat, Sumanth N. Jamadagni, and Shekhar Garde. Characterizing hydrophobicity of interfaces by using cavity formation, solute binding, and water correlations. *Proceedings of the National Academy of Sciences of the United States of America*, 106:15119–15124, 9 2009.

[63] Lidia I. Godina, Hans Heeres, Sonia Garcia, Steve Bennett, Stephen Poulston, and Dmitry Yu Murzin. Hydrogen production from sucrose via aqueous-phase reforming. *International Journal of Hydrogen Energy*, 44:14605–14623, 6 2019.

[64] Lidia I Godina, Alexey V Kirilin, Anton V Tokarev, and Dmitry Yu. Murzin. Aqueous phase reforming of industrially relevant sugar alcohols with different chiralities. *ACS Catalysis*, 5:2989–3005, 7 2015.

[65] Lidia I. Godina, Anton V. Tokarev, Irina L. Simakova, Päivi Mäki-Arvela, Ewelina Kortesmäki, Jan Gläsel, Leif Kronberg, Bastian Etzold, and Dmitry Yu Murzin. Aqueous-phase reforming of alcohols with three carbon atoms on carbon-supported pt. *Catalysis Today*, 301:78–89, 3 2018.

[66] N. Goga, A. J. Rzepiela, A. H. De Vries, S. J. Marrink, and H. J.C. Berendsen. Efficient algorithms for langevin and dpd dynamics. *Journal of Chemical Theory and Computation*, 8:3637–3649, 10 2012.

[67] Lars C Grabow, Amit A Gokhale, Steven T Evans, James A Dumesic, and Manos Mavrikakis. Mechanism of the water gas shift reaction on pt: First principles, experiments, and microkinetic modeling. *The Journal of Physical Chemistry C*, 112:4608–4617, 3 2008. doi: 10.1021/jp7099702.

[68] Jeff Greeley and Manos Mavrikakis. Competitive paths for methanol decomposition on pt(111). *Journal of the American Chemical Society*, 126:3910–3919, 3 2004.

[69] Stefan Grimme, Jens Antony, Stephan Ehrlich, and Helge Krieg. A consistent and accurate ab initio parametrization of density functional dispersion correction (dft-d) for the 94 elements h-pu. *The Journal of Chemical Physics*, 132:154104, 7 2010.

[70] Stefan Grimme, Stephan Ehrlich, and Lars Goerigk. Effect of the damping function in dispersion corrected density functional theory. *Journal of Computational Chemistry*, 32:1456–1465, 7 2011.

[71] Axel Groß and Sung Sakong. Ab initio simulations of water/metal interfaces. *Chemical Reviews*, 122:10746–10776, 6 2022.

[72] Geun Ho Gu, Gerhard R. Wittreich, and Dionisios G. Vlachos. Microkinetic modeling of aqueous phase biomass conversion: Application to ethylene glycol reforming. *Chemical Engineering Science*, 197:415–418, 4 2019.

[73] Sophie M. Gutenthaler, Satoru Tsushima, Robin Steudtner, Manuel Gailer, Anja Hoffmann-Röder, Björn Drobot, and Lena J. Daumann. Lanmodulin peptides – unravelling the binding of the ef-hand loop sequences stripped from the structural corset. *Inorganic Chemistry Frontiers*, 9:4009–4021, 8 2022.

[74] Avik Halder, Mai Anh Ha, Huanchen Zhai, Bing Yang, Michael J. Pellin, Sönke Seifert, Anastassia N. Alexandrova, and Stefan Vajda. Oxidative dehydrogenation of cyclohexane by cu vs pd clusters: Selectivity control by specific cluster dynamics. *ChemCatChem*, 12:1307–1315, 3 2020.

[75] Niels Hansen and Wilfred F. Van Gunsteren. Practical aspects of free-energy calculations: A review. *Journal of Chemical Theory and Computation*, 10:2632–2647, 7 2014.

[76] Bryan J. Hare, Ricardo A. Garcia Carcamo, Luke L. Daemen, Yongqiang Cheng, Rachel B. Getman, and Carsten Sievers. Poisoning of pt/γ-al2o3 aqueous phase reforming catalysts by ketone and diketone-derived surface species. *ACS Catalysis*, 14:1480–1493, 1 2024.

[77] Bryan J Hare, Ricardo A Garcia Carcamo, Rachel B Getman, and Carsten Sievers. Surface chemistry of ketones and diketones on lewis acidic $\gamma-al_2o_3$ probed by infrared spectroscopy. *Journal of Physical Chemistry C*, 126:17554–17568, 7 2022.

[78] Bryan J Hare, Ricardo A Garcia Carcamo, Tianjun Xie, Paul J Meza-Morales, Rachel B Getman, and Carsten Sievers. Active sites and effects of co-adsorbed h_2o on isolated methanol dehydrogenation over $pt/\gamma-al_2o_3$. *Journal of Catalysis*, 402:218–228, 7 2021.

[79] Katherine J Harmon, Ying Chen, Eric J Bylaska, Jeffrey G Catalano, Michael J Bedzyk, John H Weare, and Paul Fenter. Insights on the alumina-water interface structure by direct comparison of density functional simulations with x-ray reflectivity. *Journal of Physical Chemistry C*, 122:26934–26944, 7 2018.

[80] Ali A. Hassanali, Jérôme Cuny, Vincenzo Verdolino, and Michele Parrinello. Aqueous solutions: state of the art in ab initio molecular dynamics. *Philosophical Transactions of the Royal Society A: Mathematical, Physical and Engineering Sciences*, 372, 3 2014.

[81] Zhenhong He, Meng Cui, Qingli Qian, Jingjing Zhang, Huizhen Liu, and Buxing Han. Synthesis of liquid fuel via direct hydrogenation of co2. *Proceedings of the National Academy of Sciences*, 116:12654–12659, 7 2019. doi: 10.1073/pnas.1821231116.

[82] Graeme Henkelman and Hannes Jónsson. A dimer method for finding saddle points on high dimensional potential surfaces using only first derivatives. *The Journal of Chemical Physics*, 111:7010, 7 1999.

[83] Graeme Henkelman and Hannes Jónsson. Improved tangent estimate in the nudged elastic band method for finding minimum energy paths and saddle points. *The Journal of Chemical Physics*, 113:9978, 7 2000.

[84] Graeme Henkelman, Blas P Uberuaga, and Hannes Jónsson. A climbing image nudged elastic band method for finding saddle points and minimum energy paths. *The Journal of Chemical Physics*, 113:9901, 7 2000.

[85] Berk Hess and Nico F.A. Van Der Vegt. Hydration thermodynamic properties of amino acid analogues: A systematic comparison of biomolecular force fields and water models. *Journal of Physical Chemistry B*, 110:17616–17626, 9 2006.

[86] Andreas Heyden, Alexis T Bell, and Frerich J Keil. Efficient methods for finding transition states in chemical reactions: Comparison of improved dimer method and partitioned rational function optimization method. *The Journal of Chemical Physics*, 123:224101, 7 2005.

[87] Robert F. Higgins, Kevin P. Ruoff, Amit Kumar, and Eric J. Schelter. Coordination chemistry-driven approaches to rare earth element separations. *Accounts of Chemical Research*, 55:2616–2627, 9 2022.

[88] Tuan Anh Ho, Dimitrios V Papavassiliou, Lloyd L Lee, and Alberto Striolo. Liquid water can slip on a hydrophilic surface. *Proceedings of the National Academy of Sciences*, 108:16170–16175, 7 2011. doi: 10.1073/pnas.1105189108.

[89] William G. Hoover. Canonical dynamics: Equilibrium phase-space distributions. *Physical Review A*, 31:1695, 3 1985.

[90] Yimu Hu, Justyna Florek, Dominic Larivière, Frédéric Georges Fontaine, and Freddy Kleitz. Recent advances in the separation of rare earth elements using mesoporous hybrid materials. *The Chemical Record*, 18:1261–1276, 7 2018.

[91] Jochen S. Hub, Bert L. De Groot, Helmut Grubmüller, and Gerrit Groenhof. Quantifying artifacts in ewald simulations of inhomogeneous systems with a net charge. *Journal of Chemical Theory and Computation*, 10:381–390, 1 2014.

[92] George W. Huber and James A. Dumesic. An overview of aqueous-phase catalytic processes for production of hydrogen and alkanes in a biorefinery. *Catalysis Today*, 111:119–132, 1 2006.

[93] Justin M. Hutchison, Brooke K. Mayer, Marcela Vega, Wambura E. Chacha, and Julie L. Zilles. Making waves: Biocatalysis and biosorption: Opportunities and challenges associated with a new protein-based toolbox for water and wastewater treatment. *Water Research X*, 12:100112, 8 2021.

[94] Jacob N. Israelachvili. *Intermolecular and Surface Forces, Third Edition.* Elsevier, 1 2010.

[95] T. Iwasita. Electrocatalysis of methanol oxidation. *Electrochimica Acta*, 47:3663–3674, 8 2002.

[96] Anubhav Jain, Shyue Ping Ong, Geoffroy Hautier, Wei Chen, William Davidson Richards, Stephen Dacek, Shreyas Cholia, Dan Gunter, David Skinner, Gerbrand Ceder, and Kristin A Persson. Commentary: The materials project: A materials genome approach to accelerating materials innovation. *APL Materials*, 1:11002, 7 2013.

[97] Michael J Janik, Christopher D Taylor, and Matthew Neurock. First-principles analysis of the initial electroreduction steps of oxygen over pt(111). *Journal of The Electrochemical Society*, 156:B126, 7 2009.

[98] Glen R Jenness, Matthew A Christiansen, Stavros Caratzoulas, Dionisios G Vlachos, and Raymond J Gorte. Site-dependent lewis acidity of $\gamma - al_2o_3$ and its impact on ethanol dehydration and etherification. *The Journal of Physical Chemistry C*, 118:12899–12907, 7 2014.

[99] Wei Jiang and Benoît Roux. Free energy perturbation hamiltonian replica-exchange molecular dynamics (fep/h-remd) for absolute ligand binding free energy calculations. *Journal of Chemical Theory and Computation*, 6:2559–2565, 9 2010.

[100] Zhifeng Jing, Chengwen Liu, Sara Y. Cheng, Rui Qi, Brandon D. Walker, Jean Philip Piquemal, and Pengyu Ren. Polarizable force fields for biomolecular simulations: Recent advances and applications. *Annual Review of Biophysics*, 48:371–394, 5 2019.

[101] Shampa Kandoi, Jeff Greeley, Marco A Sanchez-Castillo, Steven T Evans, Amit A Gokhale, James A Dumesic, and Manos Mavrikakis. Prediction of experimental methanol decomposition rates on platinum from first principles. *Topics in Catalysis*, 37:17–27, 7 2006.

[102] M. J. Kappers and J. H. van der Maas. Correlation between co frequency and pt coordination number. a drift study on supported pt catalysts. *Catalysis Letters*, 10:365–373, 9 1991.

[103] Tae Wan Kim, Ho Dong Kim, Kwang Eun Jeong, Ho Jeong Chae, Soon Yong Jeong, Chang Ha Lee, and Chul Ung Kim. Catalytic production of hydrogen through aqueous-phase reforming over platinum/ordered mesoporous carbon catalysts. *Green Chemistry*, 13:1718–1728, 7 2011.

[104] Iskra Z Koleva, Hristiyan A Aleksandrov, and Georgi N Vayssilov. Influence of the adsorption of co on the electronic structure of platinum clusters and nanowires deposited on ceo2(111) and γ-al2o3(001) surfaces. *Catalysis Today*, 357:442–452, 7 2020.

[105] G Kresse and J Furthmüller. Efficiency of ab-initio total energy calculations for metals and semiconductors using a plane-wave basis set. *Computational Materials Science*, 6:15–50, 1996.

[106] G Kresse and J Furthmüller. Efficient iterative schemes for ab initio total-energy calculations using a plane-wave basis set. *Physical Review B*, 54:11169–11186, 7 1996.

[107] G Kresse and J Hafner. Ab initio molecular dynamics for liquid metals. *Physical Review B*, 47:558–561, 7 1993.

[108] G Kresse and D Joubert. From ultrasoft pseudopotentials to the projector augmented-wave method. *Physical Review B*, 59:1758, 7 1999.

[109] K. Y. Kung, P. Chen, F. Wei, Y. R. Shen, and G. A. Somorjai. Sum-frequency generation spectroscopic study of co adsorption and dissociation on pt(111) at high pressure and temperature. *Surface Science*, 463:L627–L633, 9 2000.

[110] Gerhard König, Ye Mei, Frank C. Pickard, Andrew C. Simmonett, Benjamin T. Miller, John M. Herbert, H. Lee Woodcock, Bernard R. Brooks, and Yihan Shao. Computation of hydration free energies using the multiple environment single system quantum mechanical/molecular mechanical method. *Journal of Chemical Theory and Computation*, 12:332–344, 1 2016.

[111] Raudah Lazim, Donghyuk Suh, and Sun Choi. Advances in molecular dynamics simulations and enhanced sampling methods for the study of protein systems. *International Journal of Molecular Sciences 2020, Vol. 21, Page 6339*, 21:6339, 9 2020.

[112] Andrew R Leach. *Molecular modelling: principles and applications.* Prentice Hall, second edition, 2001. ID: 45008511.

[113] W T Lee, F Thomas, and R L Masel. Methanol oxidation on (2×1)pt(110): does the c–o or o–h bond break first? *Surface Science*, 418:479–483, 7 1998.

[114] Dennis H. Leung, Robert G. Bergman, and Kenneth N. Raymond. Enthalpy-entropy compensation reveals solvent reorganization as a driving force for supramolecular encapsulation in water. *Journal of the American Chemical Society*, 130:2798–2805, 3 2008.

[115] Didi Li, Yi Li, Xiaohui Liu, Yong Guo, Chih-Wen Pao, Jeng-Lung Chen, Yongfeng Hu, and Yanqin Wang. Nial2o4 spinel supported pt catalyst: High performance and origin in aqueous-phase reforming of methanol. *ACS Catalysis*, 9:9671–9682, 7 2019. doi: 10.1021/acscatal.9b02243.

[116] Gengnan Li, Mallikharjuna Rao Komarneni, Bin Wang, Nebojsa Marinkovic, and Daniel E Resasco. Cooperative roles of water and metal-support interfaces in the selective hydrogenation of cinnamaldehyde over cobalt boride catalysts. *Cell Reports Physical Science*, 4:101367, 2023.

[117] Gengnan Li, Bin Wang, and Daniel E Resasco. Solvent effects on catalytic reactions and related phenomena at liquid-solid interfaces. *Surface Science Reports*, 76:100541, 2021.

[118] Giovanni Di Liberto and Livia Giordano. Role of solvation model on the stability of oxygenates on pt(111): A comparison between microsolvation, extended bilayer, and extended metal/water interface. *Electrochemical Science Advances*, 4:e2100204, 2 2023.

[119] Steffen Lid, Susan Köppen, and Lucio Colombi Ciacchi. Creation of models and parametrization of a classical force field for amorphous al2o3/water interfaces based on density functional theory. *Computational Materials Science*, 140:307–314, 12 2017.

[120] Nathan M. Lim, Lingle Wang, Robert Abel, and David L. Mobley. Sensitivity in binding free energies due to protein reorganization. *Journal of Chemical Theory and Computation*, 12:4620–4631, 9 2016.

[121] Nidia Gabaldon Limas and Thomas A Manz. Introducing ddec6 atomic population analysis: part 4. efficient parallel computation of net atomic charges, atomic spin moments, bond orders, and more. *RSC Advances*, 8:2678–2707, 7 2018.

[122] David T. Limmer, Adam P. Willard, Paul Madden, and David Chandler. Hydration of metal surfaces can be dynamically heterogeneous and hydrophobic. *Proceedings of the National Academy of Sciences of the United States of America*, 110:4200–4205, 3 2013.

[123] Lili Lin, Yuzhen Ge, Hongbo Zhang, Meng Wang, Dequan Xiao, and Ding Ma. Heterogeneous catalysis in water. *JACS Au*, 1:1834–1848, 11 2021.

[124] Bing Liu, Jian Liu, Teng Li, Zhen Zhao, Xue Qing Gong, Yu Chen, Aijun Duan, Guiyuan Jiang, and Yuechang Wei. Interfacial effects of ceo2-supported pd nanorod in catalytic co oxidation: A theoretical study. *Journal of Physical Chemistry C*, 119:12923–12934, 6 2015.

[125] Maoyuan Liu, Quinn Alexander Besford, Thomas Mulvaney, and Angus Gray-Weale. Order and correlation contributions to the entropy of hydrophobic solvation. *Journal of Chemical Physics*, 142:114117, 3 2015.

[126] Stephanie Liu, Emily R. Featherston, Joseph A. Cotruvo, and Carlos R. Baiz. Lanthanide-dependent coordination interactions in lanmodulin: a 2d ir and molecular dynamics simulations study. *Physical Chemistry Chemical Physics*, 23:21690–21700, 10 2021.

[127] Hao Lu, Yuan Zhong, Yao Jie, Pan Yin, Xiao Jie Zhao, Yu Liang Feng, Tian Yao Shen, Jing Yi Guo, Wei Zhang, Min Pu, and Hong Yan. A dft study on methanol decomposition over single atom pt/ceo2 catalysts: the effect of the position of pt. *Physical Chemistry Chemical Physics*, 25:14232–14244, 7 2023.

[128] Xiya Lu, Dong Fang, Shingo Ito, Yuko Okamoto, Victor Ovchinnikov, and Qiang Cui. Qm/mm free energy simulations: recent progress and challenges. *Molecular Simulation*, 42:1056–1078, 9 2016.

[129] Nianjun Luo, Xianwen Fu, Fahai Cao, Tiancun Xiao, and Peter P Edwards. Glycerol aqueous phase reforming for hydrogen generation over pt catalyst – effect of catalyst composition and reaction conditions. *Fuel*, 87:3483–3489, 7 2008.

[130] Pablo G. Lustemberg, Robert M. Palomino, Ramón A. Gutiérrez, David C. Grinter, Mykhailo Vorokhta, Zongyuan Liu, Pedro J. Ramírez, Vladimír Matolín, M. Verónica Ganduglia-Pirovano, Sanjaya D. Senanayake, and José A. Rodriguez. Direct conversion of methane to methanol on ni-ceria surfaces: Metal-support interactions and water-enabled catalytic conversion by site blocking. *Journal of the American Chemical Society*, 140:7681–7687, 6 2018.

[131] Alenka Luzar and David Chandler. Hydrogen-bond kinetics in liquid water. *Nature 1996 379:6560*, 379:55–57, 1 1996.

[132] A. D. MacKerell, D. Bashford, M. Bellott, R. L. Dunbrack, J. D. Evanseck, M. J. Field, S. Fischer, J. Gao, H. Guo, S. Ha, D. Joseph-McCarthy, L. Kuchnir, K. Kuczera, F. T.K. Lau, C. Mattos, S. Michnick, T. Ngo, D. T. Nguyen, B. Prodhom, W. E. Reiher, B. Roux, M. Schlenkrich, J. C. Smith, R. Stote, J. Straub, M. Watanabe, J. Wiórkiewicz-Kuczera, D. Yin, and M. Karplus. All-atom empirical potential for molecular modeling and dynamics studies of proteins. *Journal of Physical Chemistry B*, 102:3586–3616, 4 1998.

[133] Alex M. Maldonado, Satoshi Hagiwara, Tae Hoon Choi, Frank Eckert, Kathleen Schwarz, Ravishankar Sundararaman, Minoru Otani, and John A. Keith. Quantifying uncertainties in solvation procedures for modeling aqueous phase reaction mechanisms. *Journal of Physical Chemistry A*, 125:154–164, 1 2021.

[134] Fausto Martelli, Sacha Abadie, Jean Pierre Simonin, Rodolphe Vuilleumier, and Riccardo Spezia. Lanthanoids(iii) and actinoids(iii) in water: Diffusion coefficients and hydration enthalpies from polarizable molecular dynamics simulations. *Pure and Applied Chemistry*, 85:237–246, 7 2013.

[135] Sergey B. Martynov, Richard T.J. Porter, and Haroun Mahgerefteh. Henry's law constants and vapor-liquid distribution coefficients of noncondensable gases dissolved in carbon dioxide. *ACS Omega*, 7:8777–8788, 3 2022.

[136] Kiran Mathew, Ravishankar Sundararaman, Kendra Letchworth-Weaver, T. A. Arias, and Richard G. Hennig. Implicit solvation model for density-functional study of nanocrystal surfaces and reaction pathways. *Journal of Chemical Physics*, 140, 2 2014.

[137] Guilherme Duarte Ramos Matos, Daisy Y. Kyu, Hannes H. Loeffler, John D. Chodera, Michael R. Shirts, and David L. Mobley. Approaches for calculating solvation free

energies and enthalpies demonstrated with an update of the freesolv database. *Journal of Chemical and Engineering Data*, 62:1559–1569, 5 2017.

[138] Andraž Mavrič, Matjaz Valant, Chunhua Cui, and Zhiming M. Wang. Advanced applications of amorphous alumina: From nano to bulk. *Journal of Non-Crystalline Solids*, 521:119493, 10 2019.

[139] Yuhan Mei and N. Aaron Deskins. An evaluation of solvent effects and ethanol oxidation. *Physical Chemistry Chemical Physics*, 23:16180–16192, 8 2021.

[140] Lindsay R. Merte, Guowen Peng, Ralf Bechstein, Felix Rieboldt, Carrie A. Farberow, Lars C. Grabow, Wilhelmine Kudernatsch, Stefan Wendt, Erik Lægsgaard, Manos Mavrikakis, and Flemming Besenbacher. Water-mediated proton hopping on an iron oxide surface. *Science*, 336:889–893, 5 2012.

[141] Hendrik J Monkhorst and James D Pack. Special points for brillouin-zone integrations. *Physical Review B*, 13:5188–5192, 7 1976.

[142] Matthew M. Montemore, Oliviero Andreussi, and J. Will Medlin. Hydrocarbon adsorption in an aqueous environment: A computational study of alkyls on cu(111). *Journal of Chemical Physics*, 145:74702, 8 2016.

[143] J J Mortensen, L B Hansen, and K W Jacobsen. Real-space grid implementation of the projector augmented wave method. *Physical Review B - Condensed Matter and Materials Physics*, 71:35109, 7 2005.

[144] B F Ngouana-Wakou, P Cornette, M Corral Valero, D Costa, and P Raybaud. An atomistic description of the γ-alumina/water interface revealed by ab initio molecular dynamics. *Journal of Physical Chemistry C*, 121:10351–10363, 7 2017.

[145] Xiaowa Nie, Wenjia Luo, Michael J Janik, and Aravind Asthagiri. Reaction mechanisms of co2 electrochemical reduction on cu(1 1 1) determined with density functional theory. *Journal of Catalysis*, 312:108–122, 7 2014.

[146] Sandeep Nigam and Chiranjib Majumder. Orr viability of alumina-supported platinum nanocluster: exploring oxidation behaviour by dft. *Physical Chemistry Chemical Physics*, 19:19308–19315, 7 2017.

[147] Shüichi Nosé. A molecular dynamics method for simulations in the canonical ensemble. *Molecular Physics*, 52:255–268, 1984.

[148] Jude A Okolie, Biswa R Patra, Alivia Mukherjee, Sonil Nanda, Ajay K Dalai, and Janusz A Kozinski. Futuristic applications of hydrogen in energy, biorefining, aerospace, pharmaceuticals and metallurgy. *International Journal of Hydrogen Energy*, 46:8885–8905, 7 2021.

[149] M. Parrinello and A. Rahman. Polymorphic transitions in single crystals: A new molecular dynamics method. *Journal of Applied Physics*, 52:7182–7190, 12 1981.

[150] John P Perdew, Kieron Burke, and Matthias Ernzerhof. Generalized gradient approximation made simple. *Physical Review Letters*, 77:3865–3868, 7 1996.

[151] John P Perdew, Kieron Burke, and Matthias Ernzerhof. Generalized gradient approximation made simple [phys. rev. lett. 77, 3865 (1996)]. *Physical Review Letters*, 78:1396, 7 1997.

[152] Remo Perozzo, Gerd Folkers, and Leonardo Scapozza. Thermodynamics of protein-ligand interactions: history, presence, and future aspects. *Journal of receptor and signal transduction research*, 24:1–52, 2004.

[153] Ingmar Persson. Hydrated metal ions in aqueous solution: How regular are their structures? *Pure and Applied Chemistry*, 82:1901–1917, 8 2010.

[154] Nikolay G. Petrik, Patricia L Huestis, Jay A LaVerne, Alexandr B Aleksandrov, Thomas M Orlando, and Greg A Kimmel. Molecular water adsorption and reactions on $\alpha - al_2o_3(0001)$ and α-alumina particles. *The Journal of Physical Chemistry C*, 122:9540–9551, 7 2018.

[155] A A Phatak, N Koryabkina, S Rai, J L Ratts, W Ruettinger, R J Farrauto, G E Blau, W N Delgass, and F H Ribeiro. Kinetics of the water–gas shift reaction on pt catalysts supported on alumina and ceria. *Catalysis Today*, 123:224–234, 2007.

[156] Abhijit A. Phatak, W. Nicholas Delgass, Fabio H. Ribeiro, and William F. Schneider. Density functional theory comparison of water dissociation steps on cu, au, ni, pd, and pt. *Journal of Physical Chemistry C*, 113:7269–7276, 4 2009.

[157] Giuseppe Pipitone, Giulia Zoppi, Alessandra Frattini, Sergio Bocchini, Raffaele Pirone, and Samir Bensaid. Aqueous phase reforming of sugar-based biorefinery streams: from the simplicity of model compounds to the complexity of real feeds. *Catalysis Today*, 345:267–279, 7 2020.

[158] Giuseppe Pipitone, Giulia Zoppi, Raffaele Pirone, and Samir Bensaid. A critical review on catalyst design for aqueous phase reforming. *International Journal of Hydrogen Energy*, 47:151–180, 7 2022.

[159] Steve Plimpton. Fast parallel algorithms for short-range molecular dynamics. *Journal of Computational Physics*, 117:1–19, 3 1995.

[160] Alberto Podjarny, Annick P Dejaegere, and Bruno Kieffer. Biophysical approaches determining ligand binding to biomolecular targets: Detection, measurement and modelling. *RSC Biomolecular sciences*, 2011.

[161] A (Andrew) Pohorille and Ch. (Christophe) Chipot. Free energy calculations: theory and applications in chemistry and biology. *Springer*, page 517, 2007.

[162] Andrew Pohorille, Christopher Jarzynski, and Christophe Chipot. Good practices in free-energy calculations. *Journal of Physical Chemistry B*, 114:10235–10253, 8 2010.

[163] David S. Potts, Vijaya Sundar Jeyaraj, Ohsung Kwon, Richa Ghosh, Alexander V. Mironenko, and David W. Flaherty. Effect of interactions between alkyl chains and solvent structures on lewis acid catalyzed epoxidations. *ACS Catalysis*, 12:13372–13393, 11 2022.

[164] Rodolfo Salazar Pérez, Mariana M V M Souza, Neyda C Om Tapanes, Gisel Chenard Diaz, and Donato A G Aranda. Production of hydrogen from aqueous phase reforming of glycerol: Economic evaluation. *Engineering*, 6:12–18, 7 2014.

[165] Ali Mehdizadeh Rahimi, Safa Jamali, Jaydeep P. Bardhan, and Steven R. Lustig. Solvation thermodynamics of solutes in water and ionic liquids using the multiscale solvation-layer interface condition continuum model. *Journal of Chemical Theory and Computation*, 2022.

[166] M. M. Rahman. Aqueous-phase reforming of glycerol over carbon-nanotube-supported catalysts. *Catalysis Letters*, 150:2674–2687, 9 2020.

[167] Víctor A Ranea, William F Schneider, and Ian Carmichael. Dft characterization of coverage dependent molecular water adsorption modes on α -al_2o_3 (0001). *Surface Science*, 602:268–275, 2008.

[168] A. K. Rappé, C. J. Casewit, K. S. Colwell, W. A. Goddard, and W. M. Skiff. Uff, a full periodic table force field for molecular mechanics and molecular dynamics simulations. *Journal of the American Chemical Society*, 114:10024–10035, 12 1992.

[169] Ekaterina L. Ratkova, David S. Palmer, and Maxim V. Fedorov. Solvation thermodynamics of organic molecules by the molecular integral equation theory: Approaching chemical accuracy. *Chemical Reviews*, 115:6312–6356, 7 2015.

[170] Richard C. Remsing, Shule Liu, and John D. Weeks. Long-ranged contributions to solvation free energies from theory and short-ranged models. *Proceedings of the National Academy of Sciences of the United States of America*, 113:2819–2826, 3 2016.

[171] Jérôme Rey, Paul Clabaut, Romain Réocreux, Stephan N Steinmann, and Carine Michel. Mechanistic investigation and free energies of the reactive adsorption of ethanol at the alumina/water interface. *The Journal of Physical Chemistry C*, 126:7446–7455, 7 2022.

[172] Peter S Rice, Yu Mao, Chenxi Guo, and P Hu. Interconversion of hydrated protons at the interface between liquid water and platinum. *Physical Chemistry Chemical Physics*, 21:5932–5940, 7 2019.

[173] Stefan Ringe, Nicolas G. Hörmann, Harald Oberhofer, and Karsten Reuter. Implicit solvation methods for catalysis at electrified interfaces. *Chemical Reviews*, 122:10777–10820, 6 2022.

[174] Renée M. Ripken, Jan Meuldijk, Johannes G.E. Gardeniers, and Séverine Le Gac. Influence of the water phase state on the thermodynamics of aqueous-phase reforming for hydrogen production. *ChemSusChem*, 10:4909–4913, 12 2017.

[175] S. Rudtsch. Uncertainty of heat capacity measurements with differential scanning calorimeters. *Thermochimica Acta*, 382:17–25, 1 2002.

[176] Manuel F Ruiz-Lopez, Joseph S Francisco, Marilia T C Martins-Costa, and Josep M Anglada. Molecular reactions at aqueous interfaces. *Nature Reviews Chemistry*, 4:459–475, 2020.

[177] Daniel Sadowsky and J. Samuel Arey. Prediction of aqueous free energies of solvation using coupled qm and mm explicit solvent simulations. *Physical Chemistry Chemical Physics*, 22:8021–8034, 4 2020.

[178] Javad Saien, Farzaneh Moghaddamnia, and Hamid Bamdadi. Interfacial tension of methylbenzene-water in the presence of hydrophilic and hydrophobic alumina nanoparticles at different temperatures. *Journal of Chemical and Engineering Data*, 58:436–440, 2 2013.

[179] Mohammad Saleheen, Mehdi Zare, Muhammad Faheem, and Andreas Heyden. Computational investigation of aqueous phase effects on the dehydrogenation and dehydroxylation of polyols over pt(111). *Journal of Physical Chemistry C*, 123:19052–19065, 8 2019.

[180] Kryslaine M.A. Santos, Elise M. Albuquerque, Giada Innocenti, Luiz E.P. Borges, Carsten Sievers, and Marco A. Fraga. The role of brønsted and water-tolerant lewis acid sites in the cascade aqueous-phase reaction of triose to lactic acid. *ChemCatChem*, 11:3054–3063, 7 2019.

[181] Saurabh Jyoti Sarma, Vinayak Pachapur, Satinder Kaur Brar, Yann Le Bihan, and Gerardo Buelna. Hydrogen biorefinery: Potential utilization of the liquid waste

from fermentative hydrogen production. *Renewable and Sustainable Energy Reviews*, 50:942–951, 10 2015.

[182] Felix Sedlmeier, Dominik Horinek, and Roland R. Netz. Entropy and enthalpy convergence of hydrophobic solvation beyond the hard-sphere limit. *Journal of Chemical Physics*, 134, 2 2011.

[183] Asma Sellami, Manon Réau, Florent Langenfeld, Nathalie Lagarde, and Matthieu Montes. *Molecular Docking for Computer-Aided Drug Design*. Elsevier, 1 2021.

[184] A. Seretis and P. Tsiakaras. A thermodynamic analysis of hydrogen production via aqueous phase reforming of glycerol. *Fuel Processing Technology*, 134:107–115, 6 2015.

[185] R D Shannon. Revised effective ionic radii and systematic studies of interatomic distances in halides and chalcogenides. *Acta Crystallographica Section A*, 32:751–767, 9 1976.

[186] Devleena Shivakumar, Joshua Williams, Yujie Wu, Wolfgang Damm, John Shelley, and Woody Sherman. Prediction of absolute solvation free energies using molecular dynamics free energy perturbation and the opls force field. *Journal of Chemical Theory and Computation*, 6:1509–1519, 5 2010.

[187] David S Sholl and Janice A Steckel. *Density functional theory a practical introduction*. John Wiley & Sons, 2009.

[188] Paul E. Smith and Wilfred F. van Gunsteren. The viscosity of spc and spc/e water at 277 and 300 k. *Chemical Physics Letters*, 215:315–318, 12 1993.

[189] David Van Der Spoel, Erik Lindahl, Berk Hess, Gerrit Groenhof, Alan E. Mark, and Herman J.C. Berendsen. Gromacs: Fast, flexible, and free. *Journal of Computational Chemistry*, 26:1701–1718, 12 2005.

[190] K. Stanciakova and B. M. Weckhuysen. Water–active site interactions in zeolites and their relevance in catalysis. *Trends in Chemistry*, 3:456–468, 6 2021.

[191] Miguel Steiner, Tanja Holzknecht, Michael Schauperl, and Maren Podewitz. Quantum chemical microsolvation by automated water placement. *Molecules*, 26, 3 2021.

[192] Stephan N. Steinmann and Carine Michel. How to gain atomistic insights on reactions at the water/solid interface? *ACS Catalysis*, 12:6294–6301, 6 2022.

[193] Stephan N. Steinmann, Philippe Sautet, and Carine Michel. Solvation free energies for periodic surfaces: comparison of implicit and explicit solvation models. *Physical Chemistry Chemical Physics*, 18:31850–31861, 11 2016.

[194] Andrew D. Sutton, Fraser D. Waldie, Ruilian Wu, Marcel Schlaf, Louis A. 'Pete'Silks, and John C. Gordon. The hydrodeoxygenation of bioderived furans into alkanes. *Nature Chemistry 2013 5:5*, 5:428–432, 4 2013.

[195] Junyu Tao, Lian Hou, Beibei Yan, Guanyi Chen, Wanqing Li, Hong Chen, Zhanjun Cheng, and Fawei Lin. Hydrogen production via aqueous-phase reforming of ethylene glycol over a nickel–iron alloy catalyst: Effect of cobalt addition. *Energy & Fuels*, 34:1153–1161, 7 2020. doi: 10.1021/acs.energyfuels.9b02149.

[196] John Tatini Titantah and Mikko Karttunen. Long-time correlations and hydrophobe-modified hydrogen-bonding dynamics in hydrophobic hydration. *Journal of the American Chemical Society*, 134:9362–9368, 6 2012.

[197] A. V. Tokarev, A. V. Kirilin, E. V. Murzina, K. Eränen, L. M. Kustov, D. Yu Murzin, and J. P. Mikkola. The role of bio-ethanol in aqueous phase reforming to sustainable hydrogen. *International Journal of Hydrogen Energy*, 35:12642–12649, 11 2010.

[198] Mark E Tuckerman. Free energy calculations: Theory and applications. *Journal of the American Chemical Society*, 129:10963–10964, 9 2007. doi: 10.1021/ja076952n.

[199] Christina Eleftheria Tzeliou, Markella Aliki Mermigki, and Demeter Tzeli. Review on the qm/mm methodologies and their application to metalloproteins. *Molecules*, 27, 5 2022.

[200] Ryo Urano, Wataru Shinoda, Noriyuki Yoshii, and Susumu Okazaki. Exact long-range coulombic energy calculation for net charged systems neutralized by uniformly distributed background charge using fast multipole method and its application to efficient free energy calculation. *Journal of Chemical Physics*, 152:244115, 6 2020.

[201] Tamás Vajda and András Perczel. Role of water in protein folding, oligomerization, amyloidosis and miniprotein. *Journal of Peptide Science*, 20:747–759, 10 2014.

[202] Geeta Verma, Jacob Hostert, Alex A Summerville, Alicia S Robang, Ricardo Garcia Carcamo, Anant K Paravastu, Rachel B Getman, Christine E Duval, and Julie Renner. Investigation of rare earth element binding to a surface-bound affinity peptide derived from ef-hand loop i of lanmodulin. *ACS Applied Materials & Interfaces*, 16:16912–16926, 4 2024. doi: 10.1021/acsami.3c17565.

[203] Alessandra Villa and Alan E. Mark. Calculation of the free energy of solvation for neutral analogs of amino acid side chains. *Journal of Computational Chemistry*, 23:548–553, 4 2002.

[204] Alexander D. Wade, Agastya P. Bhati, Shunzhou Wan, and Peter V. Coveney. Alchemical free energy estimators and molecular dynamics engines: Accuracy, precision, and reproducibility. *Journal of Chemical Theory and Computation*, 18:3972–3987, 6 2022.

[205] Eric A Walker, Donald Mitchell, Gabriel A Terejanu, and Andreas Heyden. Identifying active sites of the water–gas shift reaction over titania supported platinum catalysts under uncertainty. *ACS Catalysis*, 8:3990–3998, 7 2018.

[206] Lingle Wang, Richard A. Friesner, and B. J. Berne. Replica exchange with solute scaling: A more efficient version of replica exchange with solute tempering (rest2). *Journal of Physical Chemistry B*, 115:9431–9438, 8 2011.

[207] Rui Wang, Zhenchao Zhao, Pan Gao, Kuizhi Chen, Zhehong Gan, Qiang Fu, and Guangjin Hou. Impact of adsorption configurations on alcohol dehydration over alumina catalysts. *The Journal of Physical Chemistry C*, 126:10073–10080, 7 2022.

[208] Jonas Wirth and Peter Saalfrank. The chemistry of water on α-alumina: Kinetics and nuclear quantum effects from first principles. *The Journal of Physical Chemistry C*, 116:26829–26840, 7 2012.

[209] Jinghua Wu, Yang Huang, Wen Ye, Yanguang Li, J Wu, Y Huang, W Ye, and Y Li. Co2 reduction: From the electrochemical to photochemical approach. *Advanced Science*, 4:1700194, 11 2017.

[210] Ruitao Wu and Lichang Wang. Insight into the solvent effects on ethanol oxidation on ir(100). *Physical Chemistry Chemical Physics*, 25:2190–2202, 1 2023.

[211] Tianjun Xie, Bryan J Hare, Paul J Meza-Morales, Carsten Sievers, and Rachel B Getman. Identification of the active sites in the dehydrogenation of methanol on *pt/al2o3* catalysts. *The Journal of Physical Chemistry C*, 124:19015–19023, 7 2020.

[212] Ming Yuan Xu, Zihang Su, and Julie N. Renner. Characterization of cerium (iii) ion binding to surface-immobilized ef-hand loop i of calmodulin. *Peptide Science*, 111:e24133, 11 2019.

123

[213] Quanhui Ye, Xiuyu Jin, Baotong Zhu, Haifeng Gao, and Na Wei. Lanmodulin-functionalized magnetic nanoparticles as a highly selective biosorbent for recovery of rare earth elements. *Environmental Science and Technology*, 57:4276–4285, 3 2023.

[214] Yiming Ye, Hsiau Wei Lee, Wei Yang, Sarah Shealy, and Jenny J. Yang. Probing site-specific calmodulin calcium and lanthanide affinity by grafting. *Journal of the American Chemical Society*, 127:3743–3750, 3 2005.

[215] David C. Young. *Computational Chemistry*. Wiley, 2 2001.

[216] Borna Zandkarimi and Anastassia N. Alexandrova. Dynamics of subnanometer pt clusters can break the scaling relationships in catalysis. *Journal of Physical Chemistry Letters*, 10:460–467, 2 2019.

[217] Mehdi Zare, Mohammad S. Saleheen, Nirala Singh, Mark J. Uline, Muhammad Faheem, and Andreas Heyden. Liquid-phase effects on adsorption processes in heterogeneous catalysis. *JACS Au*, 2:2119–2134, 9 2022.

[218] Jin Zhang, Haiyang Zhang, Tao Wu, Qi Wang, and David Van Der Spoel. Comparison of implicit and explicit solvent models for the calculation of solvation free energy in organic solvents. *Journal of Chemical Theory and Computation*, 13:1034–1043, 3 2017.

[219] Jun Zhang, Norah Heinz, and Michael Dolg. Understanding lanthanoid(iii) hydration structure and kinetics by insights from energies and wave functions. *Inorganic Chemistry*, 53:7700–7708, 7 2014.

[220] Xiaohong Zhang, Ryan S Defever, Sapna Sarupria, and Rachel B Getman. Free energies of catalytic species adsorbed to pt(111) surfaces under liquid solvent calculated using classical and quantum approaches. *Journal of Chemical Information and Modeling*, 59:2190–2198, 7 2019.

[221] Xiaohong Zhang and Rachel Getman. Development of improved models for simulating adsorption kinetics and solvation free energies of catalytic species at pt(111)/liquid water interfaces. *ProQuest Dissertations and Theses*, page 102, 2021. Copyright - Database copyright ProQuest LLC; ProQuest does not claim copyright in the individual underlying works. Last updated - 2023-03-08.

[222] Xiaohong Zhang, Aditya Savara, and Rachel B Getman. A method for obtaining liquid-solid adsorption rates from molecular dynamics simulations: Applied to methanol on pt(111) in h2o. *Journal of Chemical Theory and Computation*, 16:2680–2691, 7 2020.

[223] Shu Zhao, Fang Chen, Sibin Duan, Bin Shao, Tianbo Li, Hailian Tang, Qingquan Lin, Junying Zhang, Lin Li, Jiahui Huang, Nicolas Bion, Wei Liu, Hui Sun, Ai Qin Wang, Masatake Haruta, Botao Qiao, Jun Li, Jingyue Liu, and Tao Zhang. Remarkable active-site dependent h2o promoting effect in co oxidation. *Nature Communications 2019 10:1*, 10:1–9, 8 2019.

[224] Zhi Jian Zhao, Zhenglong Li, Yanran Cui, Houyu Zhu, William F. Schneider, W. Nicholas Delgass, Fabio Ribeiro, and Jeffrey Greeley. Importance of metal-oxide interfaces in heterogeneous catalysis: A combined dft, microkinetic, and experimental study of water-gas shift on au/mgo. *Journal of Catalysis*, 345:157–169, 1 2017.

[225] Ming Zheng, Xin Zhou, Yu Zhou, and Mingxia Li. Theoretical insights into mechanisms of electrochemical reduction of co2 to ethylene catalyzed by pd3au. *Applied Surface Science*, 572:151474, 7 2022.

[226] Álvaro Pérez-Barcia, Gustavo Cárdenas, Juan J. Nogueira, and Marcos Mandado. Effect of the qm size, basis set, and polarization on qm/mm interaction energy decomposition analysis. *Journal of Chemical Information and Modeling*, 63:882–897, 2 2023.

[227] Líney Árnadóttir, Eric M. Stuve, and Hannes Jónsson. The effect of coadsorbed water on the stability, configuration and interconversion of formyl (hco) and hydroxymethylidyne (coh) on platinum (1 1 1). *Chemical Physics Letters*, 541:32–38, 7 2012.